

AD-A267 764



UNIVERSITY OF CALIFORNIA, BERKELEY

Department of Materials Science and Mineral Engineering

OTIC

LECTE

AUG 6 1993

C

D

Final Report

to

AFOSR-TR-90-0167

U.S. Air Force Office of Scientific Research
on

**MICROMECHANISMS OF MONOTONIC AND CYCLIC
SUBCRITICAL CRACK GROWTH IN ADVANCED HIGH
MELTING POINT LOW-DUCTILITY INTERMETALLICS**

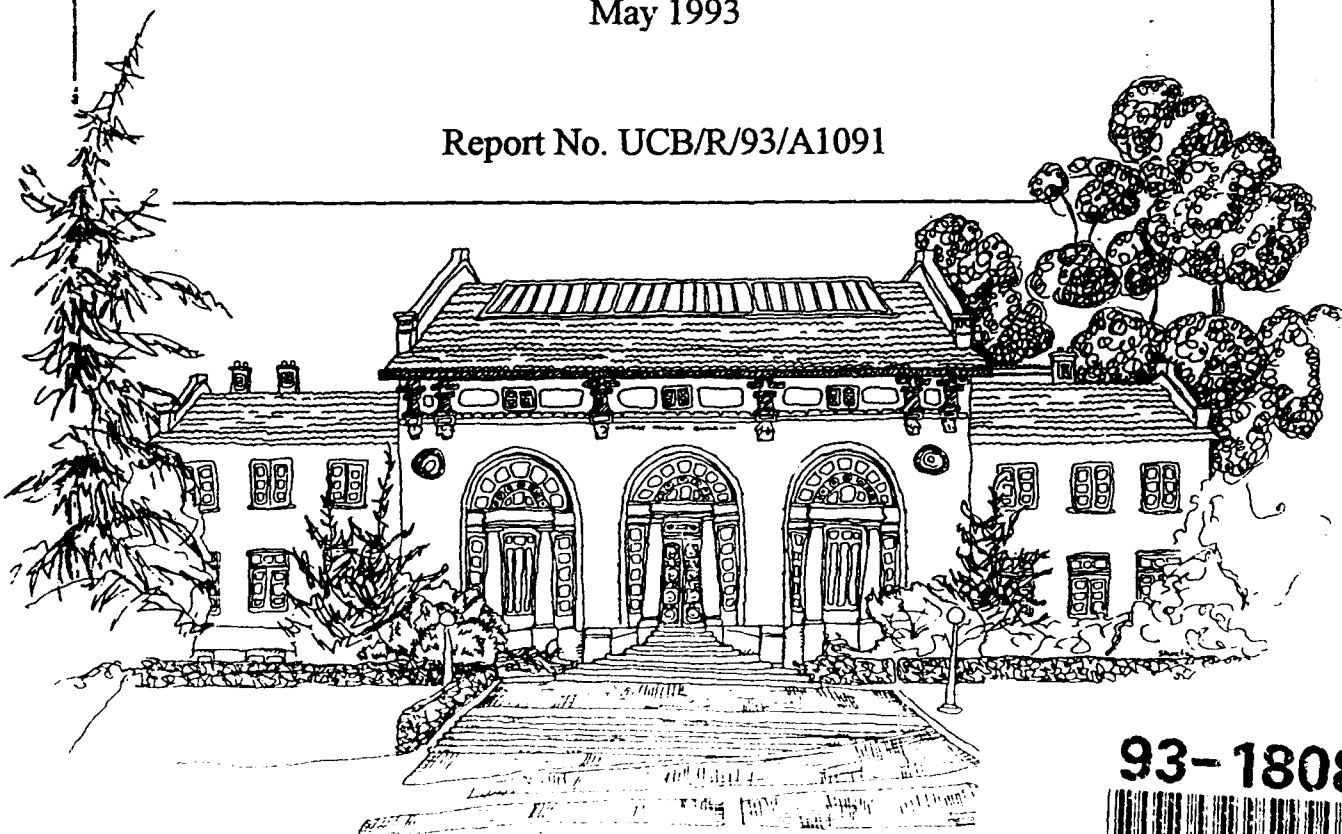
Grant No. AFOSR-90-0167
for period 1 April 1990 to 31 March 1993

by

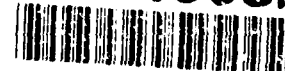
K. T. Venkateswara Rao, L. Muruges and R. O. Ritchie

May 1993

Report No. UCB/R/93/A1091



93-18082



93

8

03

135

Hearst Mining Building, Berkeley, CA 94720

Approved for public release;
distribution unlimited.

UNCLASSIFIED

SECURITY CLASSIFICATION OF THIS PAGE

REPORT DOCUMENTATION PAGE

1a. REPORT SECURITY CLASSIFICATION Unclassified			1b. RESTRICTIVE MARKINGS None		
2a. SECURITY CLASSIFICATION AUTHORITY Not Applicable			3. DISTRIBUTION / AVAILABILITY OF REPORT Approved for public release; Not Applicable distribution unlimited.		
2b. DECLASSIFICATION / DOWNGRADING SCHEDULE Not Applicable			5. MONITORING ORGANIZATION REPORT NUMBER(S)		
4. PERFORMING ORGANIZATION REPORT NUMBER(S) UCB/R/93/A1091			7a. NAME OF MONITORING ORGANIZATION Air Force Office of Scientific Research AFOSR/NC		
6a. NAME OF PERFORMING ORGANIZATION Robert O. Ritchie, Dept. of Mat. Sci. & Minl. Eng.		6b. OFFICE SYMBOL (if applicable) N/C	7b. ADDRESS (City, State, and ZIP Code) Bldg. 410, Bolling Air Force Base Washington, D.C. 20322 ATTN: Dr. A. H. Rosenstein		
8a. NAME OF FUNDING / SPONSORING ORGANIZATION AFOSR		8b. OFFICE SYMBOL (if applicable) N/C	9. PROCUREMENT INSTRUMENT IDENTIFICATION NUMBER AFOSR-90-0167		
8c. ADDRESS (City, State, and ZIP Code) 110 Duane Ave Bolling AFB, DC 20332			10. SOURCE OF FUNDING NUMBERS		
			PROGRAM ELEMENT NO. 101102F	PROJECT NO. 2306	TASK NO. A1
			WORK UNIT ACCESSION NO.		
11. TITLE (Include Security Classification) MICROMECHANISMS OF MONOTONIC AND CYCLIC SUBCRITICAL CRACK GROWTH IN ADVANCED HIGH MELTING POINT LOW-DUCTILITY INTERMETALLICS (Unclassified)					
12. PERSONAL AUTHOR(S) VENKATESWARA RAO, K.T., MURUGESH, L. and RITCHIE, R.O.					
13a. TYPE OF REPORT Final		13b. TIME COVERED FROM 90/4/1 TO 93/3/31		14. DATE OF REPORT (Year, Month, Day) 1993 May 1	
15. PAGE COUNT 115					
16. SUPPLEMENTARY NOTATION					
17. COSATI CODES			18. SUBJECT TERMS (Continue on reverse if necessary and identify by block number)		
FIELD	GROUP	SUB-GROUP	Intermetallic Composites; Fatigue Crack Propagation; Fracture Toughness		
19. ABSTRACT (Continue on reverse if necessary and identify by block number)					
<p>The next generation of high-performance engines will require stiffer materials, operating at higher stress levels and capable of withstanding significantly higher temperatures up to 1650°C and above. Prime candidates for such applications include ordered intermetallics, ceramics, and composites based on metal, intermetallic and ceramic or carbon matrices. However, these materials are currently of limited use due to their low ductility and toughness properties; moreover, an understanding of their fatigue resistance is still essentially lacking. Accordingly, the present research was aimed at examining one class of these materials, namely ductile-phase toughened intermetallic alloys, with respect to the critical factors influencing crack-propagation resistance under monotonic and cyclic loading. The model systems studied included TiNb- and Nb-reinforced γ-TiAl, Nb-reinforced Nb₃Al, and Nb-reinforced MoSi₂.</p>					
20. DISTRIBUTION / AVAILABILITY OF ABSTRACT <input checked="" type="checkbox"/> UNCLASSIFIED/UNLIMITED <input type="checkbox"/> SAME AS RPT. <input type="checkbox"/> DTIC USERS			21. ABSTRACT SECURITY CLASSIFICATION Unclassified		
22a. NAME OF RESPONSIBLE INDIVIDUAL Dr. Rosenstein			22b. TELEPHONE (Include Area Code) 202-747-4960		22c. OFFICE SYMBOL AFOSR/NC

Specifically, the influence of type, volume fraction, thickness and orientation of TiNb and Nb reinforcements on the room temperature fatigue and fracture resistance of γ -TiAl intermetallic alloys was investigated. Large improvements in toughness compared to monolithic γ -TiAl were observed for composites reinforced with elongated β -TiNb and Nb particles under monotonic loading; the toughness increased with increasing ductile phase content, reinforcement thickness and strength, although orientation effects were minimal. Crack-growth behavior was characterized by steep resistance curves, primarily due to crack trapping/renucleation and extensive crack bridging by ductile-phase particles in the crack wake. In contrast, under cyclic loading the influence of ductile phases on fatigue resistance was seen to be strongly dependent upon reinforcement orientation. Compared to monolithic γ -TiAl, improvements in fatigue-crack growth resistance were observed in TiNb-reinforced γ -TiAl composites only in the C-L orientation; crack-growth rates for the C-R orientation were actually faster in the composite. In comparison, Nb-particle reinforcements offered less toughening under monotonic loading but enhanced the fatigue properties compared to TiNb reinforcements under cyclic loading due to more extensive debonding at the particle/matrix interface.

Similar studies on *in situ* Nb₃Al composites, processed *in house* with either equiaxed or lamellar Nb particles as reinforcements, showed a six-fold increase in fracture toughness compared to monolithic Nb₃Al; mechanistically, this can be attributed principally to crack bridging and plastic deformation in the ductile Nb phase, with additional contributions from microcracking ahead of the crack tip. Under cyclic loading conversely, the effect of the crack bridging was found to be significantly less potent due to premature fatigue failure on the ductile Nb phase; nevertheless, the composites still displayed improved fatigue-crack growth resistance compared to unreinforced Nb₃Al.

With the addition of spherical Nb particles to MoSi₂, only marginal increases in toughness compared to monolithic MoSi₂ were achieved, primarily because the cracks tended to circumvent the particles due to failure of the weak matrix/particle interfacial layer of (Mo + Nb) silicides; similarly, fatigue cracks sought a trajectory along the weak interfacial layers. Overall, these results serve to illustrate the contrasting effects of ductile reinforcements on monotonic (fracture toughness) and cyclic (fatigue) crack growth in intermetallic-matrix composites; these effects critically depend on the morphology and properties of the ductile phase, and the nature of the interface with the matrix.

Report No. UCB/R/93/A1091

Final Report

to

U.S. Air Force Office of Scientific Research

on

**MICROMECHANISMS OF MONOTONIC AND CYCLIC SUBCRITICAL
CRACK GROWTH IN ADVANCED HIGH MELTING POINT
LOW-DUCTILITY INTERMETALLICS**

Grant No. AFOSR-90-0167

for period 1 April 1990 to 31 March 1993

submitted to

U.S. Air Force Office of Scientific Research
Bldg. 410, Bolling Air Force Base
Washington, D.C. 20322
Attention: Dr. Alan H. Rosenstein

submitted by

K. T. Venkateswara Rao, L. Muruges and R. O. Ritchie
Department of Materials Science and Mineral Engineering
University of California
Berkeley, California 94720

May 1993

Accession For	
NTIS CRA&I	<input checked="" type="checkbox"/>
DTIC TAB	<input type="checkbox"/>
Unannounced	<input type="checkbox"/>
Justification	
By	
Distribution /	
Availability Codes	
Dist	Avail and/or Special
A-1	

DTIC QUALITY INSPECTED 3
DTIC QUALITY INSPECTED 2

TABLE OF CONTENTS

	Page
FOREWORD	iv
ABSTRACT	v
1. INTRODUCTION.....	1
2. FRACTURE AND FATIGUE IN γ -TiAl COMPOSITES	3
3. PROCESSING OF Nb/Nb ₃ Al <i>IN SITU</i> COMPOSITES	45
4. FATIGUE AND FRACTURE OF Nb/Nb ₃ Al <i>IN SITU</i> COMPOSITES	65
5. DUCTILE-PHASE TOUGHENING IN Nb/MoSi ₂ COMPOSITES.....	91
6. ACKNOWLEDGEMENTS	112
7. PROGRAM ORGANIZATION AND PERSONNEL	112
8. PUBLICATIONS	113
9. DISTRIBUTION LIST.....	115

**MICROMECHANISMS OF MONOTONIC AND CYCLIC SUBCRITICAL
CRACK GROWTH IN ADVANCED HIGH MELTING POINT
LOW-DUCTILITY INTERMETALLICS**

K. T. Venkateswara Rao, L. Muruges and R. O. Ritchie

(Grant No. AFOSR-90-0167)

FOREWORD

This manuscript constitutes the Final Report on Grant No. AFOSR-90-0167, administered by the U.S. Air Force Office of Scientific Research, with Dr. Alan H. Rosenstein as program manager. The work, covering the period April 1, 1990, through March 31, 1993, was performed under the Direction of Dr. R. O. Ritchie, Professor of Materials Science, University of California at Berkeley, and Dr. L. C. De Jonghe, Professor of Materials Science, University of California at Berkeley, with Dr. K. T. Venkateswara Rao as Research Engineer, L. Muruges as graduate student, and D. Nath as undergraduate engineering aide.

ABSTRACT

The next generation of high-performance engines will require stiffer materials, operating at higher stress levels and capable of withstanding significantly higher temperatures up to 1650°C and above. Prime candidates for such applications include ordered intermetallics, ceramics, and composites based on metal, intermetallic and ceramic or carbon matrices. However, these materials are currently of limited use due to their low ductility and toughness properties; moreover, an understanding of their fatigue resistance is still essentially lacking. Accordingly, the present research was aimed at examining one class of these materials, namely ductile-phase toughened intermetallic alloys, with respect to the critical factors influencing crack-propagation resistance under monotonic and cyclic loading. The model systems studied included TiNb- and Nb-reinforced γ -TiAl, Nb-reinforced Nb₃Al, and Nb-reinforced MoSi₂.

Specifically, the influence of type, volume fraction, thickness and orientation of TiNb and Nb reinforcements on the room temperature fatigue and fracture resistance of γ -TiAl intermetallic alloys was investigated. Large improvements in toughness compared to monolithic γ -TiAl were observed for composites reinforced with elongated β -TiNb and Nb particles under monotonic loading; the toughness increased with increasing ductile phase content, reinforcement thickness and strength, although orientation effects were minimal. Crack-growth behavior was characterized by steep resistance curves, primarily due to crack trapping/re-nucleation and extensive crack bridging by ductile-phase particles in the crack wake. In contrast, under cyclic loading the influence of ductile phases on fatigue resistance was seen to be strongly dependent upon reinforcement orientation. Compared to monolithic γ -TiAl, improvements in fatigue-crack growth resistance were observed in TiNb-reinforced γ -TiAl composites only in the C-L orientation; crack-growth rates for the C-R orientation were actually faster in the composite. In comparison, Nb-particle reinforcements offered less toughening under monotonic loading but enhanced the fatigue properties compared to TiNb reinforcements under cyclic loading due to more extensive debonding at the particle/matrix interface.

Similar studies on *in situ* Nb₃Al composites, processed *in house* with either equiaxed or lamellar Nb particles as reinforcements, showed a six-fold increase in fracture toughness compared to monolithic Nb₃Al; mechanistically, this can be attributed principally to crack bridging and plastic deformation in the ductile Nb phase, with additional contributions from microcracking ahead of the crack tip. Under cyclic loading conversely, the effect of the crack bridging was found to be significantly less potent due to

premature fatigue failure on the ductile Nb phase; nevertheless, the composites still displayed improved fatigue-crack growth resistance compared to unreinforced Nb₃Al.

With the addition of spherical Nb particles to MoSi₂, only marginal increases in toughness compared to monolithic MoSi₂ were achieved, primarily because the cracks tended to circumvent the particles due to failure of the weak matrix/particle interfacial layer of (Mo + Nb) silicides; similarly, fatigue cracks sought a trajectory along the weak interfacial layers. Overall, these results serve to illustrate the contrasting effects of ductile reinforcements on monotonic (fracture toughness) and cyclic (fatigue) crack growth in intermetallic-matrix composites; these effects critically depend on the morphology and properties of the ductile phase, and the nature of the interface with the matrix.

1. INTRODUCTION

Current gas-turbine engines in commercial use primarily utilize nickel-base superalloys in the hot turbine and compressor sections and primarily nickel-base and titanium alloys in the cooler compressor sections. However, since the efficiency and total thrust of a jet engine is a direct function of the peak temperature of the working fluid and current limits are set by thermal constraints on materials, these alloys are unlikely to meet the performance needs of the next generation of engines, which will require markedly stiffer materials operating at high stress levels at very much higher temperatures [1]. At present, materials are being sought which can operate at temperatures as high as 1650°C and above, although materials which can operate effectively at 1000°C would represent significant progress. Prime candidates include ordered intermetallics, ceramics and composites based on metal, intermetallic, ceramic or carbon matrices, all materials which suffer from potential problems of very low ductility, fracture toughness, and subcritical crack-growth resistance [2,3].

Much progress has been achieved over the past few years in the understanding of the mechanical, thermal and environmental behavior of such advanced high-temperature materials; however, the most significant void in this understanding still pertains to their fracture, fatigue and creep properties. Cyclic fatigue in particular has been largely overlooked, based on the widely held perception that low-ductility materials may in fact be largely immune to fatigue failure [4]. The refuted existence of a true cyclic fatigue phenomenon in these materials has been based largely on limited crack-tip plasticity. However, other inelastic deformation mechanisms, such as microcracking, phase transformation, reinforcement-phase deformation or frictional sliding between the phase and the matrix, may exist in the vicinity of the crack. In fact, recent studies by one of the authors [5-7], and others [8-11], have shown that premature fatigue failures can readily occur in ceramic and graphite/carbon materials with toughnesses as low as $1\text{-}2 \text{ MPa}\sqrt{\text{m}}$. In light of the service conditions that such intermetallic and ceramic alloys may see in future engines, it is clear that the generation of information on fatigue lifetimes and cyclic crack-growth resistance in these alloys must be regarded as extremely important; moreover, a mechanistic understanding of the primary mechanical, microstructural and environmental factors that contribute to their fracture toughness and cyclic fatigue-crack growth properties is of even greater significance.

Accordingly, the principal objective of this study was to gain a fundamental understanding of the mechanics and micromechanisms of ambient temperature fracture-

toughness and cyclic fatigue-crack propagation behavior in advanced, low-ductility intermetallic alloys. Specifically, the intent was to examine the underlying basis for crack-growth resistance under monotonic and cyclic loads in several model intermetallics in both monolithic and composite form; these include niobium aluminides (Nb_3Al), which were synthesized in-house, TiNb- and Nb-reinforced γ -TiAl intermetallics processed at Pratt and Whitney, and molybdenum disilicides (MoSi_2), which were obtained from Los Alamos National Laboratory, United Technologies and University of Michigan. This report is focused on integrating the processing and properties of such advanced low-ductility alloys with emphasis on the effect of ductile-particle reinforcements. The objective is to provide guidelines for the alloy design of new microstructures in hybrid intermetallic systems with superior resistance to incipient crack growth under both sustained and alternating loads.

1.1 References

- 1) J. J. de Luccia, R. E. Trabocco and J. F. Collins, *Adv. Mat. Proc.* **136**:5, 39 (1989).
- 2) J. D. Destefani, *ibid.* **136**:2, 37 (1989).
- 3) R. H. Jeal, *Met. Matls.* **5**, 539 (1989).
- 4) A. G. Evans, *Int. J. Fract.* **16**, 485 (1980).
- 5) R. H. Dauskardt, W. Yu and R. O. Ritchie, *J. Am. Ceram. Soc.* **70**, C-248 (1987).
- 6) R. H. Dauskardt and R. O. Ritchie, *Closed Loop* **7**, 7 (1989).
- 7) R. O. Ritchie, R. H. Dauskardt, W. Yu and A. M. Brendzel, *J. Biomed. Mat. Res.* **27**, 189 (1990).
- 8) L. Ewart and S. Suresh, *J. Mater. Sci. Lett.* **5**, 774 (1986).
- 9) S. Suresh, L. X. Han and J. J. Petrovic, *J. Am. Ceram. Soc.* **71**, C-158 (1988).
- 10) K. J. Bowman, P. E. Reyes-Marel and I.-W. Chen, in *Advanced Structural Ceramics*, MRS Symp. Proc., P. F. Becher et al. (eds.), MRS, Pittsburgh, PA (1986).
- 11) M. J. Reece, F. Guiu and M. F. R. Sammur, *J. Am. Ceram. Soc.* **72**, 348 (1989).

2. FATIGUE AND FRACTURE RESISTANCE OF DUCTILE-PHASE TOUGHENED γ -TiAl INTERMETALLIC-MATRIX COMPOSITES

(In collaboration with Dr. G. R. Odette, UCSB)

2.1 Introduction

Titanium aluminide alloys based on the ordered intermetallic compound γ -TiAl ($L1_0$ structure) are currently of considerable interest as advanced high-temperature structural materials, owing primarily to their higher specific modulus, greater elevated-temperature strength and better oxidation resistance compared to conventional titanium alloys, super-alloys and α_2 -Ti₃Al based intermetallic alloys [1-7]. The alloys are currently being developed as potential materials for use in the cooler compressor sections of high-performance turbine engines and for skin structures of hypersonic and high-speed civil transport vehicles. However, the application of monolithic γ -TiAl is severely limited by its relatively low tensile ductility ($< 2\%$) and fracture toughness ($\sim 8 \text{ MPa}\sqrt{\text{m}}$) at ambient temperatures. Accordingly, much work in recent years has focused on obtaining an understanding of the structure-property relationships in these alloys and in improving their ductility and fracture resistance.

Both alloy modification (intrinsic) and composite reinforcement (extrinsic) approaches to toughening γ -TiAl have been explored [3-11]. Microalloying with elements such as V, Cr, Mn, Mo and Nb and optimized thermomechanical processing treatments have led to toughened dual-phase microstructures composed of alternating microlaminae of γ (TiAl) and α_2 (Ti₃Al). In this case, toughening contributions arise from an intrinsic change in the deformation mechanism, i.e., mechanical twinning of the γ -phase [7], as well as crack deflection and blunting at γ/α_2 or γ/γ interfaces, and shear-ligament bridging by the more ductile α_2 phase [4-7].

Composite approaches to toughening have centered around reinforcing TiAl with small volume fractions of ductile Nb, TiNb or Ti-6Al-4V particles [8-11]. The primary objective is to enhance toughness by crack-tip shielding arising from tractions provided by unbroken ductile ligaments bridging the crack wake, akin to approaches first proposed for brittle ceramics [12-14]. When the length of the bridging zone is *very* small compared to the specimen and crack length dimensions, the toughness increases with crack extension up to a maximum steady-state level, K_{SSB} , associated with the development of a steady-state bridging zone length, L_{SSB} . At this small-scale bridging limit, K_{SSB} is given as [11]:

$$K_{SSB} = \sqrt{K_I^2 + E' f t \sigma_0 \chi} \quad (1)$$

where K_I is the critical crack-tip stress intensity factor required to initiate crack growth, E' is the plane-strain elastic modulus of the composite ($= E/(1 - \nu^2)$, ν being the Poisson's ratio), σ_0 , f , t and χ refer to the yield strength, volume fraction and characteristic dimension of the reinforcement, respectively. The non-dimensional work of rupture, χ , is the area under the normalized-reinforcement stress ($\sigma(u)$)-displacement (u) function, defined as [13]:

$$\chi = \int_0^{u^*/t} \left[\frac{\sigma(u)}{\sigma_0} \right] d\left(\frac{u}{t}\right) \quad (2)$$

where u^* is the critical crack-opening displacement at the point of reinforcement rupture. The characteristic dimension, t , is appropriately defined based on the reinforcement geometry; i.e., the diameter of a fiber, the average diameter of circles inscribing a sphere, or the thickness of a foil (lamina) or a pan-cake shaped reinforcement. Typical values of χ for γ -TiAl reinforced with Nb or Nb-alloys range between 0.9 to 1.5. Much larger values of χ , up to 4 or more, can be obtained using strain-hardening reinforcements that undergo extensive debonding from the matrix [9]. For nominal values of $\chi = 1.2$, $\sigma_0 = 400$ MPa, $E' = 190$ GPa, $t = 100$ μ m and $K_I = 8$ MPa \sqrt{m} , the addition of a mere 20 vol.% of ductile particles ($f = 0.2$) yields K_{SSB} values of about 44 MPa \sqrt{m} , over five times the nominal TiAl toughness of 8 MPa \sqrt{m} . Additional toughening mechanisms include crack trapping, crack renucleation, crack deflection and branching, and process-zone phenomena such as microcracking and twinning. Many of these latter contributions are incorporated into K_p , which is larger than the intrinsic K_{Ic} toughness of the brittle γ -TiAl matrix.

Despite the success in toughening γ -TiAl with ductile-phase reinforcements, the composites may have lower crack-growth resistance under cyclic fatigue conditions [15,16] than monolithic γ -TiAl, as illustrated in Fig. 2.1. Under monotonic loads, the γ -TiAl + 10 vol.% TiNb composite exhibits an initiation toughness of about 16 MPa \sqrt{m} , nearly twice that of pure γ -TiAl (Fig. 2.1(a)); the fracture resistance increases with further crack extension (referred to as resistance-curve or R-curve behavior) primarily due to bridging by unbroken TiNb ligaments in the crack wake (Fig. 2.1(b)). In contrast, the diminished role of crack bridging under cyclic loads due to subcritical fatigue failure of the ductile TiNb phase (Fig. 2.1(d)), can lead to marginally faster crack velocities in the composite compared to unreinforced TiAl (Fig. 2.1(c)).

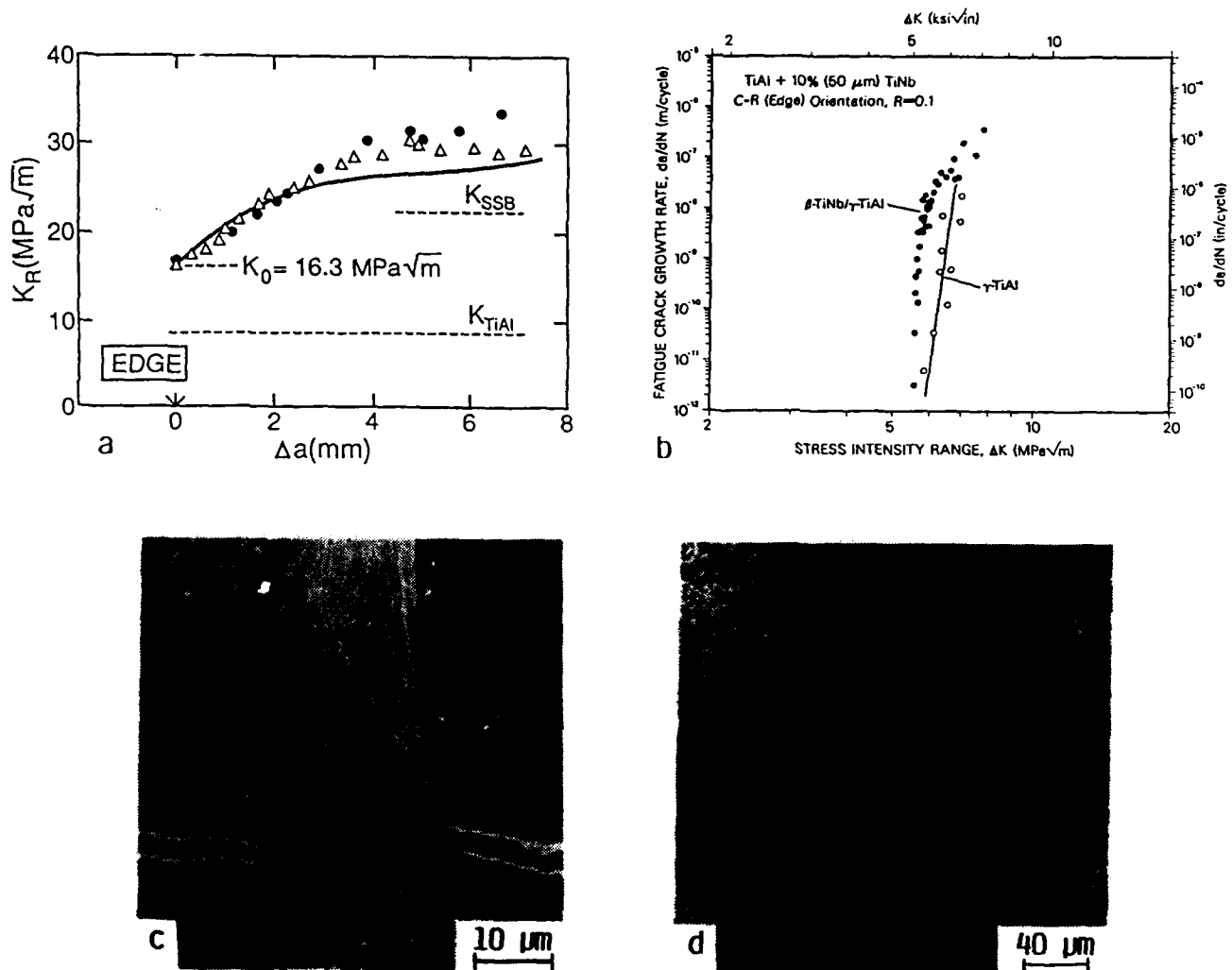


Fig. 2.1: Illustration of the contrasting role of ductile reinforcements on crack-growth behavior in a β -TiNb/ γ -TiAl composite, showing (a) improved toughness compared to γ -TiAl under monotonic loading, due to (b) crack bridging by uncracked TiNb ligaments, and (c) faster growth rates in the composite under cyclic loading, (d) due to premature failure of the TiNb particles [after ref. 15].

Accordingly, it is the objective of the present paper to provide an extensive evaluation of ductile-phase toughening in γ -TiAl intermetallic-matrix composites by systematic measurements of the influence of volume fraction, thickness, orientation and type of reinforcement on their fatigue and fracture toughness properties. Specifically, a comparison of Nb and TiNb ductile phases provides the opportunity to evaluate the effects of widely different interface and reinforcement constitutive properties on the monotonic and cyclic crack-growth resistance of ductile-phase toughened composites.

2.2 Materials and Experimental Procedures

2.2.1 Materials and Fabrication

The ductile-phase toughened composites under study, listed in Table 2.1, were fabricated by phase blending -80 mesh γ -TiAl (Ti-55 at.% Al, with small additions of Nb, Ta, C and O) with various amounts of single-phase β -TiNb (Ti-33 at.% Nb) or pure Nb powders of -35+50 mesh (nominal size ~ 300 -500 μm) or -50+140 mesh (nominal size ~ 100 -300 μm). The blends were hot pressed and forged to upset ratios of 10:1 at $1025 \pm 15^\circ\text{C}$, producing a pancake-shaped ductile particle morphology. Assuming a uniform thickness of $\sim 10\%$ of the particle diameter, the nominal aspect ratio of the pancaked reinforcements is about 5:1 and the nominal particle thicknesses are ~ 40 and ~ 20 μm for -35+50 and -50+140 mesh powders, respectively.

Table 2.1. Details of Ductile-Phase Toughened γ -TiAl Composites

Reinforcement	Mesh Size	Nominal Reinforcement Volume Fraction	Nominal Reinforcement Thickness (μm)
TiNb	-35+50	0.05	40
TiNb	-35+50	0.10	40
TiNb	-35+50	0.20	40
TiNb	-50+140	0.20	20
Nb	-35+50	0.20	40

The actual microstructures, however, were much more irregular, as illustrated in Figs. 2.2 and 2.3, and consisted of a distribution of irregularly shaped, lenticular-crenulated particles. Volume fractions and characteristic dimensions of the ductile particles were heterogeneous, both between specimens and locally within a specimen.

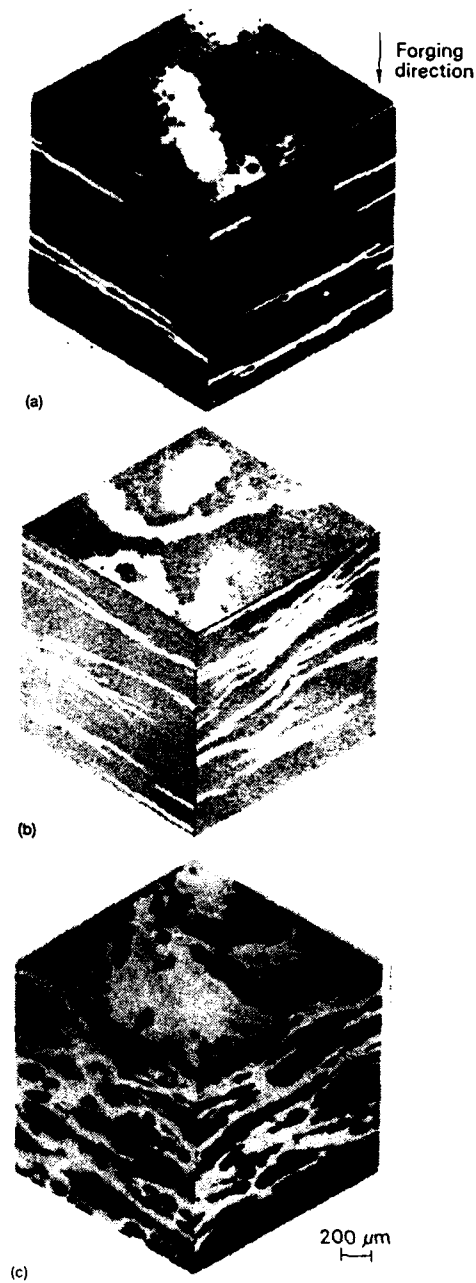


Fig. 2.2: Three-dimensional optical optical micrographs of typical γ -TiAl intermetallic-matrix composite microstructures reinforced with (a) 5 vol.%, (b) 10 vol.%, and (c) 15 vol.% of TiNb phase; the TiNb particle thickness is $\sim 40 \mu\text{m}$.

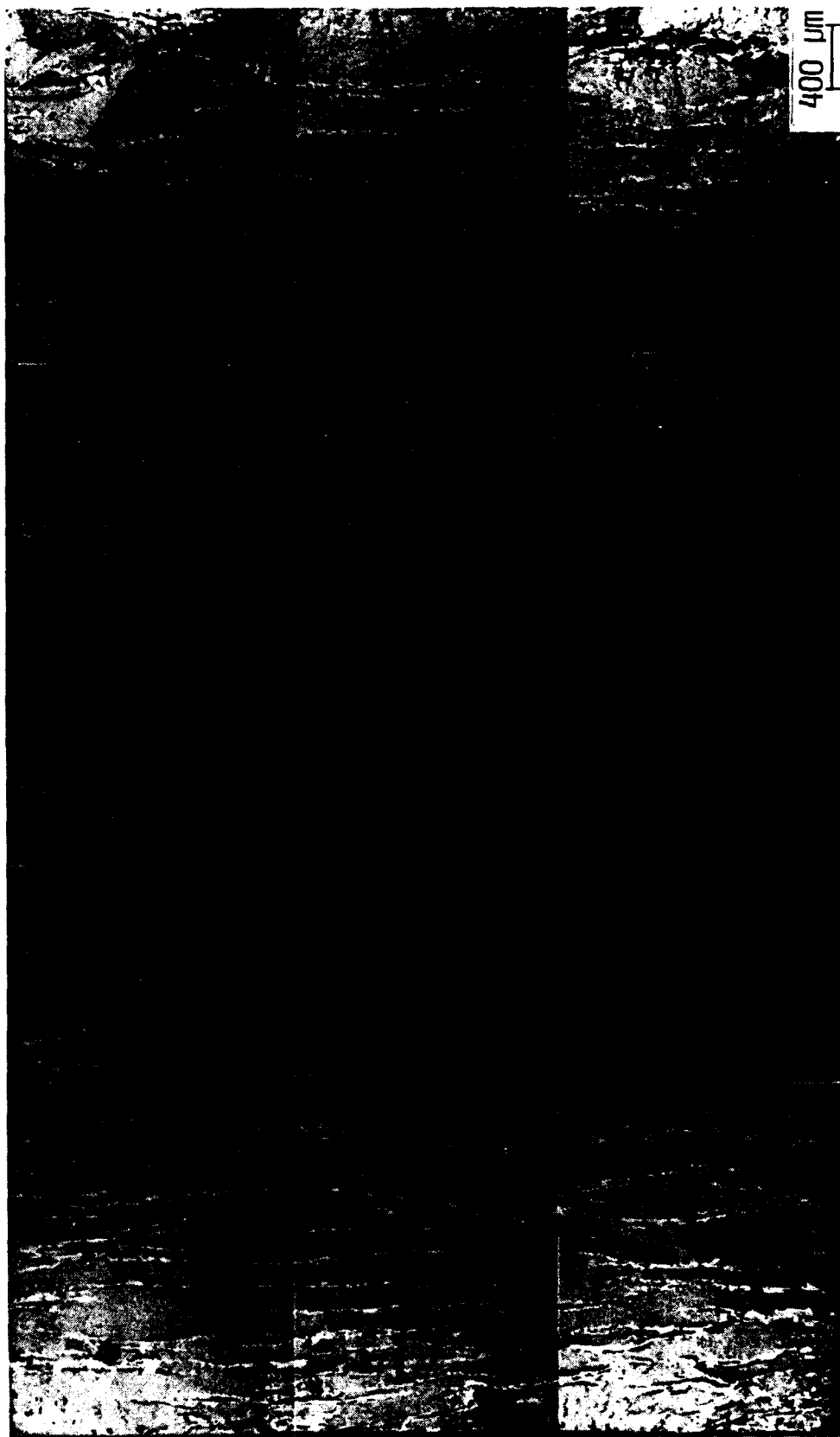


Fig. 2.3: Montage of SEM micrographs of the fractured surfaces of TiAl + 20 vol.% TiNb composite showing the distribution of ruptured ductile TiNb particles. Note the variations in particle thickness and the non-uniformity of their distribution.

Measurements along the cracked edge and on the fracture surface of representative specimens (Fig. 2.3) showed a rather wide range of particle thicknesses (between 50-150% of nominal values) and aspect ratios in part due to the particle-size distribution and irregularities in particle shape. Furthermore, unusually thick reinforcements resulted when two particles were welded during processing, more frequently so at the higher volume fractions. Local fracture-surface area fractions of the ductile phase, taken along 500 μm slices, were found to vary by up to a factor of 2; however, specimen averages were generally within a few percent of the nominal values. Henceforth, the discussions will reference nominal reinforcement parameters, recognizing that these are surrogate measures for more complex distributions.

The matrix consisted primarily of $\sim 2\text{-}10\ \mu\text{m}$ -sized grains of $\gamma\text{-TiAl}$ (ordered L1_0 tetragonal structure) with small regions of $\alpha_2\text{-Ti}_3\text{Al}$ (ordered hexagonal DO_{19} structure). Yield and ultimate strengths for unreinforced $\gamma\text{-TiAl}$ range between 400-500 MPa at room temperature with a tensile elongation of $\sim 1.8\%$ [3,4]. While the yield strength (σ_0) of the TiNb phase is about 430 MPa, this solid-solution hardened Ti-Nb alloy does not post-yield harden (strain-hardening exponent, $n \sim 0$). Thus, deformation in the TiNb phase is highly localized and the measured fracture strains strongly depend on specimen geometry and gauge length. Niobium, on the other hand, has a lower yield strength of about 140 MPa, but strain hardens extensively with an initial exponent of $n \sim 0.3$, reaching an ultimate strength (σ_u) of 250 MPa before failing at a nominal fracture strain of ~ 0.45 [9].

2.2.2 Interface Characteristics

Thermomechanical processing at high temperatures caused interfacial reactions between the $\gamma\text{-TiAl}$ matrix and TiNb and Nb reinforcements (Fig. 2.4). The $\sim 5\text{-}10\ \mu\text{m}$ thick reaction product layer between TiNb and TiAl was composed of α_2 ($\sim 3\text{-}5\ \mu\text{m}$) separated by a sharp boundary from a mixed region ($\sim 2\text{-}5\ \mu\text{m}$) of α_2 and B_2 (ordered), and possibly some ω (B8_2) phase. Transmission-electron microscope (TEM) observations in Fig. 2.4(e) also indicated the presence of dislocations in ductile α_2 grains within the TiNb/TiAl reaction layer interface. The corresponding Nb/TiAl interface consisted of a $\sim 1\text{-}2\ \mu\text{m}$ brittle σ (D_8) region and thinner layers of T_2 (Ti-44Al-11Nb at.%) and δ (Nb_3Al -A15 structure) adjacent to TiAl and Nb phases, respectively. In addition, microcracks were observed in the relatively brittle (dislocation- and twin-free) σ grains (Fig. 2.4(b)). The reaction-layer phases are critical in mediating the interface toughness, debonding characteristics and resultant constrained-deformation behavior of the reinforcing phase; results are summarized in Table 2.2.

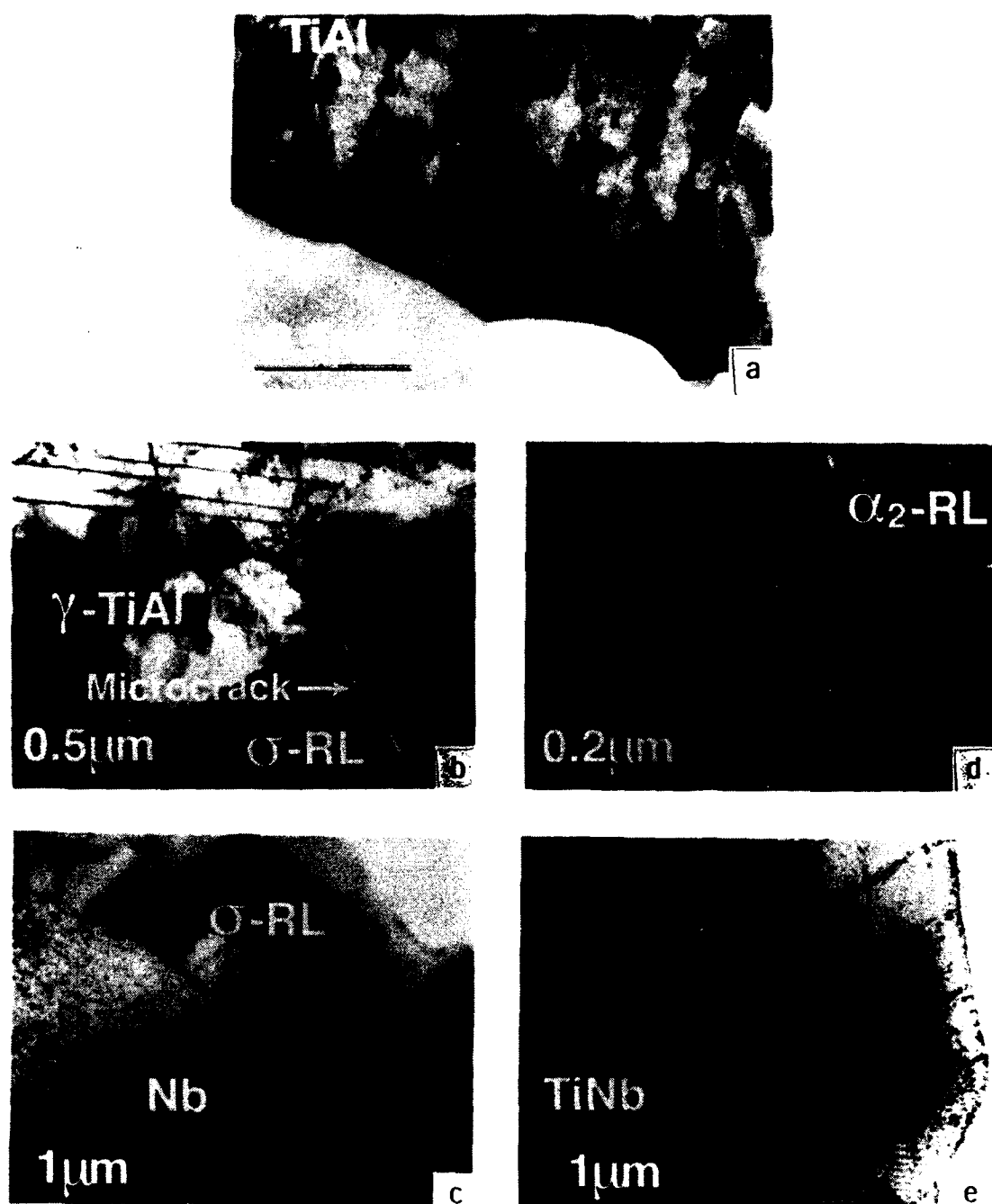


Fig. 2.4: Transmission electron microscope images of the reaction-layer interface characteristics between (a-c) Nb and γ -TiAl, and (d,e) β -TiNb and γ -TiAl.

Table 2.2 Summary of Interfacial Properties between TiNb/TiAl and Nb/TiAl

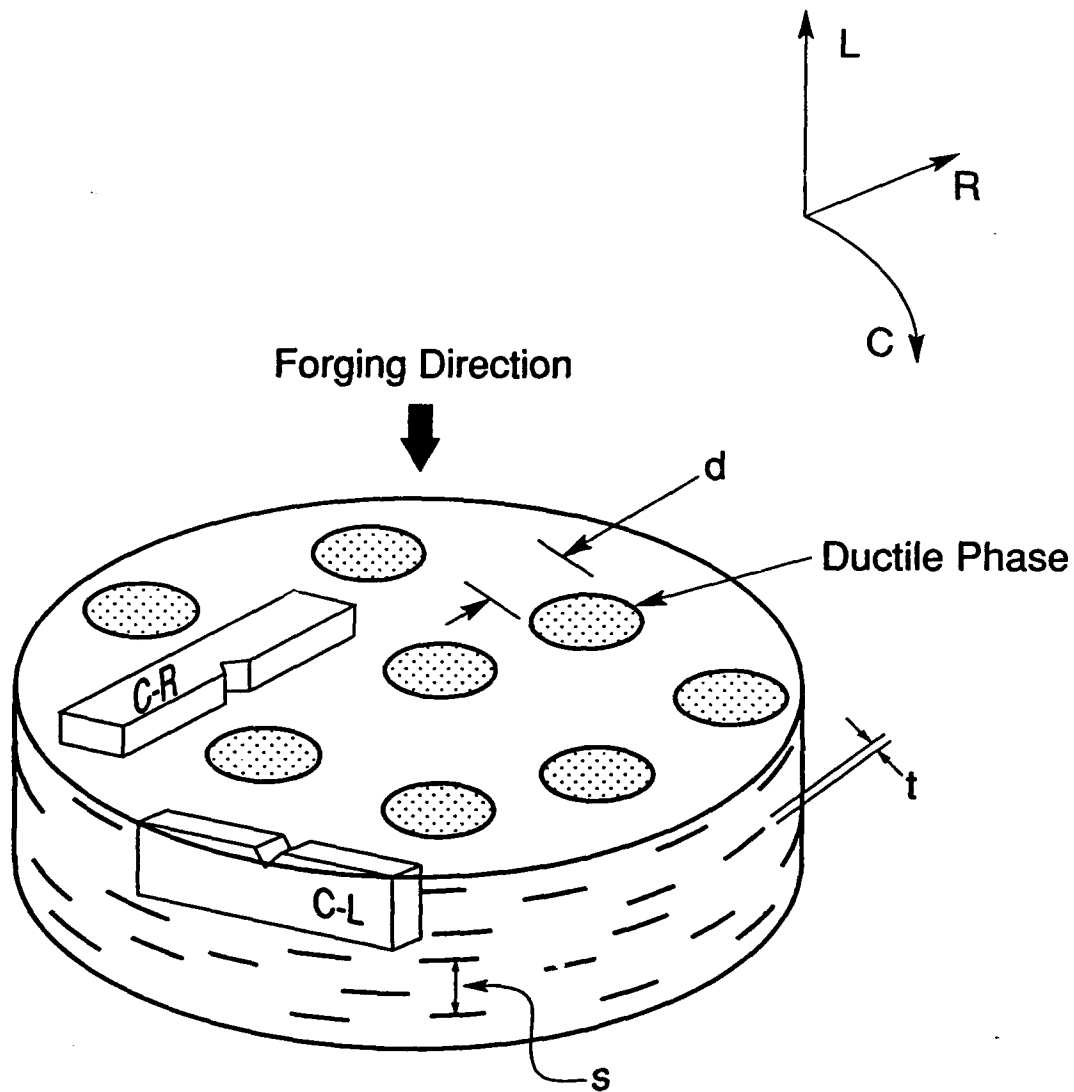
Interface	Interface Phase	Maximum Stress σ_{max}/σ_0	Critical Displacement u^*/t	Debond Length l_d/t	Work of Rupture χ	Interfacial Fracture Energy $\Gamma_i(\text{J/m}^2)$
TiNb/ γ -TiAl	α_2	2.2 ± 0.3	0.7 ± 0.2	< 0.2	1.1 ± 0.2	> 330
Nb/ γ -TiAl	σ	1.8 ± 0.2	1.1 ± 0.3	1.0 ± 0.3	1.3 ± 0.3	~ 45

In the case of Nb/TiAl, the brittle σ reaction-layer phases result in a significant amount of debonding; the interfacial toughness is estimated to be about 45 J/m² [9]. Typical debond length to particle thickness ratios (l_d/t) were roughly unity compared to values of about 4 reported for laminate foils [9]. This difference is probably due to the irregular shape and smaller thickness of the particles in the composite. However, in either case, the effect of matrix constraint on $\sigma(u)$ is minimal and the peak stress (σ_{max}) and normalized failure displacement (u^*/t) are equivalent to the corresponding ultimate strength and total elongation strains measured in geometrically-similar tensile tests; values of σ_{max}/σ_0 and u^*/t for the Nb particles are ~ 1.8 and 2.2 , respectively.

In contrast, only minimal particle debonding ($l_d/t < 0.2$) was observed for the TiNb/TiAl composites compared to values of 0.75 ± 0.25 observed in sandwich tests [9], again the variation being attributable to the particle thickness and shape. Debond cracking occurred in the γ -TiAl matrix or γ/α_2 interface, suggesting a reaction-layer toughness in excess of ~ 330 J/m². Particle constraint factors cannot be measured directly but are expected to be at least comparable to values between 2-2.5 measured in sandwich tests; in fact, the constraint may be even higher due to the minimal debonding. The critical crack-opening displacements, u^*/t , were ~ 0.7 .

2.2.3 Fracture Toughness Testing

The fracture toughness behavior of TiNb/TiAl and Nb/TiAl composites was characterized in terms of $K_{IC}(\Delta a)$ resistance curves, i.e., toughness as a function of crack extension. Specimens were fabricated by electro-discharge machining in two different orientations relative to the forging direction [17], namely, C-R and C-L (Fig. 2.5). The crack intersects the *edges* of the pancake-shaped particles in the C-R orientation; in the C-L configuration the crack intersects the *faces* of the pancakes [11]. Hence, C-R and C-L



XBL 9010-3363

Fig. 2.5: Nomenclature for specimen and reinforcement orientations in the composite forging, namely C-R and C-L; L, C and R refer to the forging, circumferential and radial directions, respectively. C-R and C-L are also referred to as the *Edge* and *Face* orientations, respectively.

are subsequently referred to as the edge and face orientations, respectively. Tests were conducted using ~5 mm thick and 12.7 to 15.2 mm wide, pre-cracked, single-edge notch bend SE(B), TiNb/TiAl composite specimens, with a span-to-width ratio of about 3:1, loaded in three-point bending; the Nb/TiAl samples were 2.5 mm thick and 7.5 mm wide. To facilitate a direct comparison of the extrinsic toughening behavior in the various composites, a set of 7.5 mm wide TiNb/TiAl specimens were also tested.

Pre-cracking was achieved by initiating stable crack growth from the electro-discharge machined chevron notch by slow monotonic loading, under displacement control, using a servo-hydraulic testing machine. Subsequently, a major portion of the pre-crack bridging zone was removed by grinding the crack wake to within ~50 μm behind the crack front. The final pre-crack depth to specimen width ratio (a_0/W) varied from about 0.3-0.5 for the various test samples.

R-curve tests were carried out by monotonically loading the pre-cracked samples under displacement control in laboratory air (~22°C, ~45% relative humidity) until crack extension was initiated. Crack lengths and crack/particle interactions were monitored using a high-resolution optical video camera system. In general, crack initiation was followed by a load drop and crack arrest after a small yet rapid uncontrolled jump. Automated detection of these load drops or direct observation of crack extension was used to trigger additional unloading, by about 15%, to further stabilize cracking. After measuring the new crack length (and recording other relevant observations), loads were again increased until the next initiation event. Applied load and crack-length measurements were used to calculate the initiation/re-initiation stress intensities (K_I) according to ASTM Standard E-399 [17]. The complete resistance curve was evaluated up to a/W ratios >0.8 by carrying out a large number of interrupted initiation/arrest (loading/unloading) cycles.

It is important to emphasize that small-scale bridging conditions, stipulated by the model in Equation 1, are seldom met in practice especially under monotonic loading. For the TiNb/TiAl and Nb/TiAl composites studied in this work, monotonic bridging-zone lengths are often comparable to specimen and crack size dimensions, i.e., large-scale bridging conditions are prevalent; specimen widths in excess of 500 mm would, therefore, be needed in some cases to fulfill small-scale bridging requirements. Crack-growth behavior under large-scale bridging is a function of the entire $\sigma(u)$ function as well as K_I and E' ; moreover, the extrinsic, large-scale bridging toughness can be significantly greater than K_{SSB} and is sensitive to test specimen size and geometry. Accordingly, R-curve measurements in this study must be considered as *extrinsic* and explicitly depend both on

specimen width and initial a_0/W . While repeated tests demonstrated that results were reproducible, reinforcement heterogeneity and specimen-to-specimen differences in W and a_0/W can complicate direct comparison of $K_I(\Delta a)$ curves for the various composite architectures. Effects of these variations were mitigated, whenever possible, by comparing results for the most similar and representative test specimens and excluding data for a/W values greater than 0.8. In addition, corrections to experimental crack-growth data were made, where necessary, to account for large-scale bridging. Small-scale bridging conditions, however, may be common under cyclic loading because of the short bridging zones.

2.2.4 Fatigue-Crack Propagation Testing

Cyclic crack-growth behavior in TiNb/TiAl composites under tension-tension loading was examined primarily with 25 mm-wide, 2.5 mm-thick, compact tension C(T) specimens in the edge (C-R) orientation; approximately 1-mm thick C(T) samples were used to characterize behavior in pure TiNb. Due to limitations in the available material, corresponding properties in the face (C-L) orientation of TiNb/TiAl composites and unreinforced γ -TiAl were determined using 15 mm-wide, 2.5 mm thick SE(B) samples (span ~ 60 mm) loaded in four-point bending. Behavior in Nb/TiAl (face orientation) was examined using 2.5 mm-thick and 7.5 mm-wide samples under identical loading conditions. All specimens were fabricated with a wedge-shaped (semi-chevron) starter notch to facilitate fatigue pre-cracking, which was performed under alternating tensile loads prior to testing.

Experiments were performed in laboratory air ($\sim 22^\circ\text{C}$, $\sim 45\%$ relative humidity) on computer-controlled servo-hydraulic testing machines operating under stress-intensity control. This was achieved by continuously monitoring the crack length, to a resolution better than $\pm 5 \mu\text{m}$, using thin metallic foils bonded to the specimen surface, similar to techniques used for fatigue testing of ceramics [18,19]. Unless otherwise stated, cyclic loads were applied at a constant nominal load ratio, $R (= K_{\min}/K_{\max})$, of 0.1 and a frequency of 50 Hz (sine wave); however, additional tests at R ratios of 0.5 and 0.7 were carried out on selected composites. To characterize the crack-growth rate behavior at different stress intensities, the applied stress-intensity range, $\Delta K (= K_{\max} - K_{\min})$, was gradually increased and/or decreased using exponential load-shedding schemes (variable ΔK at constant R), with the K -gradient set to $\pm 0.1 \text{ mm}^{-1}$ [20]. Using such procedures, crack-growth rates per cycle (da/dN) ranging between 10^{-6} to 10^{-12} m/cycle were obtained; the stress-intensity range corresponding to the slowest growth rate, $da/dN \leq 10^{-12}$ m/cycle,

is operationally defined as the fatigue threshold, ΔK_{TH} , below which no appreciable crack extension is observed for specific cyclic loading conditions. Tests on Nb- and TiNb-reinforced TiAl composites were terminated under increasing- ΔK conditions, at ΔK levels marking the acceleration in crack-growth rates to very high values; for monolithic γ -TiAl, the tests ended when the specimen fractured. Cyclic crack-growth data are presented in terms of the crack-growth rate per cycle, da/dN , as a function of the applied stress-intensity range, ΔK .

Premature contact between the cracked surfaces above the minimum load (crack closure) was monitored using strain gauges mounted on the back face of the specimens; the closure stress intensity, K_{cl} , was specified by the load at the first deviation from linearity on the unloading compliance curve, reflecting initial contact between the two surfaces. Where K_{cl} exceeds K_{min} , the *local* (near-tip) stress-intensity range can be computed as $\Delta K_{eff} = K_{max} - K_{cl}$. The extent of bridging by ductile particles under cyclic loading was estimated by comparing the crack length (of a bridged crack) estimated from back-face strain compliance with equivalent values (for an unbridged crack) measured using bonded metal-foil gauges; procedures are described in ref. [21]. These global estimates were supplemented by *in situ* observations of crack/particle interactions on the specimen surface, using a high-resolution optical telescope equipped with a video camera.

2.2.5 Fractography

Profiles of crack paths in the plane of loading and crack fronts across the specimen thickness were examined by taking metallographic sections parallel and normal to the crack growth direction, respectively. These sections and all fracture surfaces were imaged using optical and scanning electron microscopy (SEM). In addition, crack-reinforcement interactions and specific fracture mechanisms were examined by SEM by periodically interrupting tests (cyclic loading) or by using an *in situ* loading stage in the microscope (monotonic loading).

2.3 Results and Discussion

2.3.1 Fracture Toughness Properties

The basic processes leading to toughening under monotonic loading in the TiAl composites examined are illustrated in Figs. 2.6 and 2.7. Specifically, Fig. 2.6 shows a typical sequence of events as the crack intersects a ductile TiNb particle in the composite:

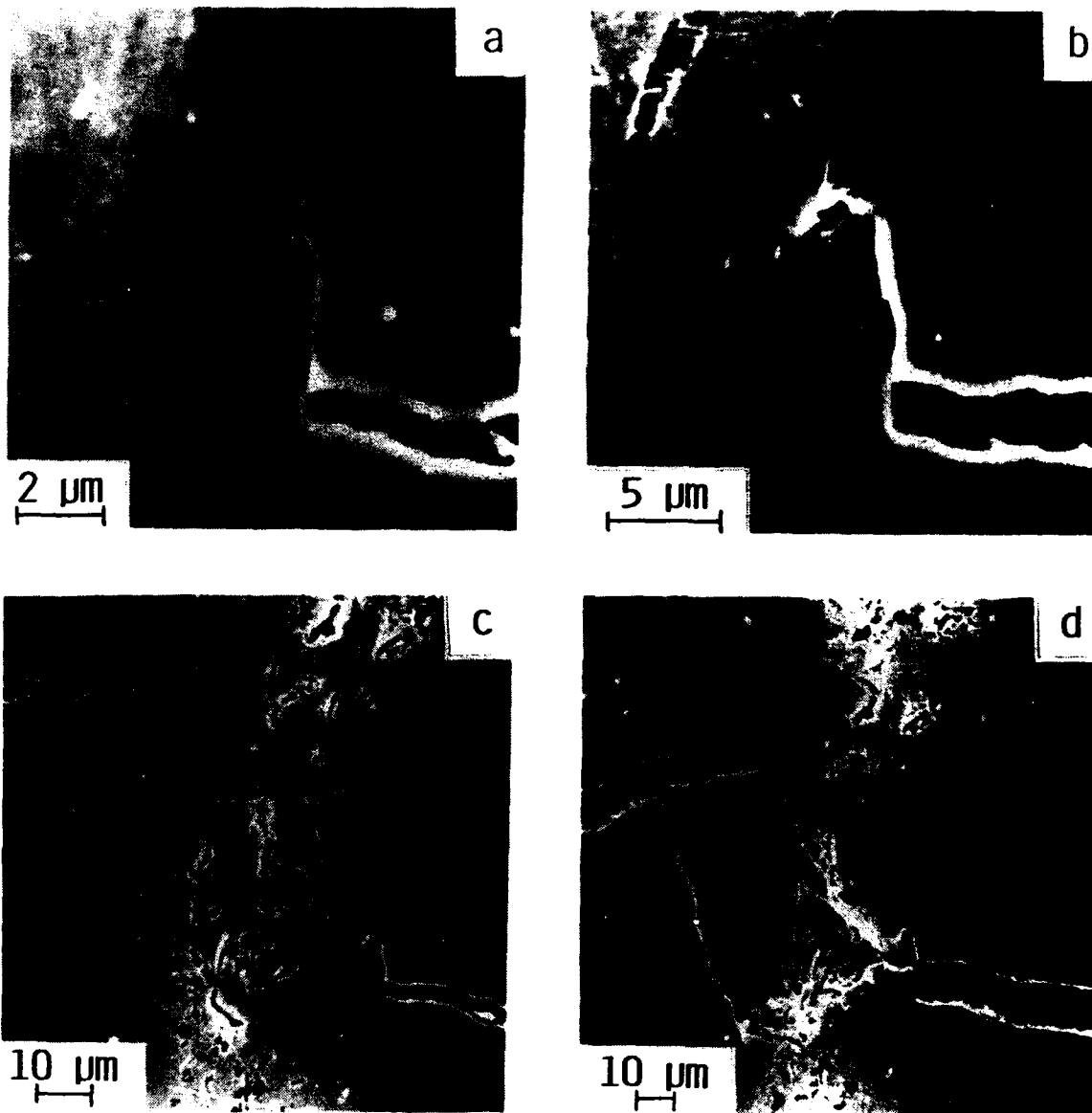


Fig. 2.6: Summary of crack/reinforcement interactions in TiNb/TiAl composites under monotonic loading, showing (a) crack arrest at the interface with minimal debonding between TiAl and the reaction layer, (b) crack-tip blunting at the TiNb particle, (c) renucleation of the crack in front of the particle leading to crack bridging, and (d) large-scale plastic deformation in the TiNb particle leading to final rupture. Images were obtained using a SEM with an *in situ* loading stage; arrow indicates the general direction of crack growth.

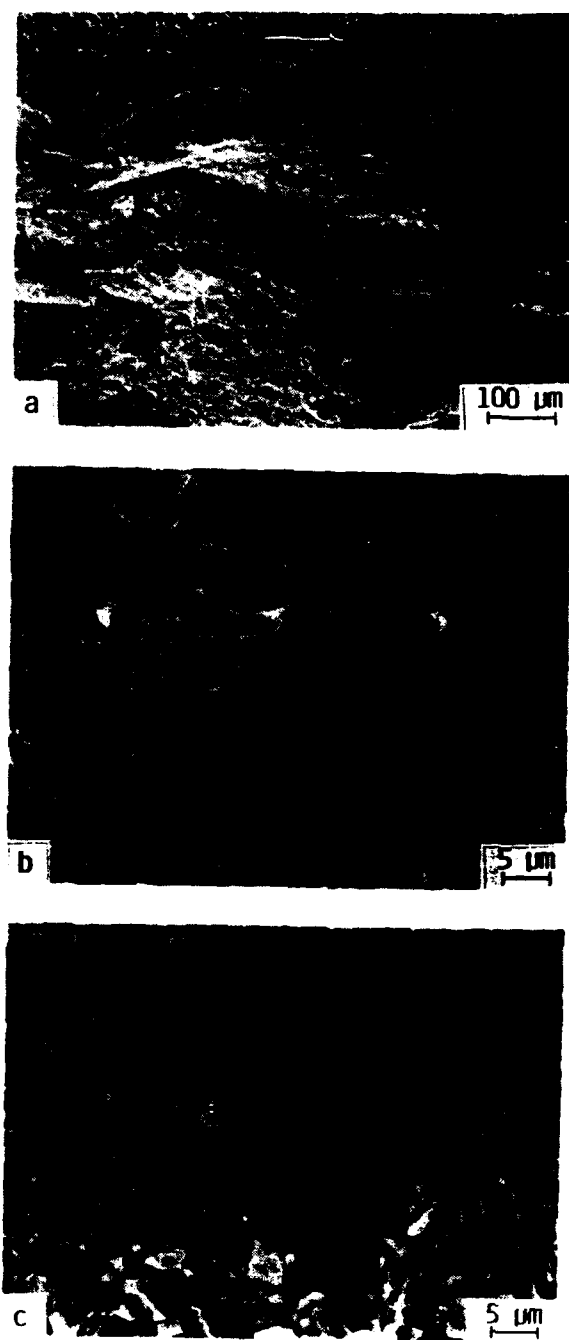


Fig. 2.7: Fractography of fracture surfaces in TiNb/TiAl composites under monotonic loading, (a-c) at various magnifications, showing (b) transgranular cleavage failures in γ -TiAl, and (c) dimpled rupture in the ductile TiNb phase. Arrow indicates the general direction of crack growth.

(a) crack arrest at the ductile α_2 layer; (b) penetration of the reaction layer and initiation of plastic deformation in the particle; (c) renucleation in the matrix ahead of the particle; and (d) large-scale deformation along intense slip bands prior to particle rupture. Note that the TiNb particles do not decohere from the matrix during crack extension but exhibit limited debond cracking along the γ/α_2 interface, as seen in Figs. 2.6(a) and 2.6(b), similar to observations made on sandwiched-composite tests [9]. The bridging zones, i.e. the length scales over which TiNb reinforcements remain intact in the crack wake, are on the order of several millimeters (Table 2.3).

The resulting composite fracture surfaces in Fig. 2.7 show minimal secondary cracking at the interface. The constituent phases exhibit similar fractographic features in composite and monolithic form; the ductile TiNb particles fail by a transgranular, microvoid nucleation and coalescence mechanism, as evidenced by the dimpled surfaces in Fig. 2.7(b). Fractures in γ -TiAl are predictably brittle, characterized by transgranular cleavage with small regions showing intergranular failure (Fig. 2.7(c)). The distribution of ruptured ductile TiNb particles dispersed over the brittle TiAl fracture surface is illustrated in Fig. 2.3.

Table 2.3. Summary of Monotonic Crack-Growth Data in γ -TiAl Composites

Reinforcement	Volume Fraction f	Particle Thickness t (μm)	Initiation Toughness K_i (MPa√m)		R-Curve Slope dK_i/da (MPa√m/mm)		Steady-State Toughness K_{SSB} (MPa√m)	Steady-State Bridge Length L_{SSB} (mm)
			Edge	Face	Edge	Face		
TiNb	0.05	40	11.3	12.7	2.1	2.5 (1.9) ¹	18.3	38.8
TiNb	0.1	40	18.6	15.7	2.5	3.3 (2.9) ¹	24.7	22.3
TiNb	0.2	40	17.3	19.0	4.2	5.0	32.6	13.7
TiNb	0.2	20	18.9	18.4	2.3	2.4 (2.2) ¹	26.6	5.3
TiNb ²	0.2	40	17.5	19.1	12.4	9.6	32.6	13.7
Nb ²	0.2	40	12.2	13.8	6.9	5.5	21.2	57.5

¹Values in parenthesis are corrected to 15.2 mm width

²7.5 mm-wide specimens

Effects of these crack-extension processes on resistance-curve behavior as a function of the ductile-reinforcement characteristics are summarized in Figs. 2.8 and 2.9; estimates of the crack-initiation toughness, K_{Ic} , and R-curve slope, dK_{Ic}/da , values based on linear least-square fits to the experimental data are listed in Table 2.3. Despite the influence of specimen size on the measured fracture properties¹, it is clear that both crack-initiation toughness and crack-growth toughness, i.e., the slope of the resistance curve, increase with ductile-phase content for the 40 μm -thick TiNb reinforcements (Figs. 2.8(a-c)). In comparison, reinforcement orientation has a minimal effect on ductile-phase toughening at lower volume fractions, particularly after specimen-size variations are considered; the toughness is marginally superior in the face orientation, compared to the edge, only for TiAl composites reinforced with 20 vol.% TiNb.

The reduction in reinforcement thickness from ~ 40 to 20 μm at a volume fraction of 0.2 decreases the slope of the resistance curve, but does not appear to have a large effect on the initiation toughness (Figs. 2.9(a), 2.9(b)). The effectiveness of Nb vs. TiNb ductile reinforcements in enhancing the monotonic fracture resistance of γ -TiAl composites, compared in Fig. 2.9(c), illustrates the significance of *effective* particle strength on toughness as mediated by the combination of yield stress, constraint (for TiNb) and strain hardening (for Nb). Specifically, the Nb particles in Nb/TiAl composites readily delaminate from the matrix during crack advance (Fig. 2.10) and relax constraint (or reduce the degree of triaxiality) during fracture compared to the highly constrained failure of TiNb ligaments in TiNb/TiAl composites (Fig. 2.6). Consequently, the higher (constrained) maximum effective strength of the TiNb reinforcements (~ 950 MPa) yield a significantly higher crack-initiation toughness and a steeper resistance curve compared to Nb additions (unconstrained, effective strength of Nb ~ 250 MPa). The larger critical opening displacement in Nb ($u^* \sim 1.1t$) versus TiNb ($u^* \sim 0.7t$) appears to have no effect on the initiation toughness and relatively little effect on crack-growth toughness in these small samples. Furthermore, little effect of orientation on toughness is noted for either reinforcement.

¹ Note that specimens in the face orientation with TiNb volume fractions of 0.05 and 0.10 were 12.7 mm-wide compared to the typical width of 15.2 mm. While the crack-initiation toughness would not be influenced by such size differences, K_{Ic} increases more rapidly with crack advance in smaller test specimens. For example, large-scale bridging calculations indicate that at crack extensions of 7 mm, the smaller specimen size increases the extrinsic toughness by $\sim 25\%$ and $\sim 13\%$ for the 5 and 10 vol.% TiNb-reinforced γ -TiAl composites, respectively.

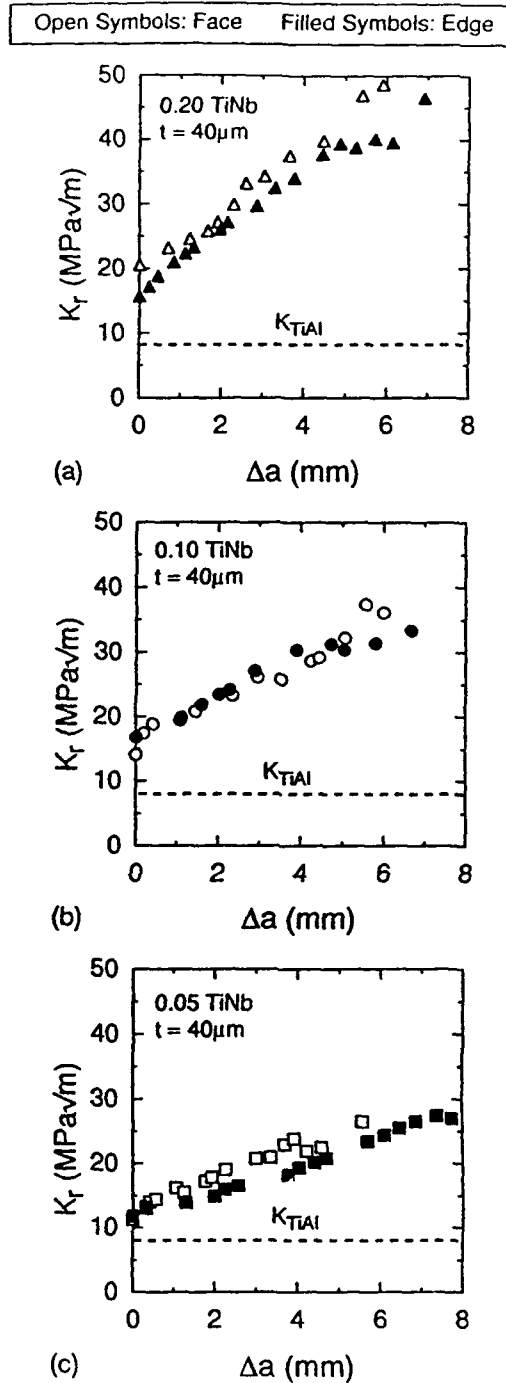


Fig. 2.8: Resistance curves characterizing the crack-growth behavior in TiNb/TiAl composites under monotonic loading, as a function of the volume fraction, (a) 20, (b) 10 and (c) 5 vol.% of TiNb phase (thickness, $t = 40 \mu m$), in the edge (or C-R, denoted by open symbols) and face (or C-L, denoted by filled symbols) orientations. Dashed line K_{TiAl} represents the toughness of pure γ -TiAl.

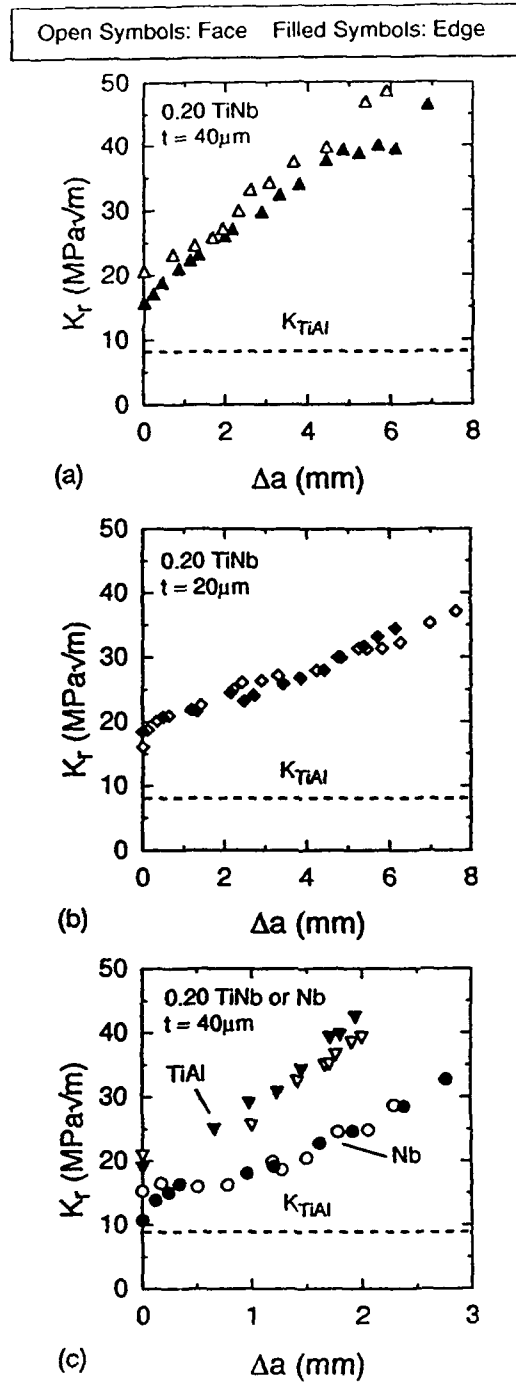


Fig. 2.9: Influence of (a,b) reinforcement thickness, t , of $20 \mu\text{m}$ vs. $40 \mu\text{m}$, and (c) reinforcement type, TiNb vs. Nb, on the monotonic crack-growth resistance of γ -TiAl intermetallic-matrix composites. Data shown are for a nominal volume fraction, $f = 0.2$, in the edge (open symbols) and face (filled symbols) orientations. Dashed line K_{TiAl} represents the toughness of pure γ -TiAl.

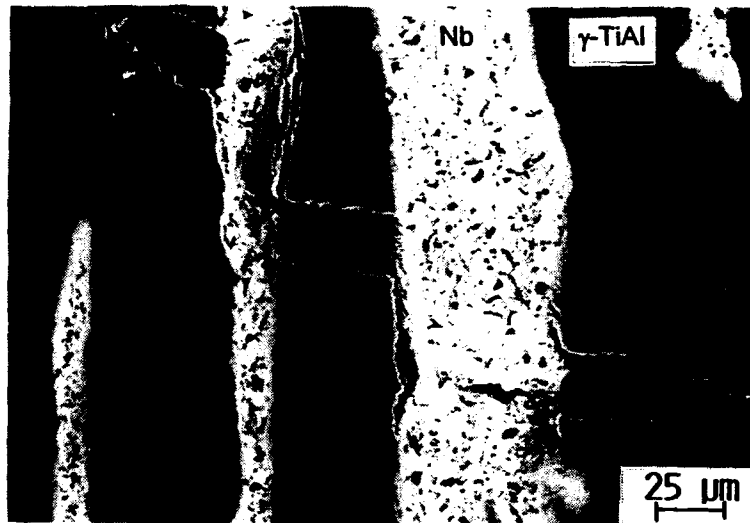


Fig. 2.10: SEM micrograph of fracture path morphologies in Nb/TiAl composites under monotonic loading. Note the extensive debonding at the interface compared to TiNb/TiAl composites.

The effects of reinforcement volume fraction (f) and thickness (t) on the apparent crack-initiation and crack-growth toughness values are more clearly shown in Figs. 2.11(a) through 2.11(c) (the small symbols in Fig. 2.11(a) represent the estimated size corrections to a common specimen width of 15.2 mm). With respect to the volume fraction of TiNb, f_{TiNb} , (Figs. 2.11(a), 2.11(b)) power-law fits yield:

$$\frac{dK_r}{da} = 10.9 (f_{\text{TiNb}})^{0.55} \quad (3)$$

$$K_i = 8 + 26.8 (f_{\text{TiNb}})^{0.5}$$

The corresponding fit of dK_r/da to the TiNb particle thickness, t_{TiNb} , yields a linear dependence (Fig. 2.11(c)). Particle thickness has little effect on crack-initiation toughness; hence, a plot of these data is not shown. Figures 2.11(d) and 2.11(e) plot the apparent crack-initiation toughness values and resistance-curve slopes versus the effective maximum reinforcement strength, yielding power-law fits:

$$\frac{dK_r}{da} = 0.58 (\sigma_{\text{max}})^{0.43} \quad (4)$$

$$K_i = 8 + 0.33 (\sigma_{\text{max}})^{0.5}$$

The extrinsic toughening behavior measured in this study cannot be analyzed using the intrinsic, steady-state, small-scale bridging model represented by Equation 1. Nevertheless, the experimental trends are *qualitatively* consistent with predictions that toughness increases with the square root of the reinforcement volume fraction and strength. The linear dependence of toughness on particle thickness is not predicted by Equation 1. The particle thickness effect on crack-growth toughness (dK_r/da) is probably a consequence of the combination of a higher effective strength (particularly in the initial portion of the R-curve) and longer extrinsic bridge length (particularly at large a/W) for the large-scale bridging conditions experienced in these tests.

One puzzling result, however, is the absence of an effect of particle thickness on the apparent initiation toughness. Recall that the elevation of K_i above the K_{Ic} value for γ -TiAl matrix is attributed to a combination of crack trapping, deflection, and renucleation mechanisms along with the presence of a small ($\sim 50 \mu\text{m}$) residual crack-bridging zone. While crack deflection contributions are not believed to be significant, the toughening

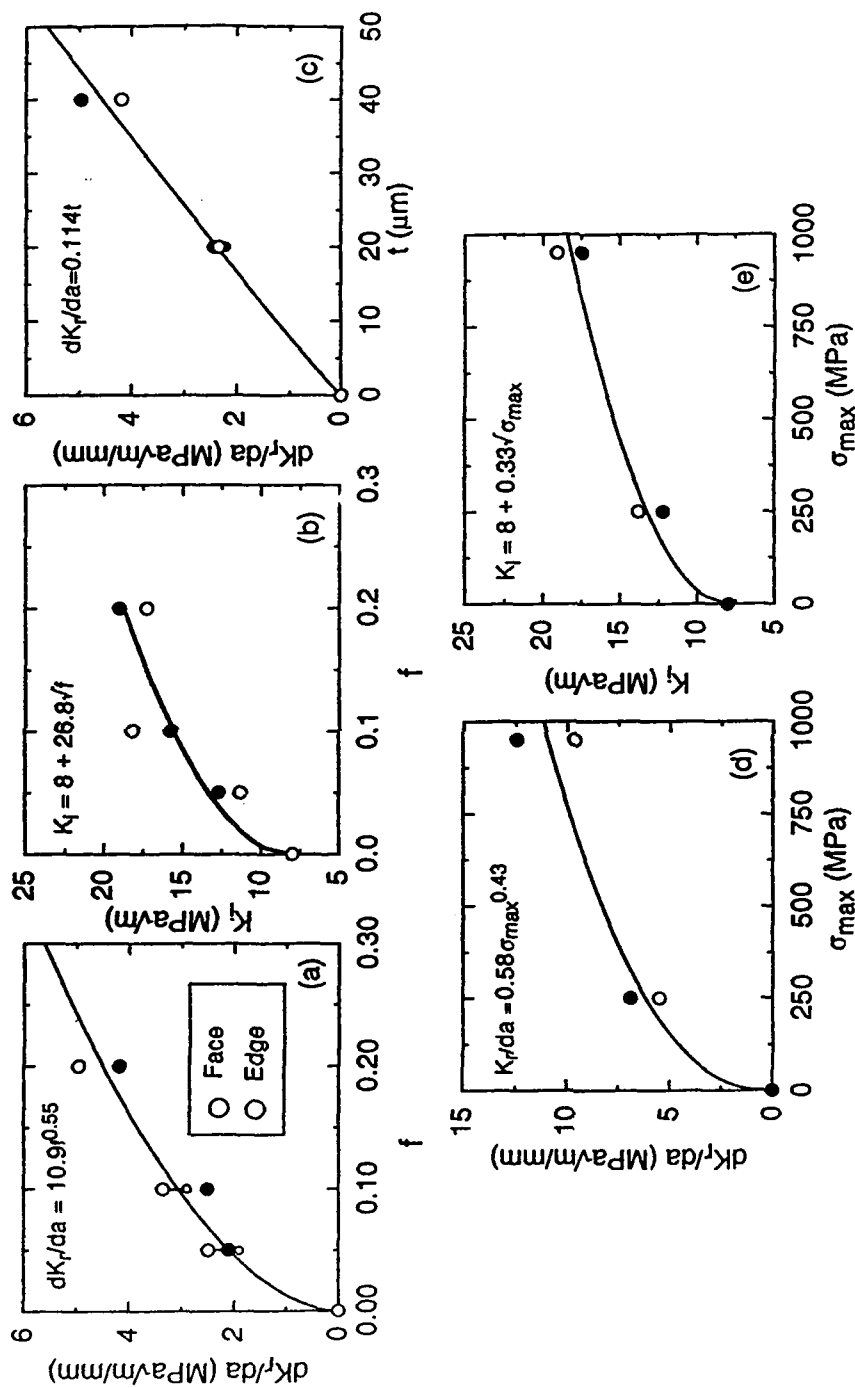


Fig. 2.11: Variations in crack-initiation toughness, K_I , and crack-growth toughness, dK_I/da , with (a,b) volume fraction f , of reinforcement phase, (c) particle thickness, t , and (d,e) reinforcement strength, σ_{max} for both Nb/TiAl and TiNb/TiAl composites.

increment associated with renucleation and residual bridging effects would be expected to scale roughly with the square root of the reinforcement thickness [11,22]. This suggests that crack trapping (pinning by ductile phases, as in the case of a tunnel crack) effects in the edge orientation may be comparable to toughening contributions from crack-renucleation mechanisms in the face orientation. More research is needed to resolve the effect of particle thickness on the apparent crack-initiation toughness.

A more rigorous analysis of these data must take into account the effects of large-scale bridging, by calculating self-consistent solutions to the crack-opening profile, $u(x)$, the distribution of tractions in the crack wake, $\sigma(x)$, and the stress-displacement function of the composite, $\sigma(u)$, where x is the distance behind from the crack tip; details are presented elsewhere [11]. Using this model, the intrinsic steady-state toughness, K_{SSB} , and steady-state bridging length, L_{SSB} , were estimated by computing the $K_I(\Delta a)$ curves up to steady-state in a very large specimen. The calculations assumed nominal reinforcement parameters given in Table 2.2; K_I and E' are approximated by the initiation toughness, K_{Ii} , and the nominal plane-strain elastic modulus of TiAl (193 GPa). The stress-displacement function for the composite is of the form:

$$\sigma(u) = \sigma_{max}(u/u_p) \quad \text{for } u \leq u_p \quad (6a)$$

$$\sigma(u) = \sigma_{max}[1 - (u/u'^*)^{0.5}] \quad \text{for } u > u_p \quad (6b)$$

where, u_p is the displacement at peak stress (taken as 2 μm), and u'^* is taken as twice the average critical particle displacement or the corresponding value measured in sandwich tests. This formulation of $\sigma(u)$ is a modification to the nearly saw-toothed stress-displacement functions measured in the sandwich tests in order to account approximately for the *distribution* of particle thicknesses in the actual composite. Results from these calculations, summarized in Table 2.3, also indicate that significant intrinsic toughening can be achieved in γ -TiAl composites even under small-scale bridging conditions. Also note the remarkably long steady-state bridging lengths under small-scale bridging conditions.

Results on crack-growth resistance curves measured under monotonic loading can be summarized as follows. Even small volume fractions of ductile reinforcements produce marked toughening due (i) the formation of large bridging zones and (ii) crack trapping and renucleation mechanisms which mediate the critical crack-tip stress intensity. The slope of the R-curve increases with reinforcement volume fraction, strength and thickness;

with the exception of particle thickness, similar trends are observed for crack-initiation toughness. Reinforcement orientation appears to have relatively little effect on the degree of toughening in these composites. Overall, the experimentally measured extrinsic toughening behavior is consistent with predictions of large-scale bridging models.

2.3.2 Fatigue-Crack Propagation Behavior

Cyclic fatigue-crack growth results in the ductile-particle reinforced γ -TiAl composites, along with data for unreinforced γ -TiAl and β -TiNb constituent phases, are plotted in Figures 2.12 through 2.14; fatigue-threshold data and other crack-growth parameters are summarized in Table 2.4. As noted in previous studies on the TiNb/TiAl system [15,16], under cyclic loading, cracks propagate subcritically at stress intensities between ~ 4 -12 $\text{MPa}\sqrt{\text{m}}$ for all γ -TiAl composite microstructures and specimen orientations, well below the K_{Ic} values necessary to initiate cracking under monotonic loading (Table 2.3). Subcritical crack propagation under cyclic loads must, therefore, be considered an important damage mode in the structural design and use of ductile-phase toughened brittle-matrix composites.

Table 2.4. Summary of Cyclic Crack Growth Data in γ -TiAl Composites

Material	Load Ratio R	Threshold ΔK_{TH} ($\text{MPa}\sqrt{\text{m}}$)	Exponent ^a <i>m</i>	Constant ^b C
γ -TiAl	0.1	5.8	29.4	9.7×10^{-31}
β -TiNb	0.1	1.7	4.6	3.0×10^{-11}
Edge Orientation				
γ -TiAl + 5% TiNb (40 μm)	0.1	4.5	17.6	5.3×10^{-18}
+ 10% TiNb (40 μm)	0.1	5.6	14.1	1.1×10^{-16}
+ 20% TiNb (40 μm)	0.1	5.0	9.6	2.0×10^{-13}
+ 20% TiNb (20 μm)	0.1	5.3	9.7	2.5×10^{-13}
	0.5	3.6	—	—
	0.7	2.6	—	—
Face Orientation				
γ -TiAl + 20% TiNb (40 μm)	0.1	8.2	6.7	1.0×10^{-15}
+ 20% TiNb (20 μm)	0.1	8.2	14.8	1.1×10^{-22}
+ 20% Nb (40 μm)	0.1	10.1	8.7	5.6×10^{-18}

^a Taken for crack growth rates between 10^{-9} and 10^{-6} m/cycle

^b Units: $\text{m/cycle} (\text{MPa}\sqrt{\text{m}})^{-m}$

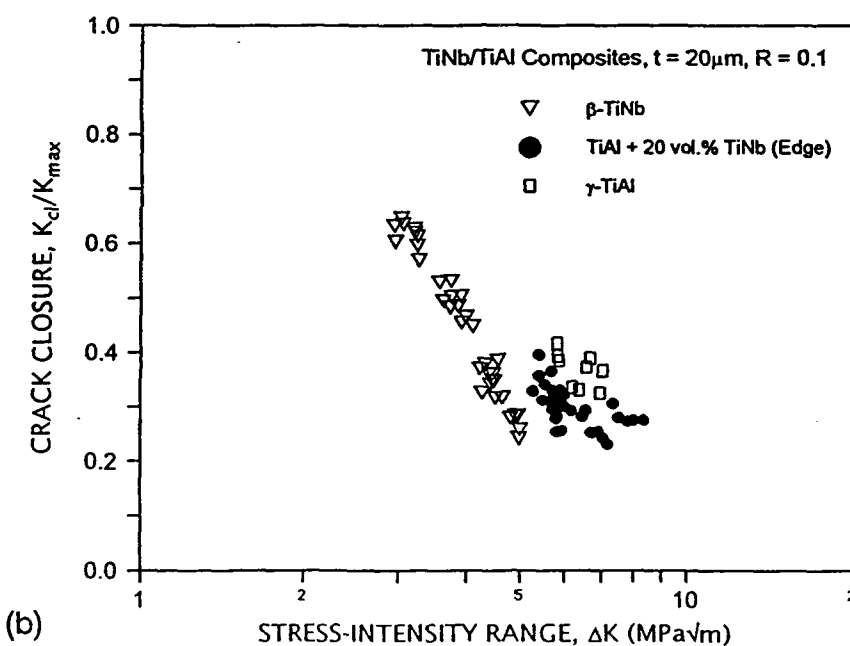
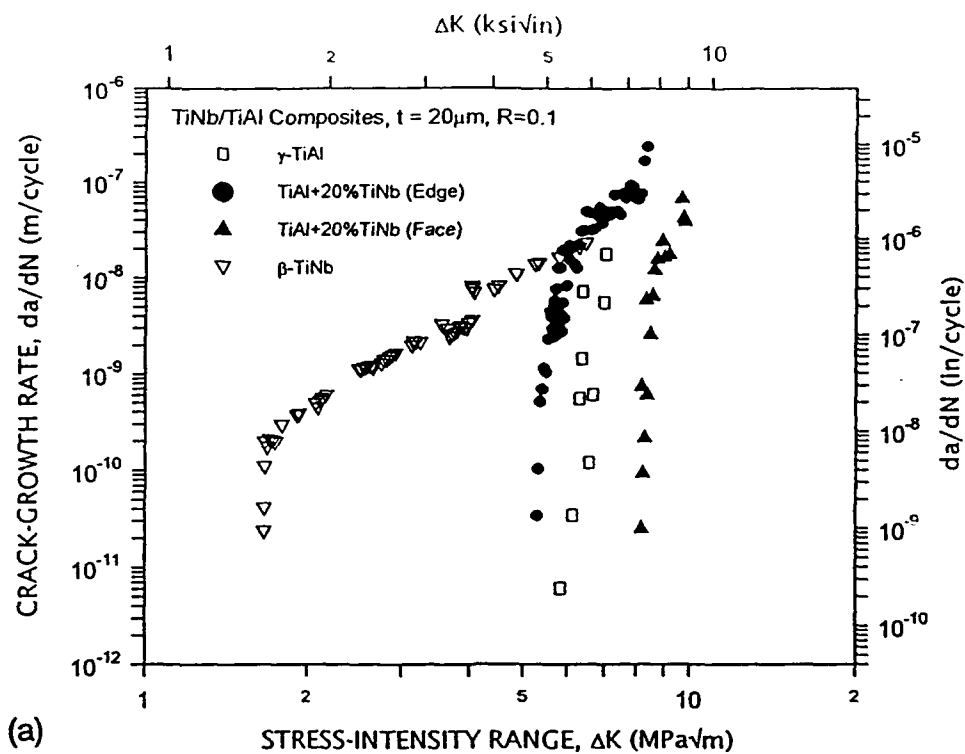


Fig. 2.12: (a) Cyclic crack propagation and (b) crack-closure behavior in a γ -TiAl + 20 vol.% β -TiNb ($t \sim 25 \mu m$) composite, in the edge (C-R) and face (C-L) orientations, at $R = 0.1$, compared with the crack-growth properties of the constituent phases, monolithic γ -TiAl and β -TiNb.

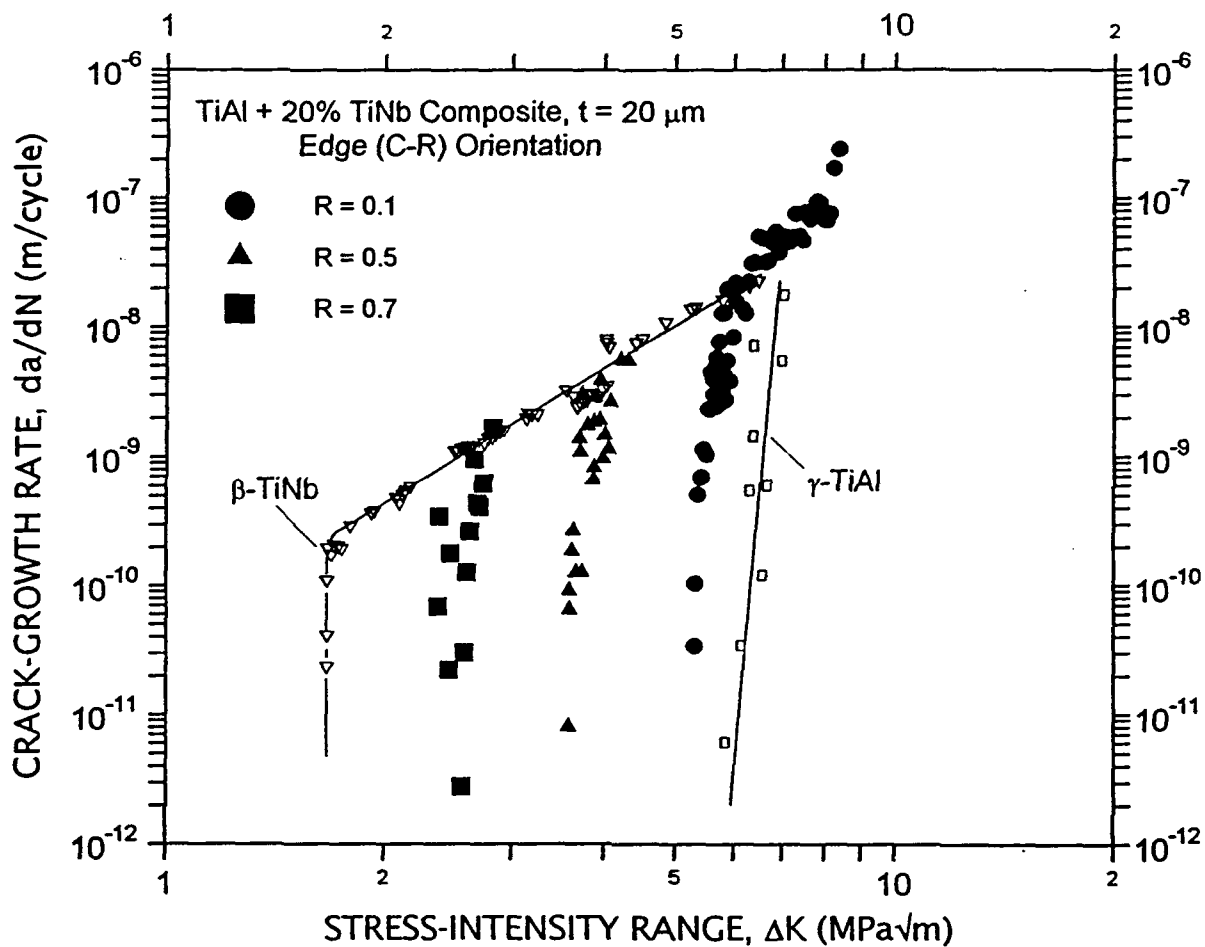


Fig. 2.13: Influence of load ratio, $R = 0.1, 0.5$ and 0.7 , on the cyclic fatigue-crack growth behavior in a γ -TiAl composite reinforced with 20 vol.% ($t \sim 25 \mu\text{m}$) TiNb particles in the edge (C-R) orientation.

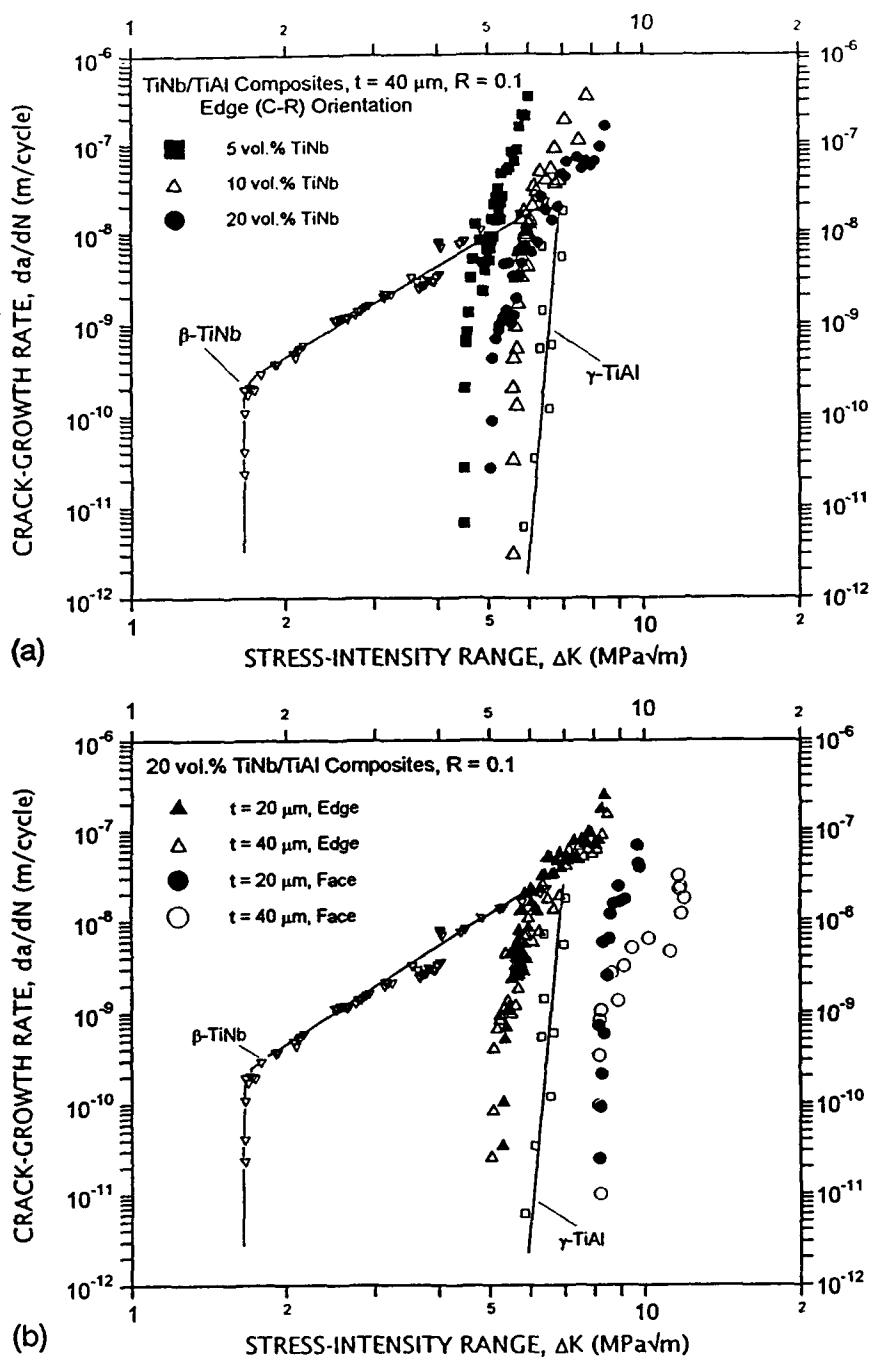


Fig. 2.14: Microstructural effects of (a) volume fraction ($t \sim 40 \mu\text{m}$) and (b) particle thickness ($f \sim 0.2$) on the cyclic fatigue-crack propagation resistance of TiNb/TiAl composites in the edge (C-R) orientation, at $R = 0.1$.

The general features on da/dN - ΔK curves for the composites resemble those seen for most metallic materials with a low-growth rate region (region I) at ΔK levels close to the fatigue threshold, where the rate of crack advance strongly depends on applied ΔK , followed by an intermediate- or mid-growth rate region (region II) where this dependence is moderate. However, unlike behavior in metals, crack-growth behavior for the γ -TiAl composites in this mid-growth rate regime (da/dN typically between $\sim 10^{-9}$ to 10^{-6} m/cycle) is still very sensitive to the applied ΔK , especially at low volume fractions. In fact, when expressed in terms of the empirical Paris power-law relationship that is often used to describe this region:

$$da/dN = C \Delta K^m \quad (7)$$

the exponent m ranges between 10-20 for the various composites, compared to values of ~ 2 -4 that are typically reported for monolithic metallic materials; $m \sim 4.6$ for pure β -TiNb (Table 2.4, Fig. 2.12(a)). In other words, the mid-growth rate (power-law) regime of cyclic crack growth is relatively small for ductile-phase toughened TiAl composites and virtually non-existent for unreinforced γ -TiAl ($m \sim 30$). At high ΔK levels approaching the initiation toughness, K_I (high-growth rate regime, region III), a rapid increase in crack-extension rates is seen for small changes in ΔK , similar to behavior near the fatigue threshold.²

Orientation Effects for TiNb/TiAl Composites: Figure 2.12(a) depicts the cyclic fatigue-crack growth data for the edge and face orientations in the γ -TiAl composite reinforced with 20 vol.% of ~ 20 μ m-thick TiNb particles. Specifically, in the edge orientation, region I fatigue-crack growth rates in the composite are faster than in unreinforced γ -TiAl and much slower than in pure β -TiNb. The near-threshold cyclic crack-growth behavior ($da/dN < 10^{-9}$ m/cycle) of the composite is essentially bounded by properties of the individual phases. In region II, growth rates in the edge-orientation of the composite are comparable to those measured in monolithic β -TiNb.

However, Figure 2.12(a) also reveals that the crack velocities in the TiNb/TiAl composite for the face (C-L) orientation are slower than in γ -TiAl; in fact, the composite fatigue properties are superior to both unreinforced TiAl and TiNb. Thus, unlike the response under monotonic loading, the reinforcement orientation has a marked effect on cyclic crack-growth behavior. More importantly, these results clearly demonstrate that the

² It should be noted that fatigue-crack growth behavior in the high- ΔK regime has not been fully characterized in this study due to the rapid crack velocities inherent with the test frequencies of 50 Hz used for cyclic loading.

incorporation of ductile reinforcements *can* enhance the cyclic fatigue-crack propagation resistance of brittle γ -TiAl intermetallic alloys, in addition to improving fracture toughness. However, the magnitude of improvement is relatively small, indicated by $\sim 2 \text{ MPa}\sqrt{\text{m}}$ shift in the entire da/dN - ΔK curve compared to the nearly five-fold increase in toughness seen under monotonic loads, and is seen only for specific orientations i.e., where the crack periodically encounters the pancake faces of ductile particles. Similar reinforcement-orientation effects are also observed in other TiNb/TiAl composite microstructures (Fig. 2.14(b)).

Corresponding measurements of the extent of crack closure in the TiNb/ γ -TiAl composites and their two unreinforced constituents are shown in Fig. 2.12(b) in terms of the closure stress intensity, K_{cl} , normalized by K_{max} , as a function of ΔK . The K_{cl}/K_{max} values in the edge orientation of composite are slightly lower compared to TiAl in the edge orientation suggesting faster growth rates due to increased ΔK_{eff} values locally at the crack tip; no such distinction is apparent in the face orientation. Although such variations are partly consistent with observed reinforcement-orientation effects on cyclic crack growth, closure effects do not appear to completely account for the differences in crack-growth rates between the composite and monolithic alloys. Specifically, at high ΔK levels where the influence of closure is minimal, cracks propagate faster in the edge-oriented composite than in pure γ -TiAl or β -TiNb (Fig. 2.14a). As such, it seems more likely that variations in cyclic crack-growth rates are primarily attributable to differences in intrinsic mechanisms of cyclic crack advance in these microstructures.

Load Ratio Effects: The effect of load ratio ($R = K_{min}/K_{max}$) on cyclic crack-growth rates, in the 20 vol.% TiNb/ γ -TiAl composite in the edge (C-R) orientation, is shown in Fig. 2.13. Compared to a baseline of $R = 0.1$, load ratios of 0.5 and 0.7 reduce the fatigue threshold stress-intensity values by about 27 and 51%, respectively. This phenomenon is consistent with behavior observed in many metallic materials [23], where increasing R accelerates crack-growth rates for a given ΔK , especially in the near-threshold and high- ΔK regions. Although the marked sensitivity to applied ΔK in the threshold regime is essentially unchanged, higher load ratios suppress the intermediate growth-rate regime (region II) separating the behavior at near-threshold and high stress intensities. The latter occurs at K_{max} of ~ 8.5 - $9.3 \text{ MPa}\sqrt{\text{m}}$, slightly in excess of the matrix K_{Ic} of $\sim 8 \text{ MPa}\sqrt{\text{m}}$, and is independent of the load ratio.

As noted above, premature crack closure is observed to occur in the composites at stress intensities above K_{min} , presumably from the wedging of fracture-surface asperities

including any intrinsic bridging ligaments or broken remnants, e.g., at threshold, K_{cl} is $\sim 0.4 K_{max}$. As a result, for load ratios below 0.4, such closure causes a net increase in K_{min} or a reduction in the driving force from the nominal (applied) value of ΔK to a local "near-tip" value ΔK_{eff} , thereby resulting in slower crack-growth rates. At high R , closure effects are minimal ($K_{min} > K_{cl}$) and the crack remains open during the entire loading cycle; accelerated crack-growth rates are thus to be expected. From these considerations, load ratio effects on cyclic crack growth in the composite are expected to be small for $R > 0.4$, since K_{cl} is at least $\sim 0.4 K_{max}$. However, other factors are clearly relevant in view of the marked differences in behavior between $R = 0.5$ and 0.7 , e.g., the rapid crack growth at K_{max} levels approaching K_{Ic} due to cleavage fracture of γ -TiAl (as in Fig. 2.7(c)), akin to the high- ΔK behavior controlled by static-mode fracture mechanisms seen in metallic alloys [23].

Crack-Particle Interactions: In contrast to behavior under monotonic loads (Fig. 2.6), crack-path morphologies in TiNb/ γ -TiAl microstructures under cyclic loads reveal that there is minimal ductile-ligament bridging in the crack wake (Fig. 2.15). Crack paths in the plane of loading and crack fronts across the specimen thickness ($\sim 150 \mu m$ behind the crack tip) clearly indicate that the TiNb particles rapidly fail under cyclic loading without any sign of plastic deformation. In the edge (C-R) orientation, fatigue cracks traverse the ductile particles apparently without significant interaction (Fig. 2.15(a)); crack blunting, crack renucleation and resultant in-plane bridging effects, which are so dominant under monotonic loads, are simply not observed. This conclusion was verified by *in situ* telescopic observations on the specimen surface, and also by quantitative estimates of the extent of crack bridging at various ΔK levels. Crack lengths, estimated from elastic-compliance measurements using strain gauges, were within $\pm 200 \mu m$ ($< 2\%$) of those measured using indirect d.c. potential methods, indicating that crack-bridging effects in fatigue are relatively insignificant. No discernable differences in crack paths were noted at the various load ratios.

Although cracking is still continuous through the matrix and ductile phases in the face (C-L) orientation, as shown in Fig. 2.15(b), there is indication of crack branching, deflection, multiple cracking in the matrix and coplanar bridging (associated with a non-planar and discontinuous crack front across the specimen thickness because of overlapping cracks on different planes), consistent with the improved crack-growth resistance in this orientation. Crack renucleation in the matrix ahead of TiNb particles under cyclic loading

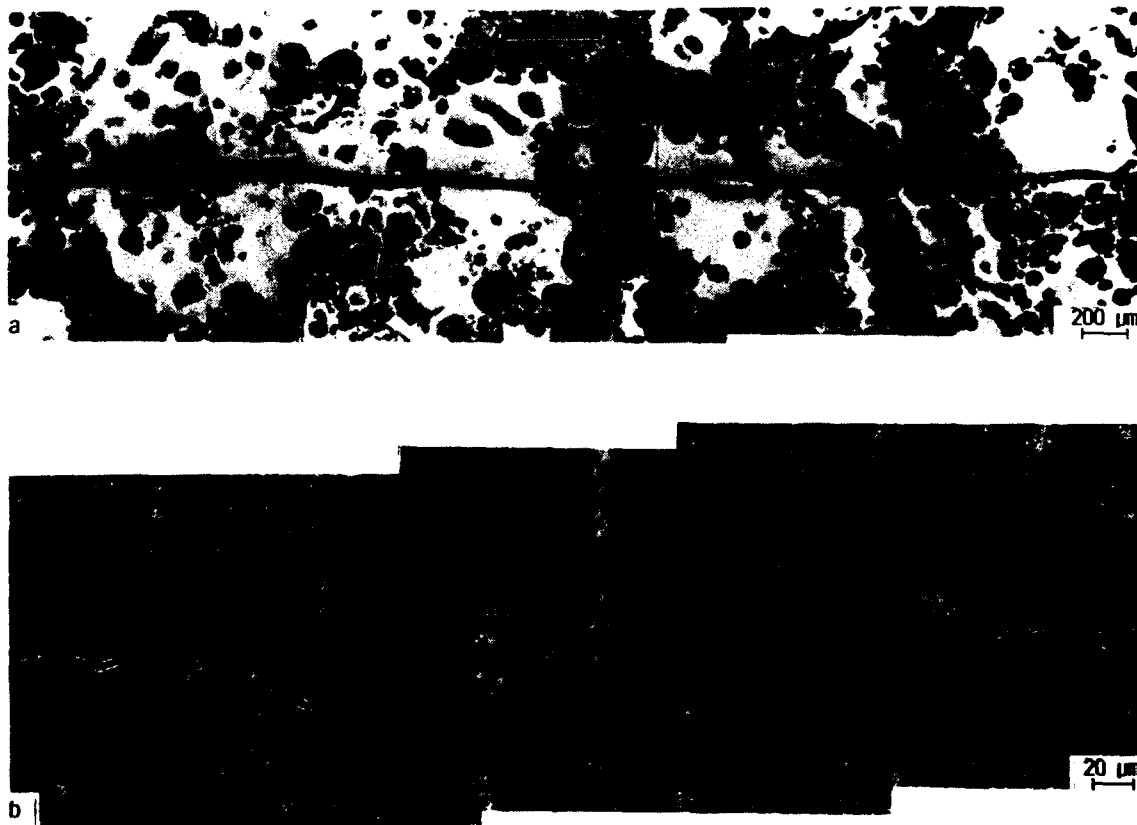


Fig. 2.15: Effect of Nb vs. TiNb ductile reinforcements on the cyclic crack-growth resistance of γ -TiAl in the face (C-L) orientation ($R = 0.1$). Note the superiority of Nb/ γ -TiAl composites due to their relatively weak interfacial bonding compared to TiNb/ γ -TiAl.

is observed at ΔK levels of $\sim 9\text{-}10 \text{ MPa}\sqrt{\text{m}}$; however, due to the rapid fatigue fracture of the TiNb particle, the effective range of crack/particle interactions is limited to a few hundred microns or less (cyclic bridging zone \sim particle thickness); equivalent dimensions under monotonic loading are on the order of several millimeters (Table 2.3). In fact, even in the face orientation, the TiNb particles show minimal evidence of plastic stretching.

Corresponding fracture-surface morphologies are shown in Fig. 2.16. Unlike the microvoid coalescence seen under monotonic loading (Fig. 2.7), the TiNb phase fails by transgranular shear under cyclic loading in both the composite and monolithic form (Fig. 2.16(b)); features resemble fatigue failures in coherent-particle hardened alloys that deform by planar slip [24]. Likewise, the γ -TiAl matrix also shows intrinsic fatigue damage, evidenced by the parallel slip markings in Fig. 2.16(c), in addition to the transgranular and intergranular cleavage modes of failure (Fig. 2.16(c)).

From these observations and other studies [15,16] it may be inferred that the lack of toughening from crack-bridging mechanisms under cyclic loads is the principal reason for subcritical crack-growth effects in TiNb/TiAl composites at ΔK levels well below their crack-initiation toughness values. Such enhanced crack growth results from fatigue-induced failure of the ductile particles before the crack can establish a bridging zone, which is already limited under cyclic loading because of the relatively small crack-opening displacements associated with the lower stress intensities.

The sources for reinforcement-orientation effects on cyclic crack growth are not altogether clear. Potential explanations include: (i) fatigue failure of the reinforcements in the edge orientation in fewer cycles, since the opening along the crack flanks and resultant plastic displacements would be larger than corresponding crack-tip opening displacements in the face orientation; (ii) restriction of crack deflection, branching and coplanar bridging effects in the edge orientation by the reinforcement; and (iii) differences in the phase angle of any local debond cracks.

Reinforcement Size and Volume Fraction Effects: The influence of TiNb reinforcement volume fractions, ranging between 0.05-0.2 ($\sim 40 \text{ }\mu\text{m}$ -thick), on fatigue-crack growth behavior of TiNb/TiAl composites in the edge orientation, is illustrated in Fig. 2.14(a). While fatigue thresholds for all composites fall below the value for monolithic γ -TiAl, there appears to be no consistent effect of f_{TiNb} on the fatigue threshold; ΔK_{TH} values range between $\sim 4.5 \text{ MPa}\sqrt{\text{m}}$ ($f_{\text{TiNb}} \sim 0.05$) and $\sim 5.6 \text{ MPa}\sqrt{\text{m}}$ ($f_{\text{TiNb}} \sim 0.1$).

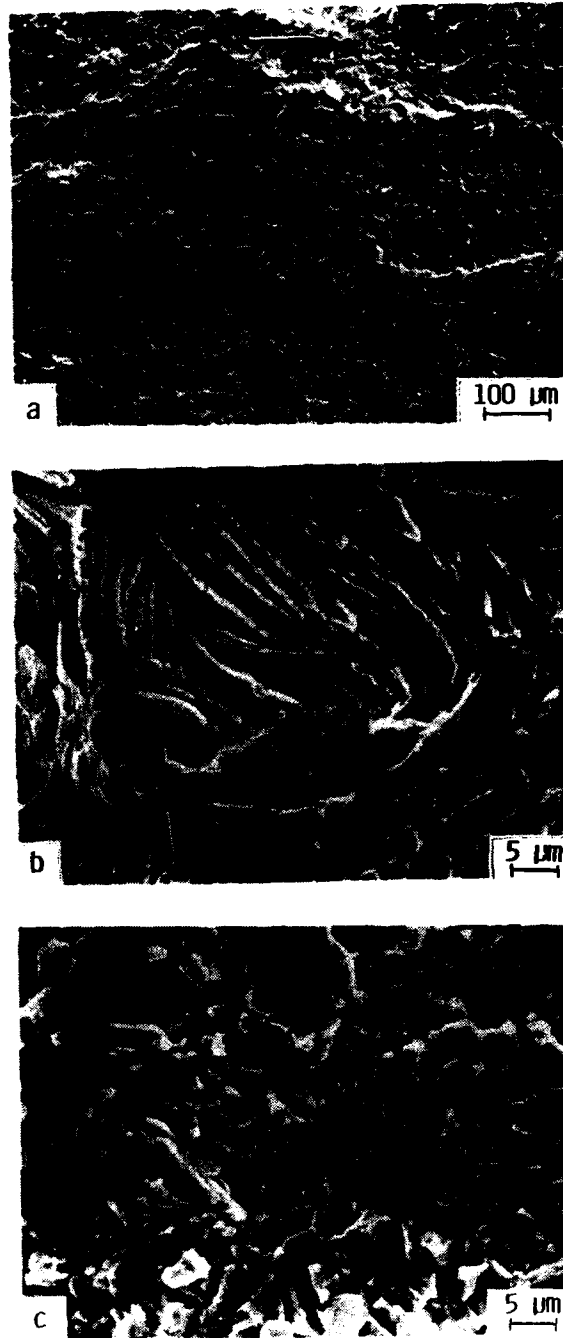


Fig. 2.16: SEM micrographs of crack-path morphologies in TiNb/ γ -TiAl composites under cyclic loading in the (a) edge (C-R) and (b) face (C-L) orientations, taken at specimen mid-thickness location in the loading plane. Horizontal arrow indicates the crack-growth direction.

However, the slope of $da/dN-\Delta K$ curves (measured as the exponent, m) in the intermediate growth-rate region is found consistently to decrease with ductile-phase content (Table 2.4); the ΔK interval for region II and the maximum ΔK marking the onset of region III show a corresponding decrease. In effect, intermediate crack-growth rates in the composites, at a given ΔK , are lowered by increasing the reinforcement volume fraction. More notably, crack-growth rates in the composites with 10 vol.% TiNb, and particularly 5 vol.% TiNb, are significantly *higher* than those found in either unreinforced TiNb or TiAl. These effects could be associated with the competing role of residual stresses or crack-closure effects (which increase ΔK_{tip}) vs. limited crack bridging/trapping (which reduces ΔK_{tip}); with increasing f_{TiNb} , crack bridging/trapping effects may become dominant.

Reinforcement thickness has a minimal effect on cyclic crack-growth behavior in the edge (C-R) orientation, for samples containing 20 vol.% TiNb (Fig. 2.14(b)). However, increasing TiNb particle thickness from ~ 20 to $40\ \mu m$ is found to retard crack advance in the face (C-L) orientation, especially for ΔK levels in the mid-growth rate regime, above $\sim 9\ MPa\sqrt{m}$. Toughening mechanisms associated with crack renucleation in the matrix ahead of the ductile particle, which scale with particle thickness [11,22], are believed to account for the improved fatigue resistance of coarse microstructures. Once again, it is clear that reinforcement-orientation effects are prominent under cyclic loading, with face-oriented composites exhibiting better crack-growth resistance over γ -TiAl and β -TiNb.

TiNb vs. Nb Reinforcements: Figure 2.17 compares the fatigue-crack growth properties of γ -TiAl reinforced with 20 vol.% ($\sim 40\ \mu m$ thick) Nb particles in face (C-L) orientation to corresponding behavior in the TiNb/TiAl, both in the edge and face orientations. While both reinforcements in the face orientation improve the fatigue resistance of γ -TiAl, the cyclic toughening increment is clearly greater for the Nb phase than for TiNb. The fatigue threshold for the Nb/TiAl composite, $\Delta K_{TH} \sim 10\ MPa\sqrt{m}$, is about 75 and 40% larger than the pure γ -TiAl ($\sim 6\ MPa\sqrt{m}$) and the TiNb/TiAl composite ($\sim 8\ MPa\sqrt{m}$), respectively. This is in contrast to fracture toughness behavior under monotonic loading, where the high-strength TiNb reinforcements are significantly more effective in impeding crack advance. When compared at a fixed ΔK of $10\ MPa\sqrt{m}$, growth rates are nearly five orders of magnitude slower in Nb/TiAl than in TiNb/TiAl. However, the enhancement in fatigue resistance of γ -TiAl from Nb additions is far less compared to that equivalent increase in fracture toughness (Fig. 2.9(c)).

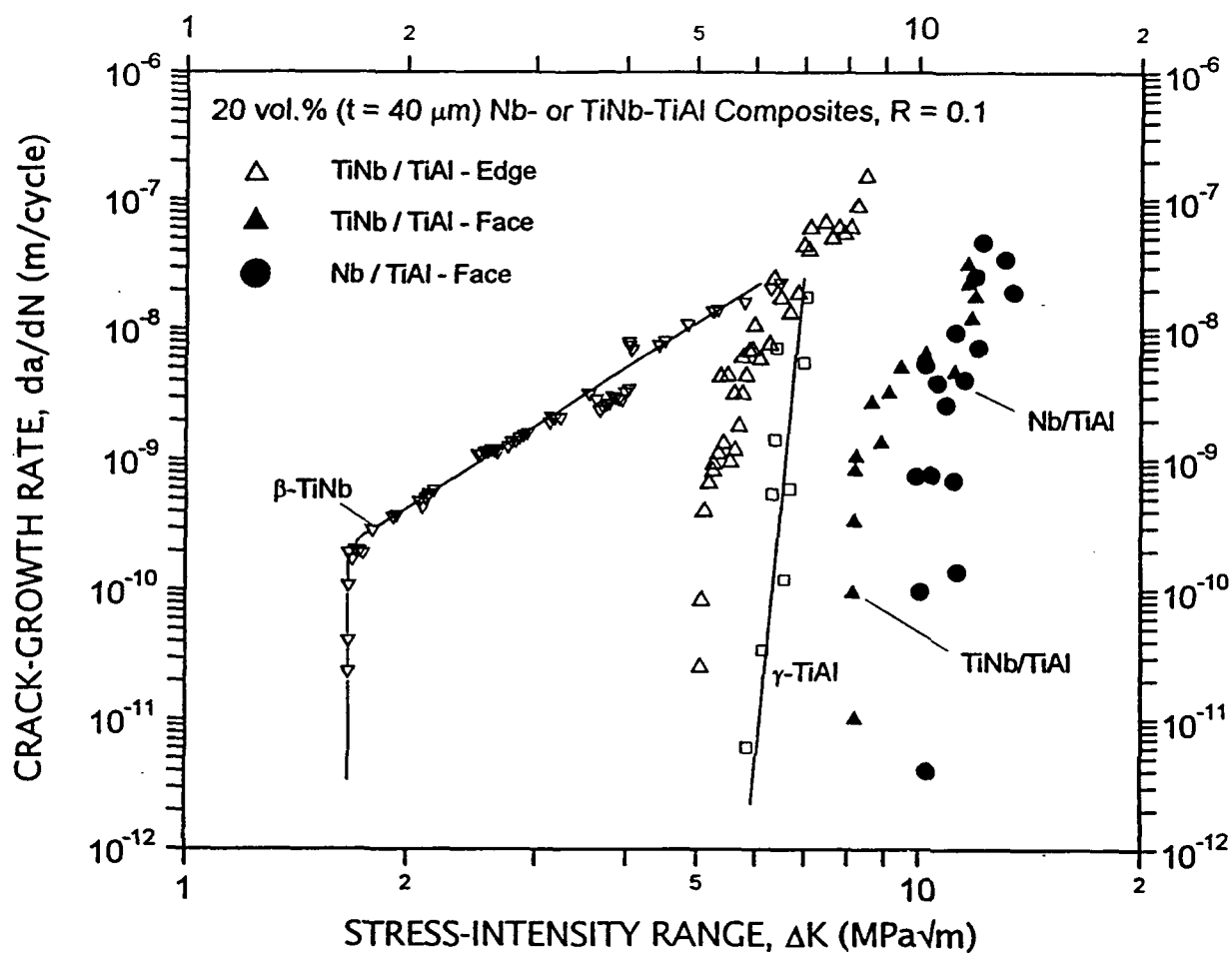


Fig. 2.17: (a-c) SEM images of fracture surfaces in TiNb/ γ -TiAl composites under cyclic loading at various magnification levels. Micrographs (b) and (c) illustrate the cracking morphologies in β -TiNb and γ -TiAl regions of the composite. Horizontal arrow indicates the general direction of crack growth.

Such improved fatigue-crack growth properties using metallic reinforcements can be traced to significant secondary-cracking effects locally near the Nb/TiAl interface. As illustrated in Fig 2.18, these are characterized by (i) crack arrest at the interface, (ii) decohesion along the interface and (iii) crack renucleation in the brittle matrix ahead of the particle, prior to particle failure. Analogous to behavior under monotonic loads, the brittle σ -layer interface surrounding Nb particles is expected to be less fatigue resistant and susceptible to debonding compared to the ductile α_2 layer around TiNb particles. Nevertheless, such Nb-particle debonding relaxes constraint, diffuses plastic strains, and more notably, stops the crack locally and prevents continuous crack penetration into the ductile Nb phase; these mechanisms, in addition to crack renucleation which preserves *local* crack-tip bridging, extend the fatigue life of the Nb reinforcements. However, the extent of debonding during fatigue is still less than that seen under monotonic loading (Fig. 2.10), and is much more evident in Nb/TiAl, under monotonic and cyclic loads, than in TiNb/TiAl composites (Fig. 2.6). As a consequence, fatigue cracks in the matrix of TiNb/TiAl composites advance continuously into the TiNb particle, across the α_2 layer, without significant interactions thereby leading to rapid failure of the TiNb phase. Moreover, the TiNb phase is inherently more susceptible to fatigue failure (due to localized planar-slip deformation) than the strain-hardening Nb phase, consistent with previous results [25]. (Note that fatigue-crack growth rates in Nb are also strongly dependent on interstitial H₂, C, N₂, O₂, and Si impurity contents).

Finally, it is useful to estimate the magnitude of toughening associated with various mechanisms under cyclic loading to provide some insight into their relative contributions. The effects of local crack bridging in fatigue (Fig. 2.18), specifically in the face orientation, on the reduction in near-tip stress intensity, ΔK_b , may be assessed using the Dugdale approximation [26]:

$$\Delta K_b = \frac{2}{\sqrt{\pi}} f \sigma_e \sqrt{2 L_b} \quad (8)$$

where, L_b is the bridging-zone length and σ_e the effective value for uniform bridging tractions in that zone. Taking $L_b \sim 40 \mu\text{m}$ (bridging zone \sim reinforcement thickness) and the average bridging tractions under cyclic loading to be roughly one half the flow stress ($\sigma_e \sim 0.25 [\sigma_o + \sigma_u]$, or ~ 215 and ~ 100 MPa for TiNb and Nb, respectively), the in-plane bridging contributions, ΔK_b , for a composite reinforced with 20 vol.% ductile particles are

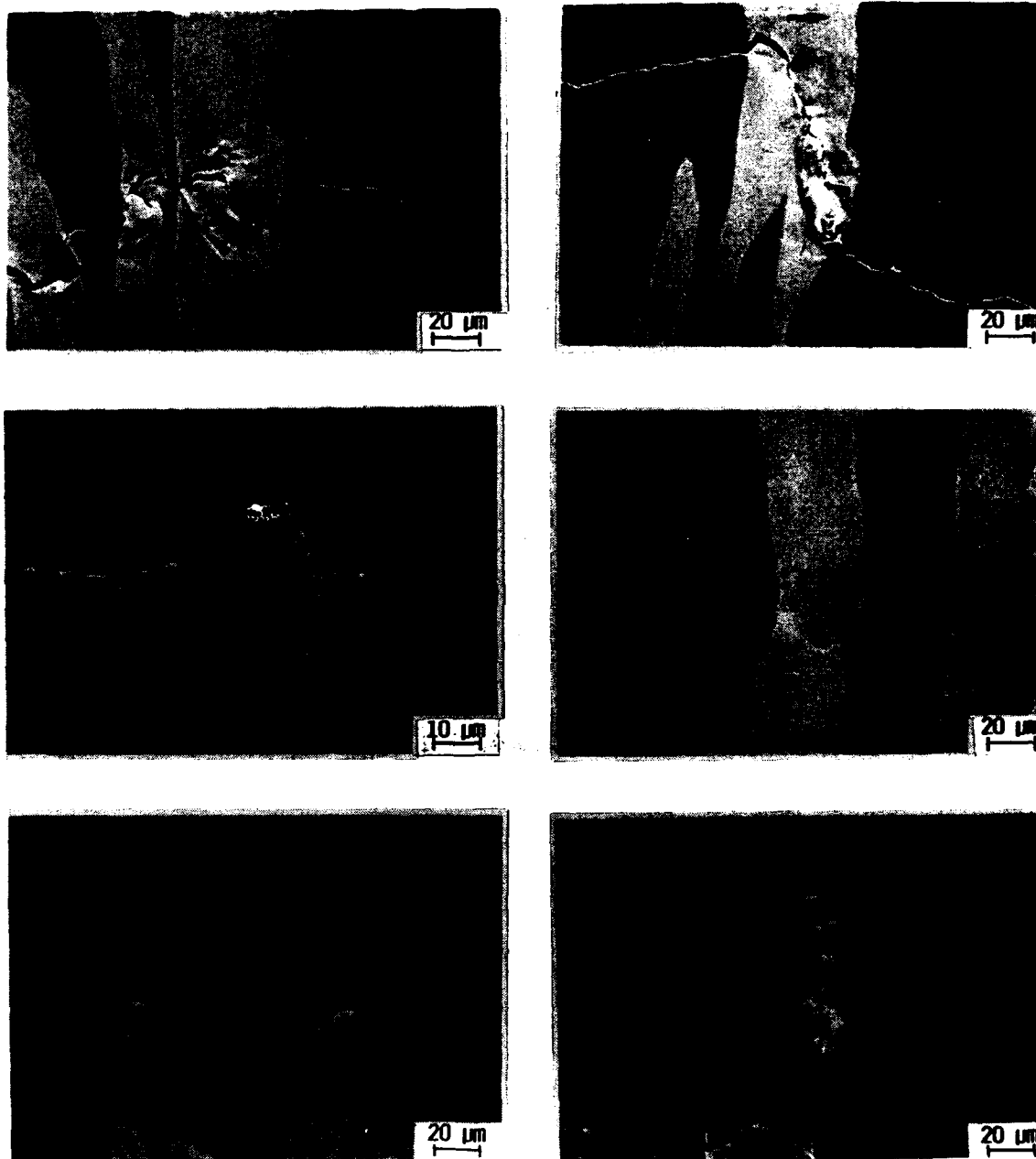


Fig. 2.18: Summary of cyclic crack-path morphologies (in the plane of loading) observed for the Nb/ γ -TiAl composite in the face (C-L) orientation, showing significant interfacial debonding, cracking ahead of the Nb particles and evidence of crack bridging. Horizontal arrow represents the crack-growth direction.

a mere ~ 0.4 and ~ 0.2 $\text{MPa}\sqrt{\text{m}}$ for TiNb and Nb phases, respectively. Measured shifts in the $da/dN-\Delta K$ curves (Fig. 2.17), respectively, are ~ 2 and ~ 4 $\text{MPa}\sqrt{\text{m}}$ for the TiNb/TiAl and Nb/TiAl composites, implying that other mechanisms are relevant. Crack trapping and renucleation of the fatigue crack in the ductile phase associated with blunting (via interfacial decohesion for Nb), and coplanar bridging from multiple and discontinuous crack fronts (for TiNb and Nb) are expected to provide the additional contributions to the fatigue-crack growth resistance.

2.4 Concluding Remarks

The present results extend previous studies [15,16] in illustrating the contrasting role of ductile reinforcements on monotonic (fracture toughness) and cyclic (fatigue) crack-growth resistance of intermetallic-matrix composites. With respect to R-curve toughness, the principal factors are effective reinforcement strength and ductility as mediated by constraint imposed by debonding characteristics of the interface and resultant constrained deformation properties of the reinforcement; local crack/particle interactions contribute to intrinsic crack-initiation toughness. Reinforcement thickness (initiation toughness) and orientation (edge vs. face) effects on toughness, previously seen in coarse-laminated composites, appear to be modest for the pancake-shaped ductile-phase toughened composites, suggesting competing effects of various local crack/particle interactions on monotonic crack-growth resistance.

Very different mechanisms and microstructural factors are associated with fatigue-crack propagation resistance. This is perhaps best illustrated by the degradation in fatigue thresholds compared to γ -TiAl and accelerated crack-growth rates relative to either monolithic constituent in the edge-oriented TiNb/TiAl composites, particularly at low volume fractions. The premature cracking or low-cycle fatigue failure of ductile particles at small crack-opening displacements under cyclic loading result in very limited bridging zones and therefore minimal toughening. Improved fatigue resistance is seen only in the face-oriented composites, the increase being attributed to local crack-particle interaction mechanisms that are similar to those under monotonic loading yet are far less potent under cyclic loading. The fatigue resistance of the composites is further enhanced by weak (debonding) particle-matrix interfaces and ductile particles with optimal fatigue properties, e.g., strain-hardening phases with high modulus and strength. Debonding can be induced at inherently strong reaction-layer interfaces by applying thin oxide coatings between constituents, although this can reduce the toughness. These observations suggest that ductile phases are associated with multiple and competing mechanisms, with the net effect

under fatigue loading being sensitive to reinforcement architecture, volume fraction and particle thickness.

Such different, and in some cases contradictory, requirements for superior toughness and fatigue resistance suggest that optimized composite microstructures may require a variety of reinforcements and architectures based on alternative shielding mechanisms. For example, a semi-continuous network of the ductile phase offering a preferred crack path may provide improved fatigue resistance by promoting crack meandering. This in turn promotes crack-tip shielding from roughness-induced crack closure from the wedging of enlarged fracture-surface asperities, and has proved to be very effective in improving the fatigue-crack growth resistance of duplex ferritic/martensitic steels and α/β titanium alloys [27,28]. Such an approach should also provide adequate toughening under monotonic loading due to the formation of extensive bridging zones.

2.5 Conclusions

Based on an experimental study of the monotonic and cyclic crack-growth properties of ductile-phase toughened γ -TiAl intermetallic composites, reinforced with either β -TiNb or Nb, the following conclusions can be made:

1. Brittle γ -TiAl intermetallic alloys can be significantly toughened under monotonic loading by dispersing ductile Nb or TiNb reinforcements; compared to a K_{Ic} value of $8 \text{ MPa}\sqrt{\text{m}}$ for pure γ -TiAl, both type of composites show increased crack-initiation toughness (K_{Ii}) and marked resistance-curve behavior with $K_{Ii}(\Delta a)$ values in excess of $\sim 40 \text{ MPa}\sqrt{\text{m}}$. Under monotonic loading, the stronger β -TiNb particles promote greater toughening than Nb reinforcements.

2. Improvement in crack-growth toughness (as reflected by the slope of the resistance curve, dK_{Ic}/da) under monotonic loading is primarily attributed to shielding effects, associated with extensive bridging by intact TiNb or Nb ligaments, over dimensions of several millimeters, in the crack wake. A number of local crack-particle interactions additionally produce increased crack-initiation toughness, and provide secondary contributions to the slope of the R-curve. Depending on the measure, toughness increases with thickness (K_{Ii}) and volume fraction (K_{Ii} , dK_{Ic}/da) of the ductile-phase particles; however, reinforcement orientation appears to have a relatively minor effect.

3. Ductile TiNb and Nb reinforcements also lead to enhanced cyclic fatigue-crack growth resistance of γ -TiAl, although the effect is specific *only* to the face (C-L) orientation and is seen as a modest increase in the fatigue threshold, ΔK_{TH} . The increase appears to be associated with local crack-particle interaction mechanisms, including crack renucleation (in the matrix and/or particle), crack branching, limited interface debonding and discontinuous (out-of-plane) crack bridging.

4. Conversely in the edge (C-R) orientation, TiNb particles actually *degrade* the ΔK_{TH} relative to γ -TiAl, and at low volume fractions accelerate the intermediate crack-growth rates relative to *either* monolithic constituents. Behavior is primarily due to the premature fatigue fracture of ductile phases under cyclic loads, which severely limits bridging in the crack wake, and the absence of any other microstructural interactions.

5. In contrast to their effect on toughness under monotonic loads, in the face (C-L) orientation, Nb particles yield better fatigue-crack growth resistance compared to TiNb particles. This results from extensive debonding of the Nb particles from the γ -TiAl matrix, due to the weak interface, and their inherently better fatigue properties compared to TiNb reinforcements.

2.6 References

1. C. T. Liu, J. O. Stiegler and F. H. Froes, *Metals Handbook* 2, 913 (1991).
2. R. L. Fleischer, D. M. Dimiduk and H. A. Lipsitt, *Ann. Rev. Mater. Sci.* 19, 231 (1989).
3. Y. W. Kim, *Acta Metall. Mater.* 40, 1121 (1992).
4. Y. W. Kim and D. M. Dimiduk, *J. Metals* 43:8, 40 (1991).
5. K. S. Chan and Y. W. Kim, *Metall. Trans. A* 23A, 1663 (1992).
6. K. S. Chan: *J. Metals*, 44:5, 30 (1992).
7. H. E. Dève, A. G. Evans and D. S. Shih, *Acta Metall. Mater.* 40, 1259 (1992).
8. C. K. Elliott, G. R. Odette, G. E. Lucas and J. W. Sheckherd, in *High-Temperature/High-Performance Composites*, (edited by F. D. Lemkey, A. G. Evans, S. G. Fishman and J. R. Strife), MRS Symp. Proc., Vol. 120, p. 95, Materials Research Society, Pittsburgh, PA, 1988.

9. H. E. Dève, A. G. Evans, G. R. Odette, R. Mehrabian, M. L. Emiliani and R. J. Hecht, *Acta Metall. Mater.* **38**, 1491 (1990).
10. G. R. Odette, H. E. Dève, C. K. Elliott, A. Harigowa and G. E. Lucas, in *Interfaces in Ceramic Metal Interfaces*, (edited by R. Y. Lin, R. J. Arsenault, G. P. Martins and S. G. Fishman), p. 443, TMS-AIME, Warrendale, PA, 1990.
11. G. R. Odette, B. L. Chao, J. W. Sheckherd and G. E. Lucas, *Acta Metall. Mater.* **40**, 2381 (1992).
12. V. D. Krstic, P. S. Nicholson and R. G. Hoagland, *J. Am. Ceram. Soc.* **64**, 499 (1981).
13. M. F. Ashby, F. J. Blunt and M. Bannister, *Acta Metall.* **37**, 1847 (1989).
14. B. D. Flinn, M. Rühle and A. G. Evans: *Acta Metall.* **37**, 3001 (1989).
15. K. T. Venkateswara Rao, G. R. Odette and R. O. Ritchie, *Acta Metall. Mater.* **40**, 353 (1992).
16. K. T. Venkateswara Rao and R. O. Ritchie, in *Intermetallic Matrix Composites II*, (edited by D. Miracle, J. Graves and D. Anton), MRS Symp. Proc., Vol. 273, p. 127, Materials Research Society, Pittsburgh, PA, 1992.
17. Anon, American Society for Testing and Materials Standard E399-90 **3.01**, 506 (1992).
18. R. O. Ritchie and R. H. Dauskardt, *J. Ceram. Soc. Japan* **99**, 1047 (1991).
19. R. H. Dauskardt and R. O. Ritchie, *Closed Loop* **27**, 7 (1989).
20. Anon, American Society for Testing and Materials Standard E647-91 **3.01**, 674 (1992).
21. R. O. Ritchie, W. Yu and R. J. Bucci, *Eng. Fract. Mech.* **32**, 361 (1989).
22. M. Y. He, F. E. Heredia, D. J. Wissuchek, M. C. Shaw and A. G. Evans, *Acta Metall. Mater.* **41**, 1223 (1993).
23. R. O. Ritchie, *Int. Met. Rev.* **20**, 205 (1979).
24. K. T. Venkateswara Rao and R. O. Ritchie, *Int. Mater. Rev.* **37**, 153 (1992).
25. S. Fariabi, A. L. W. Collins and K. Salama, *Metall. Trans. A* **14A**, 701 (1983).

26. H. Tada, P. C. Paris and G. R. Irwin, *The Stress Analysis of Cracks Handbook*, Paris Prod. Inc./Del Corp., St. Louis, MO (1985).
27. J.-K. Shang, J. L. Tzou and R. O. Ritchie, *Metall. Trans. A* **18A**, 1613 (1987).
28. J. M. Larsen, T. Nicholas, A. W. Thompson and J. C. Williams, in *Small Fatigue Cracks* (edited by R. O. Ritchie and J. Lankford), pp. 499-512, TMS-AIME, Warrendale, PA, 1986.

3. PROCESSING OF DUCTILE-PHASE TOUGHENED Nb/Nb₃Al IN SITU COMPOSITES

(In collaboration with Dr. L. C. DeJonghe)

3.1 Introduction

Niobium has been the subject of renewed research interest since the mid-1980's as the materials community continues to seek new high-performance materials and alloys for advanced high-temperature applications in aerospace propulsion systems [1]. This is especially true for structural applications with service temperatures above 1100-1150°C, which represents the upper-bound application range of both single-crystal and oxide-dispersion strengthened nickel-base superalloys. Current gas-turbine engines in commercial use primarily utilize nickel-base superalloys in the hot turbine and compressor sections and primarily nickel-base and titanium alloys in the cooler compressor sections. However, since the efficiency and total thrust of a jet engine is a direct function of the peak temperature of the working fluid and current limits are set by thermal constraints on materials, these alloys are unlikely to meet the performance needs of the next generation of engines, which will require markedly stiffer materials operating at high stress levels at very much higher temperatures. At present, materials are being sought which can operate at temperatures as high as 1650°C, although materials which can operate effectively at 1000°C would represent significant progress. Prime candidates include ordered intermetallics, ceramics and composites based on metal, intermetallic, ceramic or carbon matrices, all materials which can suffer from potential problems of very low ductility and fracture toughness.

Niobium metal of sufficient purity is tough and ductile and exhibits a unique combination of mechanical and physical properties. It is the lightest of the refractory metals, having a density close to that of copper, and has good thermal conductivity for heat transfer applications. Above 1000°C, however, although it retains a useful degree of strength, it oxidizes very rapidly, such that in the pure or unprotected form it is inappropriate for use in oxygen-bearing environments at these temperatures. Specific alloying additions, such as aluminum, can effectively improve the oxidation resistance; in fact, one such alloy, the intermetallic compound Nb₃Al, shows sufficiently good elevated-temperature properties that it is considered as a very promising candidate for potential high-temperature structural use [2,3].

Most intermetallic compounds, however, are particularly prone to brittle fracture because of a limited number of easy slip systems, a large slip vector, restricted cross-slip

and difficulty of transmitting slip across grain boundaries. These properties are the result of their complex crystal structures from which they derive their strength [4,5]. Nb_3Al , for example, possesses the A-15 structure, with a melting temperature of 2060°C and a density of 7.29 g/cm^3 . Accordingly, it shows extremely low ductility and fracture toughness at room temperature, which inhibits its fabrication and use at low temperatures.

One way of improving the toughness of a brittle intermetallic such as Nb_3Al is to fabricate a composite through incorporation of a ductile phase to induce ductile-phase toughening; this primarily acts to impede crack advance by ductile-ligament bridging [6]. This may be accomplished either by artificially hybridizing the microstructure through powder-metallurgy techniques or through *in situ* precipitation reactions based on phase transformations in the alloy system. In the case of the binary Nb-Al system, the peritectic reaction at 2060°C (Fig. 3.1), involving the precipitation of Nb_3Al from the liquid and high-temperature Nb solid solution (Nb_{ss}), can be utilized for fabricating two-phase microstructures of Nb_{ss} in a brittle Nb_3Al matrix. Previous studies have shown this to be a sluggish transformation, such that the Nb solid solution can be retained down to room temperature with only a moderate degree of undercooling [8-10]; further heat-treatment then leads to the precipitation of the ordered second phase. The precipitation reaction is a massive transformation, resulting in a highly uniform, fine distribution of a filamentary niobium within a non-contiguous Nb_3Al matrix. Such a duplex Nb/ Nb_3Al microstructure can potentially enhance toughness primarily through crack bridging by the ductile Nb phase, with an additional contribution from deformation within the ductile phase.

3.2 Crystal Structure and Formation of A-15 Intermetallics

As shown in Figure 3.2, the A-15 cubic structure with A_3B stoichiometry consists of orthogonal chains of "A" (Nb) atoms along $\langle 100 \rangle$ directions crisscrossing the bcc arrangement of "B" (Al) atoms. A-15 is the simplest of the tcp (tetragonal close-packed) structures and, though not obvious, the chains of "A" atoms penetrate normal through planar hexagonal nets of atoms rotated alternately by 90° [11]. The short distance between the "A" (Nb) atoms along the chain suggests strong directional bonding but the stacking of hexagonal nets suggests packing considerations may be a dominating factor. An important consequence of the TCP structure is the absence of large octahedral interstices [12]. In a high temperature environment, this may lead to lower solubility for interstitial elements such as carbon, nitrogen and oxygen, compared with that in the bcc structure of refractory metals.

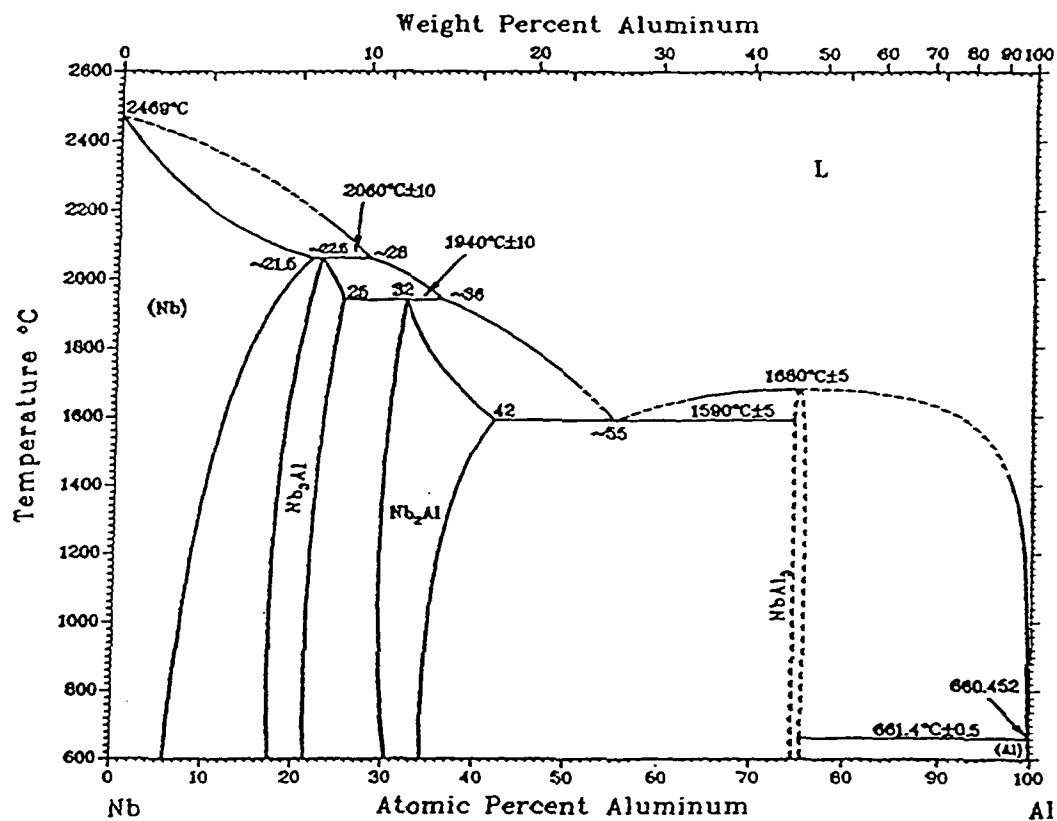


Fig. 3.1. The Nb-Al binary phase diagram.

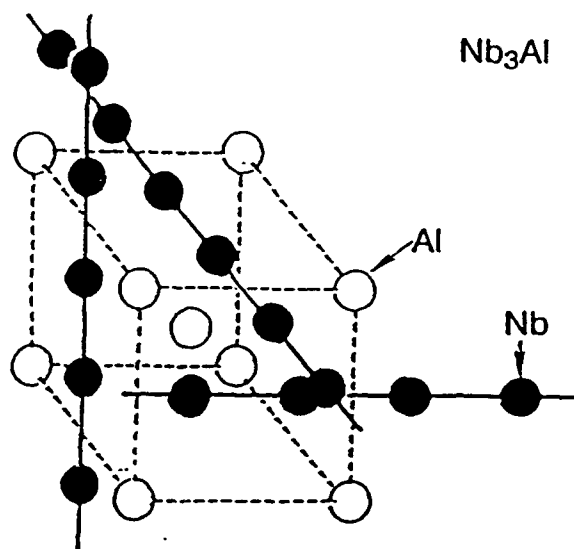


Fig. 3.2. The A-15 crystal structure with A_3B stoichiometry showing orthogonal chains of "A" atoms criss-crossing the bcc arrangement of "B" atoms.

The phase formation map [13] reproduced in Figure 3.3 shows A-15 compounds to be primarily formed based on the vanadium and chromium groups of transition elements with (1) semi-precious and precious transition elements, and with (2) non-transition elements of the aluminum and silicon groups. As seen in Figure 3.3, the nature of phase formation of these two sets of A-15 compounds is distinctly different. Most of the compounds containing semi-precious elements, marked by region "A", form by peritectoid reaction. On the other extreme, most of the compounds containing non-transition elements, covered by region "C", form by a peritectic reaction. The A-15 compounds in the transition region, "B", mostly form congruently either from the liquid or solid. The one instance of solid state phase transformation marked as "syntactic" in Fig. 3.3 refers to the existence of a A-15 δ -Cr-Ni phase at 100% Cr [14]. Among the binary systems of some practical applicability, examples of Re-V, Nb-Al, V-Ga and Cr-Si may be cited as forming an A-15 compound by peritectoid, peritectic, congruent from solid and congruently from liquid transformations respectively.

The Nb-Al system is of direct interest in this study and the portion of the phase diagram covering the A-15 field is shown in Figure 3.1. As shown, Nb₃Al is formed by a peritectic reaction, with uniquely sloping phase boundaries such that the Nb-Al solid solution overlaps the intermetallic at high temperatures. This aspect of the phase formation along with other considerations was important in selecting Nb₃Al for further study. It is felt that understanding the fundamental nature of the ordered phase formation is important, since it intrinsically controls the extent of ordering as well as the formation of useful two phase microstructures which may significantly impact the mechanical behavior.

3.3 Experimental Procedure

Preparation and Synthesis and Powders

Commercially pure Nb powder (1-10 μ m in size) was obtained from M/s Cerac, Inc., Milwaukee, WI; atomized Al powder (\sim 3 μ m) was obtained from M/s Valimet, Inc., Stockton, CA. The powders were mixed in the ratio of Nb-6 wt.% Al (Nb-18 at.% Al), prior to ball milling for 20 min. The mixed powders were then synthesized by heating *in vacuo* to 1400°C at a rate of 20°C/min, held at this temperature for an hour, and stored under argon to prevent oxidation; the sequence was repeated to ensure complete synthesis of Nb₃Al from the elemental Nb and Al powders.

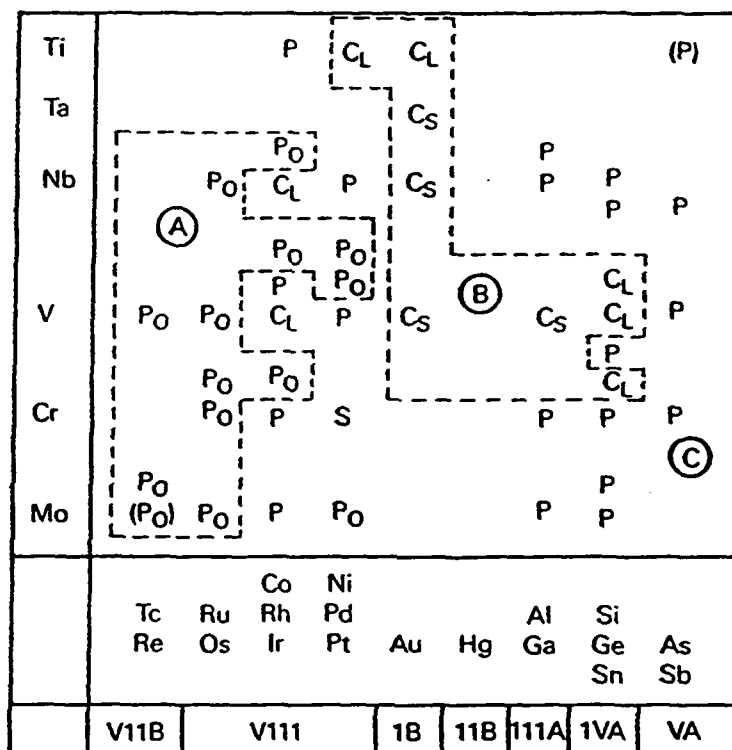


Fig. 3.3. Phase formation map for A-15 intermetallics reproduced from ref. 13, where: P_O, peritectoid; P, peritectic; C_L, congruent from melt; C_S, congruent from solid; and S, syntactic; describes the nature of A-15 phase formation.

Hot Pressing

Hot pressing was performed using a graphite die (38-mm-dia) to hold the synthesized powders. Several samples were fabricated in a single operation by separating the powders by graphite spacers, coated with a boron nitride lubricant to prevent welding between graphite and the Nb-Al powder. The compacted powders were hot pressed by simultaneously increasing the pressure and temperature to 36 MPa and 1650°C, respectively, holding for 10 min, and cooling to room temperature. The resulting samples obtained were in the form of discs, ~38 mm in diameter and ~2.5 mm thick, from hot pressing ~25 g of synthesized powder.

Thermal Treatment for Lamellar Microstructure

To examine the nature of phase transformations and sequence of microstructural development, the hot-pressed samples were heat treated in an inert environment at 1800°C for 1, 4, and 24 hours, and then cooled fairly rapidly (15°C/min) down to room temperature. Samples were subsequently annealed at 1450°C for 24 h to reduce internal stresses and consolidate the microstructure.

An alternate (and more reproducible) technique of preparing a lamellar microstructure was to arc-melt rods of Nb and Al in the ratio of Nb-7 wt.% Al (Nb-20 wt.% Al) and subsequently anneal at 1450°C for 24 h. This resulting microstructure is more uniform and the Nb lamellae can be coarsened to an extent.

Pure Nb₃Al Sample Preparation

Pure (monolithic) Nb₃Al was prepared by mixing and arc-melting Nb and Al rods in the ratio Nb-9 wt.% Al (Nb-25 wt.% Al); volatilization resulted in samples of composition Nb-7 wt.% Al. These samples, which contained cracks from the rapid cooling in the water-cooled hearth of the furnace, were subsequently ball milled for 2 h to a fine Nb₃Al powder, before hot pressing at 1500°C for 15 min at a pressure of 36 MPa. Final samples were obtained in the form of discs, 38 mm in diameter and ~2.5 mm thick.

3.4 Results and Discussion

Equiaxed Nb/Nb₃Al Microstructure

The equiaxed Nb/Nb₃Al microstructure obtained on hot pressing the synthesized Nb-6 wt.% Al powders at 1650°C is shown in Figure 3.4, along with the corresponding X-ray diffraction pattern. Consistent with the Nb-Al phase diagram (Fig. 3.1), a dual-phase microstructure of niobium solid solution and elemental niobium (~40 vol. %) dispersed as the second phase within a Nb₃Al matrix is obtained. A small amount of elemental Al and Nb was present due to incomplete synthesis of the Nb and Al powders.

Lamellar Nb/Nb₃Al Microstructure

Arc-melting of the Nb-7 wt.% Al rods resulted in dendrites of Nb solid solution at room temperature (Fig. 3.5a); subsequent heat-treatment at 1450°C for 24 h resulted in the precipitation of the ordered Nb₃Al phase in the form of a uniform and fine distribution of a filamentary niobium within a non-contiguous Nb₃Al matrix (Fig. 3.5b). The retention of the Nb solid solution at room temperature can be explained using Figure 3.1. Consider the solidification of the alloy Nb-5 wt.% Al (after volatilization of ~2 wt.% Al during arc-melting). As the temperature decreases, the first phase to appear is the Nb solid solution with the composition Nb-5 at. % Al, at a temperature close to ~2300°C. The Nb solid solution grows dendritically with successive layers solidifying at compositions determined by the local temperature and the Nb_{ss} solidus. If diffusion in the dendrites is slow (due to rapid cooling in the water-cooled copper hearth), the liquid will eventually reach the composition Nb-28 at.% Al and on further cooling it reacts with the Nb solid solution to produce a layer of Nb₃Al. However, the Nb_{ss} dendrites are effectively isolated from further reaction and are thus retained at lower temperatures. Meanwhile, the Nb₃Al phase continues to precipitate from the liquid at compositions from 22.5 to 25 at.% Al. Again, if there is no diffusion in the solid, the liquid can reach a composition of Nb-36 at.% Al and can solidify as Nb₂Al. Thus a small amount of Nb₂Al can be present along with mostly Nb₃Al surrounding the Nb_{ss} dendrites. Figure 3.5a shows the microstructure obtained on arc-melting and shows the dendrites of Nb_{ss}. The preferential etching observed maybe due to the presence of Nb₃Al and some Nb₂Al phases trapped between the dendrites. The existence of a eutectic in the phase diagram at ~55 at.% Al suggests that a small amount of NbAl₃ is also likely to exist with the Nb₃Al and Nb₂Al.

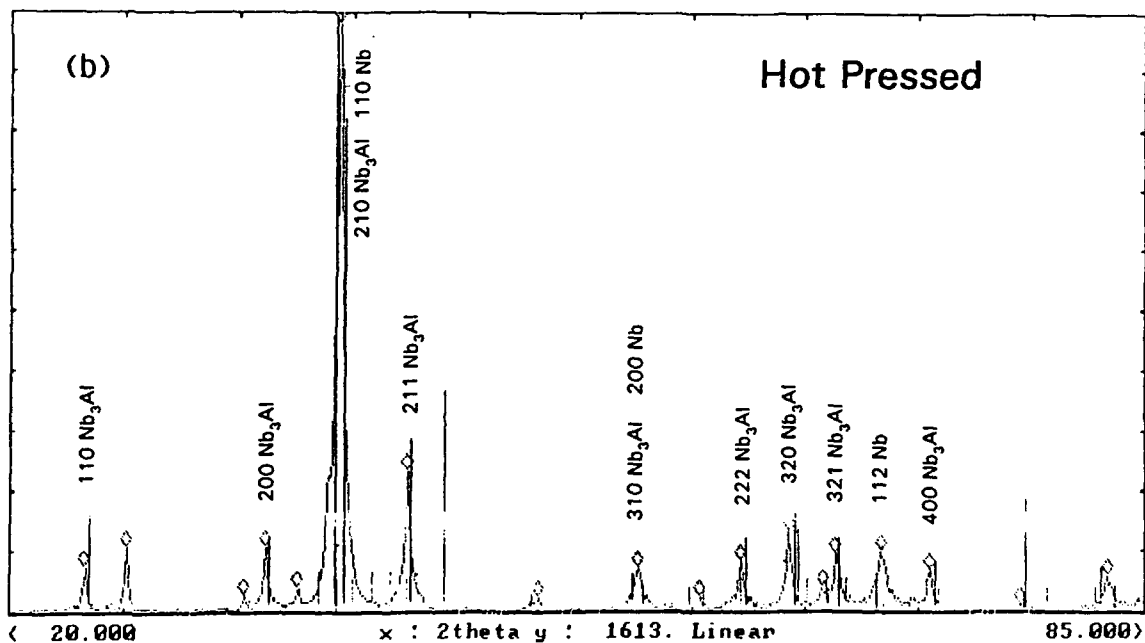
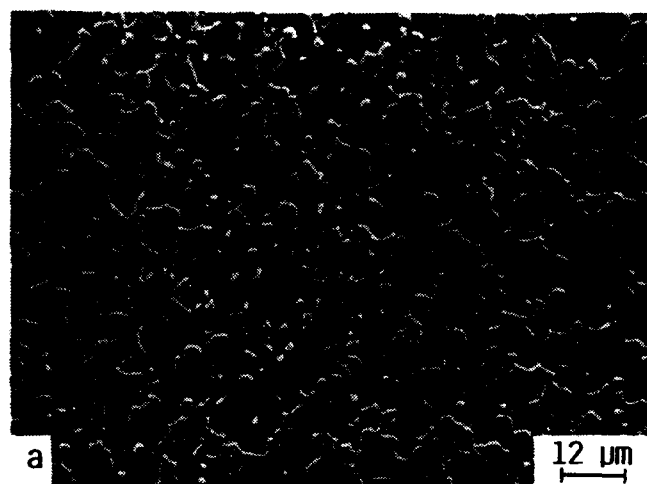


Fig. 3.4. Microstructural features of the hot-pressed (equiaxed) Nb-6 wt.% Al sample showing (a) scanning electron micrograph of Nb₃Al matrix with equiaxed islands of Nb, and (b) corresponding X-ray diffraction pattern showing characteristic peaks of Nb₃Al and Nb.

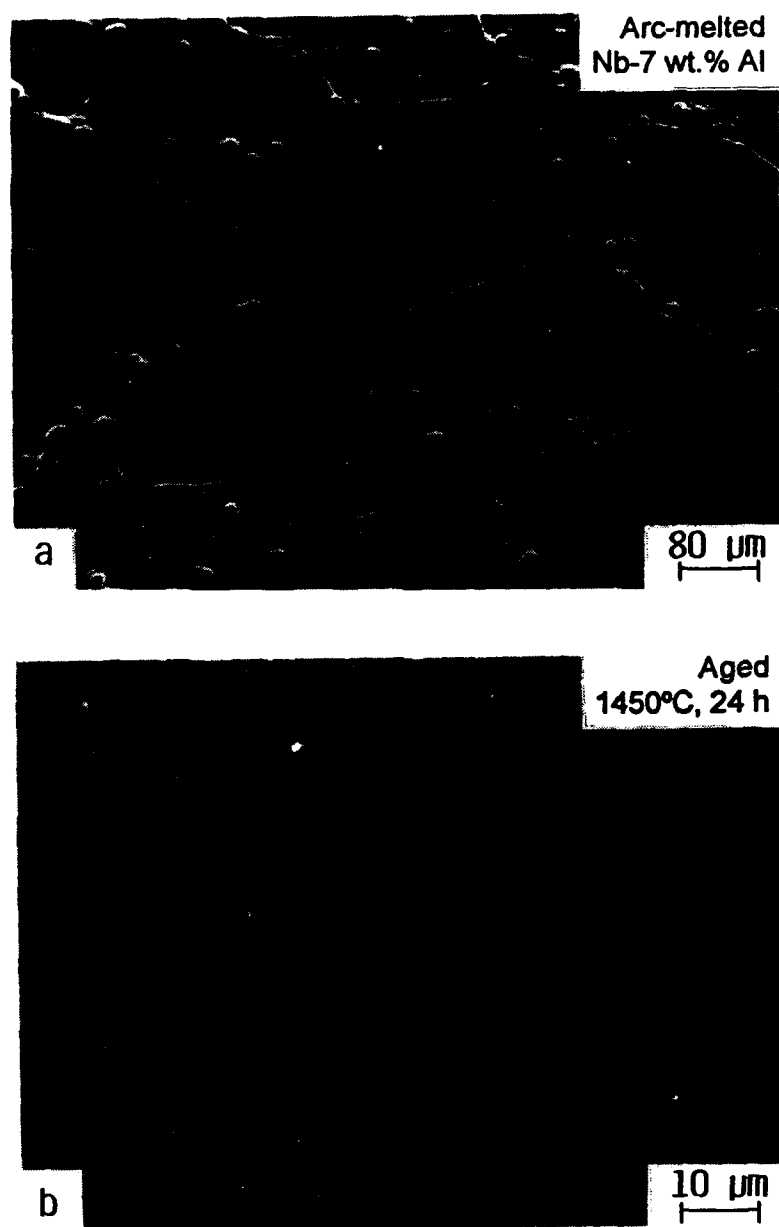


Fig. 3.5. Scanning electron micrographs of microstructural features of the (a) arc melted Nb-7 wt.% Al sample, showing the existence of the retained Nb_{ss} solid solution with no second phase, and (b) after aging at 1400°C for 24 h showing the lamellar Nb_{ss}/Nb₃Al solid solution microstructure.

Similar processes are involved in the development of the microstructure on aging the hot-pressed microstructure at 1800°C for 24 h. On aging the hot-pressed microstructure at 1800°C for 24 h there is sufficient time for diffusion to occur. The nucleation of the Nb₃Al colonies occurs heterogeneously at the grain boundaries; the start of such Nb₃Al nucleation due to a partial massive transformation is shown in Figure 3.6. Subsequent development and growth of the lamellar Nb₃Al phase is imaged using transmission electron microscopy (TEM) in Figure 3.7; corresponding trace analysis from selected area diffraction patterns indicate that the growth of the Nb₃Al colonies occurs in the $\langle 110 \rangle$ Nb_{ss} and $\langle 211 \rangle$ Nb₃Al direction. As seen from Figure 3.7c, the growth progresses to the point where the lamellae fuse into small, elongated grains with a 5-8° misorientation between them; the grains themselves exhibit abundant bend contours. There is also a high density of dislocations within the Nb solid solution near the transformation zone, as shown by the high-magnification TEM micrograph in Figure 3.8 of highly dislocated niobium solid solution adjacent to plates of ordered Nb₃Al phase. The configuration and proximity of the dislocations suggests that they are associated with a highly strained matrix of Nb solid solution. Previous work [15,16] on A-15 compounds has shown that since the A-15 phase (Nb₃Al) has a substantial mismatch with the parent Nb solid solution, the initial precipitates are likely to be under a relatively high state of strain. Alternatively, compressive and tensile strains may likely be set up in the phases due to some lattice movement associated with the different diffusivities of the Nb and Al. The internal state of strain may be relieved to an extent by preferential nucleation along grain boundaries and along defects in the matrix such as dislocations. The initial nucleus is a small elongated rod-like particle of the ordered Nb₃Al phase which grows (by removing Al atoms from the bcc phase on either side) into a deformed and supersaturated bcc solid solution (Nb_{ss}). Due to the depletion of Al atoms surrounding the Nb₃Al phase, the subsequent Nb₃Al precipitate nucleates on the top of, or in parallel to, the existing one, accounting for the lamellar growth of the Nb₃Al colonies along specific directions shown in Figs. 3.6 and 3.7.

Hong and Morris [16] have shown that the initial A-15 precipitates from the supersaturated parent matrix can differ from the equilibrium A-15 phase in terms of composition and internal strain. There are thermodynamic reasons [17] to anticipate that the severe supersaturation present at the time the particles form may cause them to have a more nearly stoichiometric composition than the equilibrium phase diagram would suggest. The energetic barrier to the formation of a small particle of a new phase within a

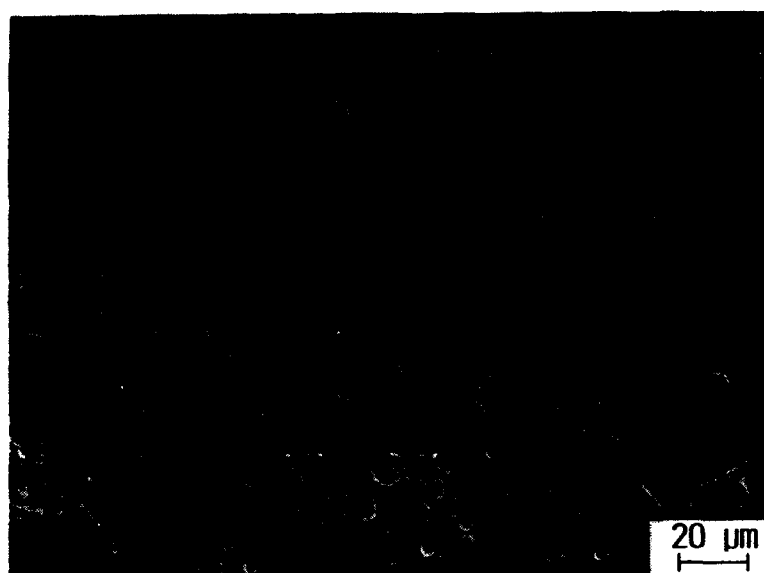


Fig. 3.6. Scanning electron micrograph showing the start of the nucleation of Nb₃Al at grain boundaries with the Nb_{ss} solid solution as the matrix.



Fig. 3.7. (a) High and (b) low-magnification bright-field transmission electron micrographs of the growth of Nb₃Al colonies from grain boundaries with growth direction of $\langle 110 \rangle$ Nb_{ss} and $\langle 211 \rangle$ Nb₃Al direction during early stages of the peritectic transformation, and (c) in the fully-transformed condition. Note the trapped Nb_{ss} between Nb₃Al lamellae in (c).

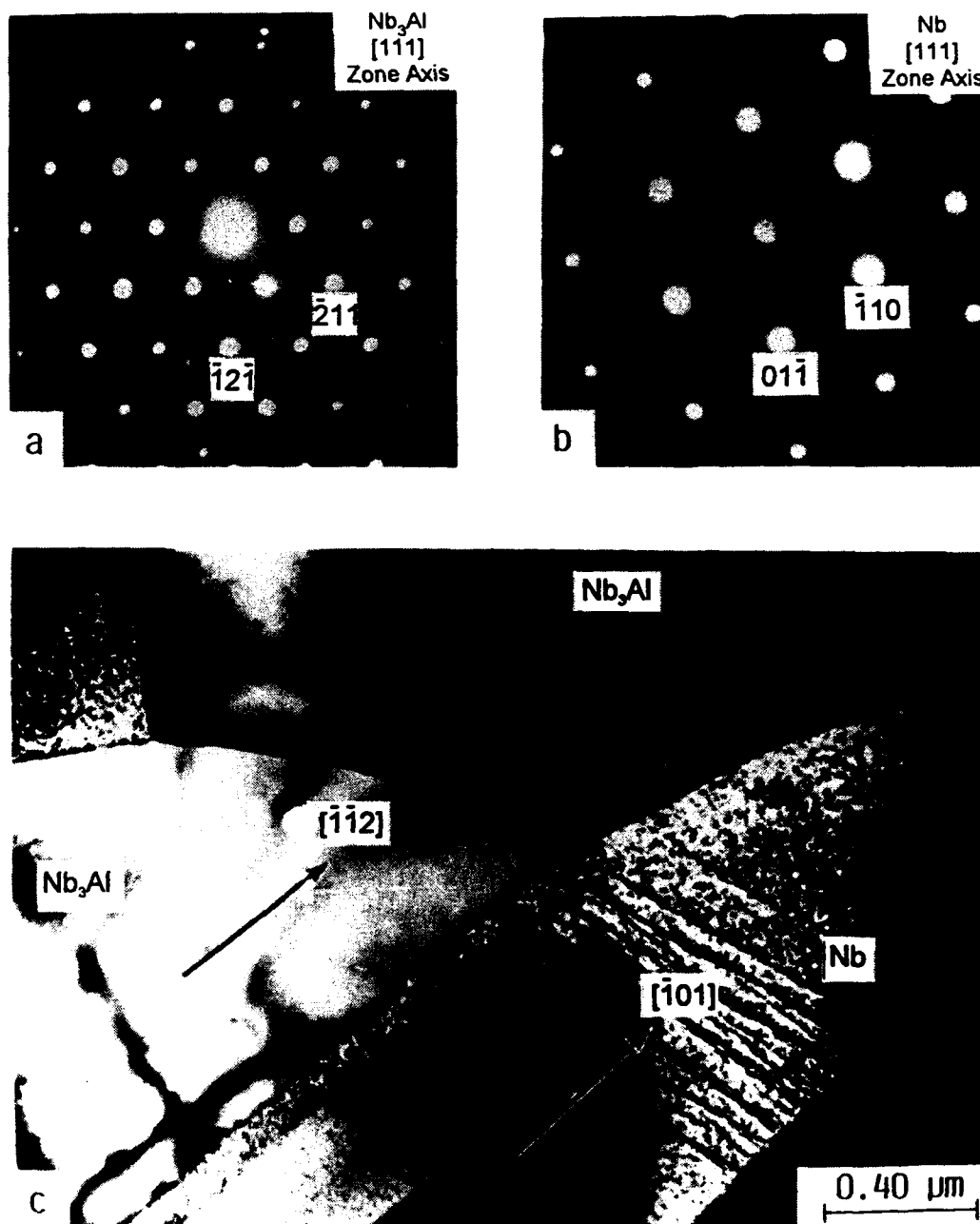


Fig. 3.8. Selected area diffraction patterns in the (a) Nb_3Al and (b) Nb phases with $\langle 111 \rangle$ zone axis and (c) high-magnification bright-field transmission electron micrograph of the highly dislocated Nb_{ss} solid solution adjacent to plates of ordered Nb_3Al . Note the dislocation pile-ups at incoherent Nb_3Al boundaries.

supersaturated matrix is minimized when the new phase forms in a state such that the chemical potential of each component remains constant. If both the parent (Nb_{ss}) and product (Nb_3Al) phases are incompressible, then the relevant chemical potential is the relative chemical potential, which is given by the slope of the free energy vs. composition curve of the parent solution measured at its mean composition (Fig. 3.9). The most favorable composition of the initial precipitate phase is that composition at which its free energy vs. composition curve, at the same temperature, has an equal slope. This implies that the initial precipitate particles formed under significant supersaturation will be richer in solute than indicated by the equilibrium phase diagram (Fig. 3.9). As noted above, the internal strain in the precipitate particles may be relieved by preferential nucleation along defects (e.g., dislocations) in the matrix and may be further relieved by the accumulation of thermal vacancies at the precipitate-matrix interface; however, as aging proceeds, eventually the growth of the precipitate particles and the relief of the supersaturation of the parent (Nb_{ss}) matrix causes the composition of the precipitates to adjust towards the equilibrium value.

3.5 Mechanical Properties

The equiaxed $\text{Nb}/\text{Nb}_3\text{Al}$ composite exhibited a Rockwell "C" (R_C) hardness of ~ 56 and a K_{Ic} plane-strain fracture toughness of $6.5 \text{ MPa}\sqrt{\text{m}}$. Bend strengths, determined in four-point bending, were $\sim 460 \text{ MPa}$, and the yield strength was estimated to be $\sim 220 \text{ MPa}$ (based on one-third of the Vicker's hardness [18]). The lamellar $\text{Nb}/\text{Nb}_3\text{Al}$ composite microstructure showed similar strength and toughness properties; the composite exhibited a R_C hardness of ~ 51 , an estimated yield strength of $\sim 177 \text{ MPa}$, and $K_{Ic} \sim 5.5 \text{ MPa}\sqrt{\text{m}}$. In contrast, the pure (monolithic) Nb_3Al material had a K_{Ic} of $1.1 \text{ MPa}\sqrt{\text{m}}$, an estimated yield strength of $\sim 274 \text{ MPa}$, and a four-point bend strength of $\sim 212 \text{ MPa}$.

The factor of six increase in toughness shown by the *in situ* $\text{Nb}/\text{Nb}_3\text{Al}$ composites compared to monolithic Nb_3Al can be attributed primarily to role of the ductile Nb_{ss} phase in bridging the crack, and to a lesser extent by plastic deformation in the ductile phase. As discussed in refs. [19, 20], zones of uncracked Nb_{ss} particles are found in the wake of the crack tip (Fig. 3.10). Their contribution to the toughening of Nb_3Al arises from the tractions produced by the uncracked ligaments in bridging the two crack surfaces, thereby partially shielding the crack tip from the remotely applied loads. Crack deflection, crack trapping, crack renucleation and decohesion along the Nb/matrix interfaces provide

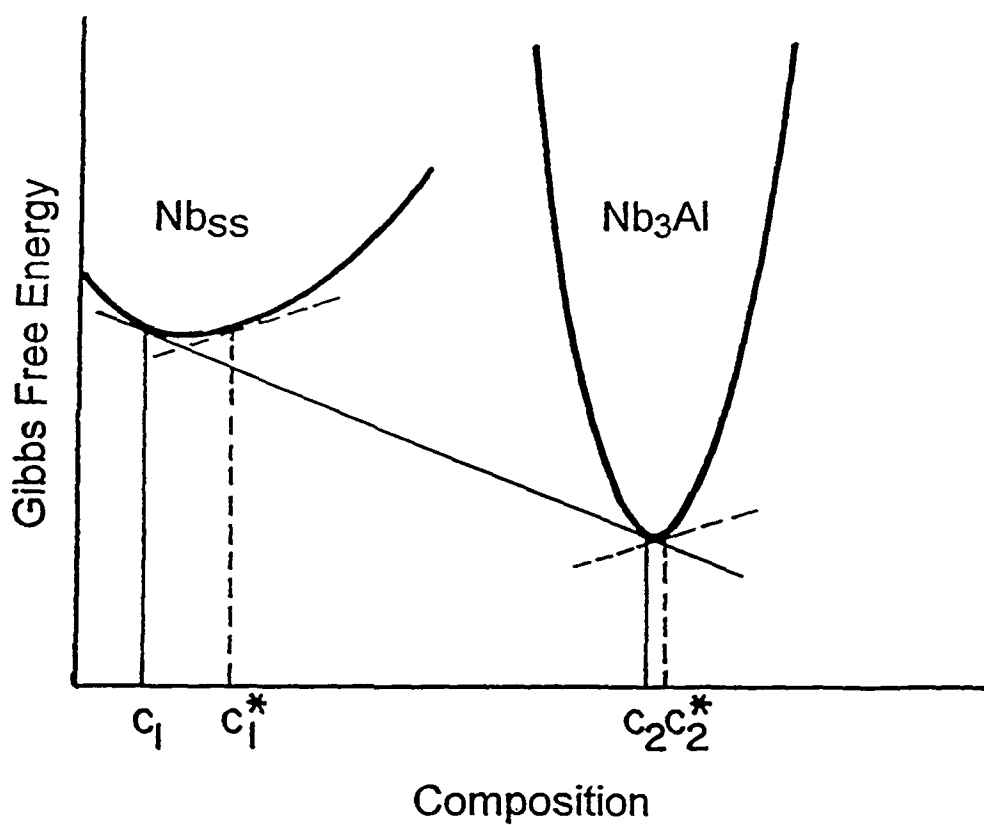


Fig. 3.9. Schematic illustration of Gibbs free energy vs. composition at given temperature. C_1 and C_2 are the equilibrium compositions of the hypothetical Nb_{SS} and Nb₃Al phases at this temperature. C_1^* is the composition of the supersaturated solid solution and C_2^* is the preferred composition of the initial Nb₃Al precipitate.

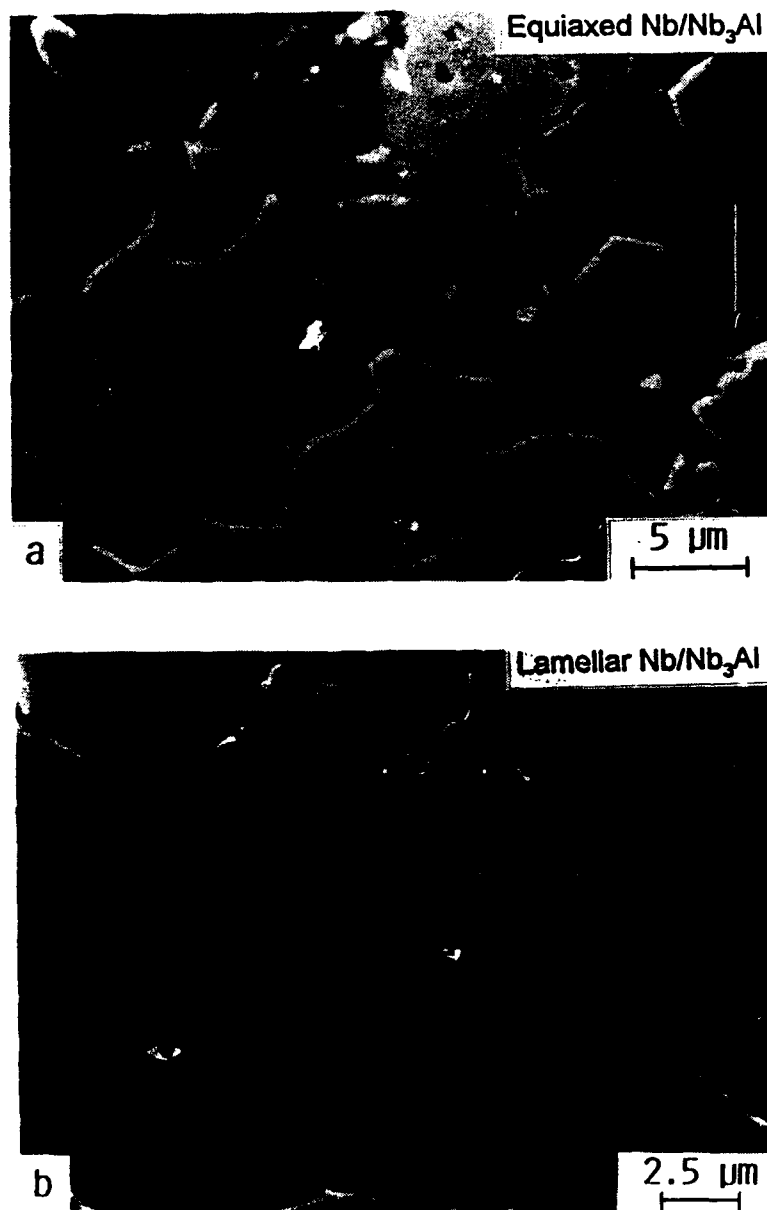


Fig. 3.10. Scanning electron micrograph of the crack-path profile in the (a) equiaxed and (b) lamellar Nb/Nb₃Al composite under monotonic loading, showing crack bridging.

additional toughening contributions. The toughening can be simply modeled under small-scale bridging conditions by considering that, at steady state, where the bridging zone is at a maximum length governed by ductile ligament rupture at a critical crack-opening displacement u^* , the fracture energy increase, ΔG_c , can be estimated in terms of the area fraction f of ductile ligaments intersecting the crack path, their uniaxial yield strength, σ_y , and a representative cross-sectional radius, r , as [21]:

$$\Delta G_c = f \sigma_y r \chi, \quad (1)$$

where χ is a dimensionless function representing the (normalized) work of rupture, given by [21]:

$$\chi = \int_0^{u^*} \frac{\sigma(u) du}{\sigma_y r} \quad (2)$$

χ can vary between ~ 0.5 and 8 , depending upon the degree of interface bonding and the constitutive properties of the reinforcement phase [22-24].

For the equiaxed Nb/Nb₃Al microstructure, taking the area fraction of the ductile Nb_{ss} phase intercepted by the crack path as $f \sim 0.28$ and using σ_y for Nb ~ 90 MPa, $E \sim 125$ GPa, particle size $r \sim 6$ μm and $\chi_{\text{Nb}} \sim 2$ [25], the increase in toughness from crack bridging is estimated to be $6 \text{ MPa}\sqrt{\text{m}}$. As the toughness of the Nb₃Al matrix is $1.1 \text{ MPa}\sqrt{\text{m}}$, the predicted toughness of the Nb/Nb₃Al composite is therefore $\sim 7 \text{ MPa}\sqrt{\text{m}}$, in accordance with the experimentally measured value. Using similar values for the lamellar Nb/Nb₃Al composite with $r \sim 1$ μm and $f \sim 0.4$ gives a composite toughness of $\sim 4 \text{ MPa}\sqrt{\text{m}}$ which is slightly lower than that observed experimentally ($K_{\text{Ic}} \sim 5.5 \text{ MPa}\sqrt{\text{m}}$).

3.6 Conclusions

Based on a study of the *in situ* processing of ductile-phase toughened Nb/Nb₃Al intermetallic-matrix composites, the following conclusions can be made:

1. By hot-pressing synthesized elemental Nb and Al powders mixed in the ratio of Nb-6 wt.% Al, an *in situ* Nb₃Al intermetallic-matrix composite can be processed that is ductile-phase toughened with equiaxed elemental Nb particles.
2. Utilizing thermal treatments, a duplex *in situ* composite microstructure of Nb_{ss}/Nb₃Al with a fine lamellar Nb phase can be processed by precipitation of the ordered Nb₃Al phase from the supersaturated Nb_{ss} solid solution; this

microstructure also shows ductile-phase toughening compared to unreinforced monolithic Nb₃Al.

3. The precipitation of Nb₃Al from the Nb_{ss} solid solution is seen to occur by a massive transformation resulting in the formation of coherent boundaries and deformation of the supersaturated solid solution.
4. The rod-like precipitates of Nb₃Al nucleate heterogeneously at grain boundaries and grow along preferential directions ($\langle 110 \rangle$ Nb_{ss} and $\langle 211 \rangle$ Nb₃Al) to relieve the internal strain in the parent matrix.
5. The resulting Nb_{ss}/Nb₃Al composites show a six-fold increase in fracture toughness compared to monolithic Nb₃Al. Such toughening is primarily attributed to crack bridging by uncracked Nb particles in the wake of the crack tip, and to plastic deformation within the Nb phase.

3.7 References

1. J. J. Stephens, *J. Metals* **42**, 22 (1990).
2. D. L. Anton, D. M. Shah, D. N. Duhal and A. F. Giamei, *J. Metals* **41**, 12 (1989).
3. D. L. Anton and D. M. Shah, in *High Temperature Structural Intermetallic Compounds*, edited by C. T. Liu *et al.*, Materials Research Society, Pittsburgh, PA, 1989, p. 361.
4. C. T. Liu and J. O. Stiegler, *Science* **226**, 636 (1984).
5. E. M. Schulson, *Int. J. Powder Met.* **23**:1, 25 (1987).
6. I. Baker and P. R. Munroe, *J. Metals* **40**, 28 (1988).
7. L. S. Sigl, P. A. Mataga, B. J. Dalgleish, R. M. McMeeking and A. G. Evans, *Acta Metall.* **36**, 945 (1988).
8. C. E. Lundin and A. S. Yamamoto, *Trans. Met. Soc. AIME*. **236**, 863 (1966).
9. L. Kohot, R. Horyn and N. Iliev, *J. Less Com. Met.* **44**, 215 (1976).
10. L. Jorda, R. Flukinger and J. Miller, *J. Less Com. Met.* **75**, 227 (1980).

11. R. M. Waterstrat and E. C. van Reuth, in *Ordered Intermetallic Alloys*, Proc. 3rd Bolton Landing Conference, edited by B. H. Kear, C. T. Sims, N. S. Stoloff and J. H. Westbrook, Caltor's Publishing Division, Baton Rouge, p. 95 (1970).
12. M. Khantha, V. Vitek and D. P. Pope, *Mater. Res. Soc. Symp. Proc.* **133**, 99 (1989).
13. R. Flukinger, in *Superconductor Materials Science-Metallurgy, Fabrication and Applications*, edited by S. Foner and B. B. Schawrtz, Plenum, New York, p.511 (1982).
14. T. B. Massalski, H. Okamoto, P. R. Subramanion and L. Kacprzak (eds.), *Binary Phase Diagrams*, ASM, Metals Park, OH (1986).
15. M. Hong and J. W. Morris, Jr., *Appl. Phys. Lett.* **37**, 1044 (1980).
16. M. Hong, *Ph.D. Thesis*, University of California, Berkeley, 1980.
17. J. W. Gibbs, *The Scientific Papers of J. Willard Gibbs, Vol. I Thermodynamics* (Dover, New York, NY, 1961).
18. D. Tabor, *The Hardness of Metals*, Oxford University Press, New York, NY, 1951.
19. L. Murugesh, K. T. Venkateswara Rao, L. C. DeJonghe, and R. O. Ritchie, in *Intermetallic Matrix Composites II*, edited by D. Miracle, J. Graves, and D. Anton, MRS Conference Proceedings vol. 273, Materials Research Society, Pittsburgh, PA, 1992, p. 433.
20. L. Murugesh, K. T. Venkateswara Rao, and R. O. Ritchie, *Scripta Metall. Mater.* **27** (1993) in review.
21. M. F. Ashby, F. J. Blunt, and M. Bannister, *Acta Metall.* **37**, 1847 (1989).
22. H. E. Dève, A. G. Evans, G. R. Odette, R. Mehrabian, M. L. Emiliani, and R. J. Hecht, *Acta Metall. Mater.* **38**, 1491 (1990).
23. G. R. Odette, H. E. Dève, C. K. Elliott, A. Hasigawa, and G. E. Lucas, in *Interfaces in Ceramic Metal Composites*, edited by R. J. Arsenault, R. Y. Lin, G. P. Martins, and S. G. Fishman, TMS-AIME, Warrendale, PA, 1990, p. 443.
24. H. C. Cao, B. J. Dalgleish, H. E. Dève, C. K. Elliott, A. G. Evans, R. Mehrabian, and G. R. Odette, *Acta Metall. Mater.* **37**, 2969 (1989).
25. P. A. Mataga, *Acta Metall. Mater.* **37**, 3349 (1989).

4. FRACTURE TOUGHNESS AND FATIGUE-CRACK GROWTH IN Nb-DUCTILE-PHASE-TOUGHENED Nb₃Al *IN SITU* INTERMETALLIC COMPOSITES

4.1 Introduction

As discussed in Section 3, model high-melting temperature Nb/Nb₃Al composites have been fabricated by hot pressing elemental Nb and Al powders mixed in the ratio Nb-6 wt. % Al [1]. The microstructure features equiaxed islands of Nb solid solution (~40 vol.%) in a brittle Nb₃Al matrix. Utilizing the peritectic reaction at 2060°C, thermal treatment for 24 h at 1800°C followed by annealing at 1450°C, results in a lamellar microstructure containing a uniform and rather fine distribution of filamentary Nb solid solution in a Nb₃Al matrix. In this section, the fatigue and fracture resistance of the equiaxed and lamellar composites are examined and compared to corresponding properties in the unreinforced constituent phases, pure Nb₃Al and Nb.

4.2 Fracture Toughness and Fatigue Crack Growth Testing

Fatigue-crack growth behavior under cyclic tension loading was examined using 38 mm-diameter, 28 mm-wide and 2.5 mm-thick disc-shaped DC(T) specimens, with a wedge-shaped starter notch to assist precracking. Specimens were cut using electrical-discharge machining. Tests were performed manually on electro-servo-hydraulic testing machines operating under load control, in room temperature air (22°C and ~45 % relative humidity), at a load ratio ($R = K_{\min}/K_{\max}$) of 0.1 and a test frequency of 25 Hz (sine wave). Limited testing at frequencies of 0.025, 0.25 and 2.5 Hz was also conducted to observe the effect of strain rate on the fracture morphology of the ductile reinforcing phase. Growth rates over the range of $\sim 10^{-10}$ to 10^{-6} m/cycle were measured under load-shedding conditions, with crack lengths continuously monitored *in situ* (resolution $\pm 2 \mu\text{m}$) by measuring the electrical resistance of thin metallic foils bonded onto the specimen surface. Results are presented in the form of crack-growth rates per cycle (da/dN) as a function of the applied stress-intensity range, ($\Delta K = K_{\max} - K_{\min}$).

Corresponding fracture-toughness behavior was evaluated by subsequently monotonically loading the fatigue-cracked samples to failure in room temperature air in order to determine resistance curves (R-curves), characterized by the crack-growth resistance (K_R) as a function of the crack extension (Δa). Several strain rates were used corresponding to \dot{K}_I of 0.04 to 5 MPa $\sqrt{\text{m/s}}$. In addition, all fracture surfaces and

metallographic sections of the crack path were examined using scanning electron microscopy (SEM).

4.3 Fracture Toughness Behavior

Measurements of the fracture toughness of the equiaxed Nb/Nb₃Al composite at slow strain rates ($\dot{K}_I \sim 0.04 \text{ MPa}\sqrt{\text{m/s}}$) [2] show that with ~40 vol.% Nb phase, the toughness increases from a K_{Ic} of $1.1 \text{ MPa}\sqrt{\text{m}}$ for the monolithic Nb₃Al to $\sim 6.5 \text{ MPa}\sqrt{\text{m}}$ (plateau value) in the equiaxed composite (Fig. 4.1). For the lamellar Nb/Nb₃Al composite, the maximum value on the R-curve was $\sim 5.5 \text{ MPa}\sqrt{\text{m}}$ for the lamellar composite. The toughness of the pure Nb was $\sim 16 \text{ MPa}\sqrt{\text{m}}$. Figure 4.2(a,c) shows crack profiles in the equiaxed and lamellar composites under monotonic loading at slow ($\dot{K} \sim 0.04 \text{ MPa}\sqrt{\text{m/s}}$) strain rates.

Metallographically, fracture surfaces in the equiaxed Nb/Nb₃Al composite revealed that roughly two-thirds of the Nb particles intersect the crack path and provide some impedance to crack advance; the crack deflects around the remaining third of the particles, which are generally the smallest ones with a size less than $\sim 2 \mu\text{m}$. Crack paths under monotonic loading show extensive crack bridging by unbroken ductile Nb particles in the wake of the crack tip (Fig. 4.3a). This provides the main contribution to the toughness of the composite, although additional toughening results from crack deflection around small Nb particles, secondary cracking of the matrix and plastic deformation in the particle. The latter process is evident from the marked plastic stretching and rupture by microvoid coalescence of the Nb particles at failure (Fig. 4.3b).

For the lamellar Nb/Nb₃Al composite, the crack path again shows definitive bridging zones under monotonic loading (Fig. 4.4a) with Nb lamellae ultimately failing by ductile rupture (Fig. 4.4b). However, additionally, extensive microcracking exists ahead of the crack tip, which clearly would contribute to toughening.

At high strain rates ($\dot{K}_I \sim 5 \text{ MPa}\sqrt{\text{m/s}}$), conversely, the equiaxed Nb/Nb₃Al composite displays a different behavior; the ductile Nb fails by a brittle cleavage mechanism, with a corresponding reduction in the K_{Ic} to $\sim 4.8 \text{ MPa}\sqrt{\text{m}}$. In comparison, pure Nb₃Al showed no R-curve behavior and crack growth was coincident with instability, at a $K_{Ic} \sim 1.1 \text{ MPa}\sqrt{\text{m}}$. Crack paths displayed no apparent impediment to crack growth (Fig. 4.5a) with fracture surfaces consisting of 100% transgranular cleavage (Fig. 4.5b).

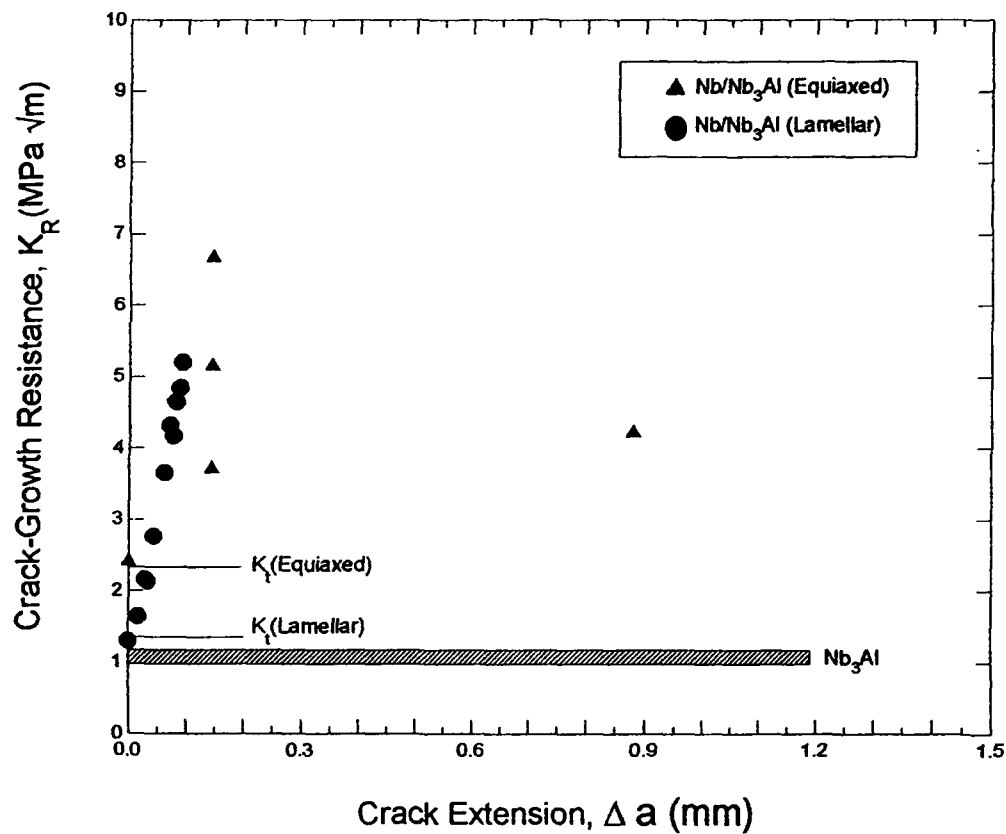


Fig. 4.1. Crack resistance (R) curves for the equiaxed and lamellar Nb/Nb₃Al composites under monotonic loading, as compared to monolithic Nb₃Al. The bridging zones were typically ~100 μ m in length with additional microcracking in the case of the lamellar composite.

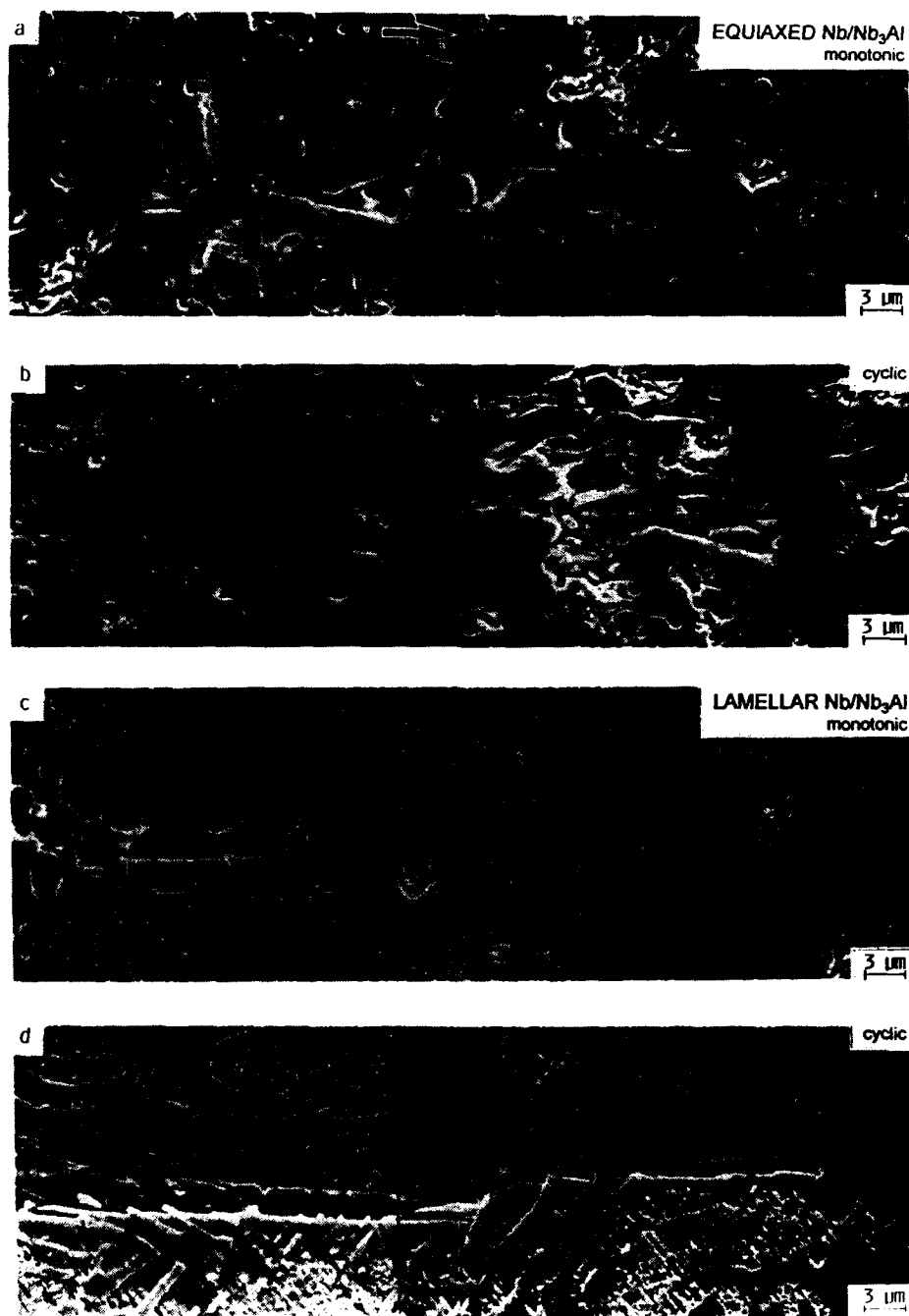


Fig. 4.2. SEM micrographs of crack profiles obtained for the equiaxed Nb/Nb₃Al composite under (a) monotonic loading and (b) cyclic loading, and for the lamellar Nb₃Al/Nb composite under (c) monotonic loading and (d) cyclic loading.

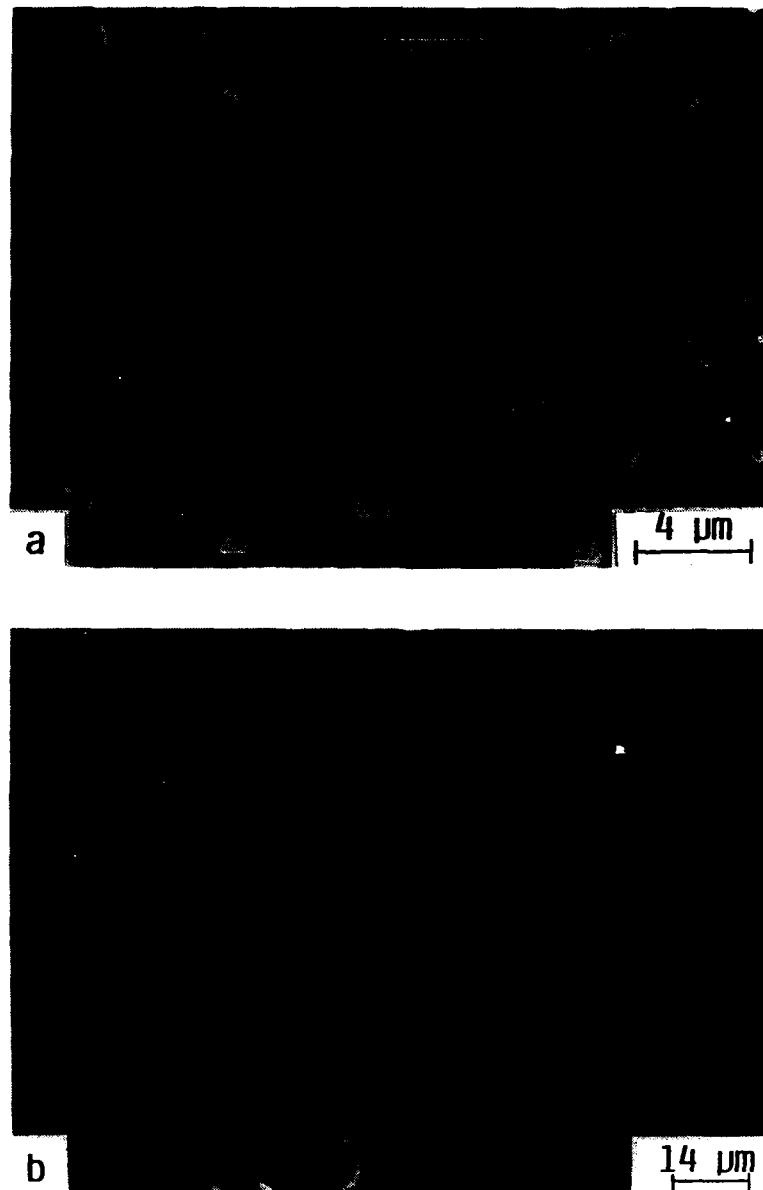


Fig. 4.3. SEM micrographs in the equiaxed Nb/Nb₃Al composite under monotonic loading (a) of the crack profile showing crack bridging by intact Nb particles, and (b) of the fracture surface showing plastic stretching and rupture by microvoid coalescence of the Nb particles. Arrow indicates direction of crack advance.

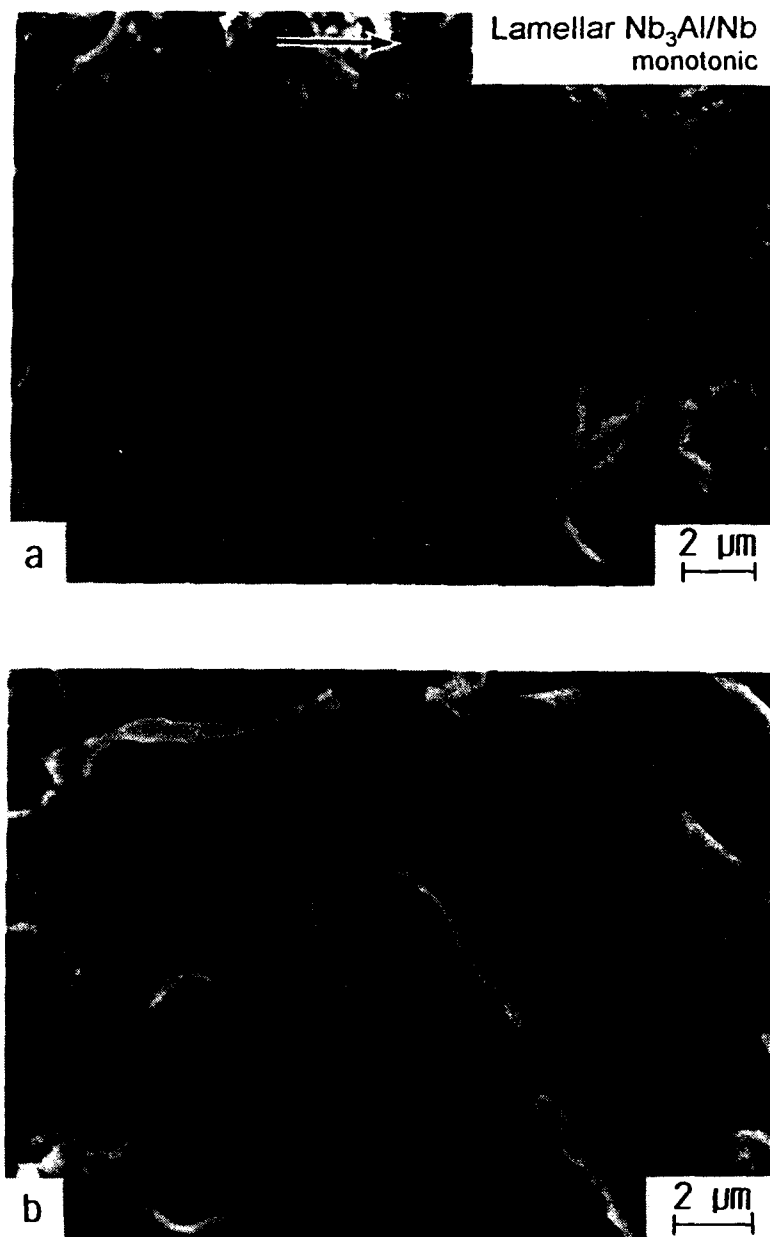


Fig. 4.4. SEM micrographs in the lamellar Nb/Nb₃Al composite under monotonic loading (a) of the crack profile showing crack bridging by intact Nb lamellae, and (b) of the fracture surface showing plastic stretching of the Nb lamellae. Arrow indicates direction of crack advance.

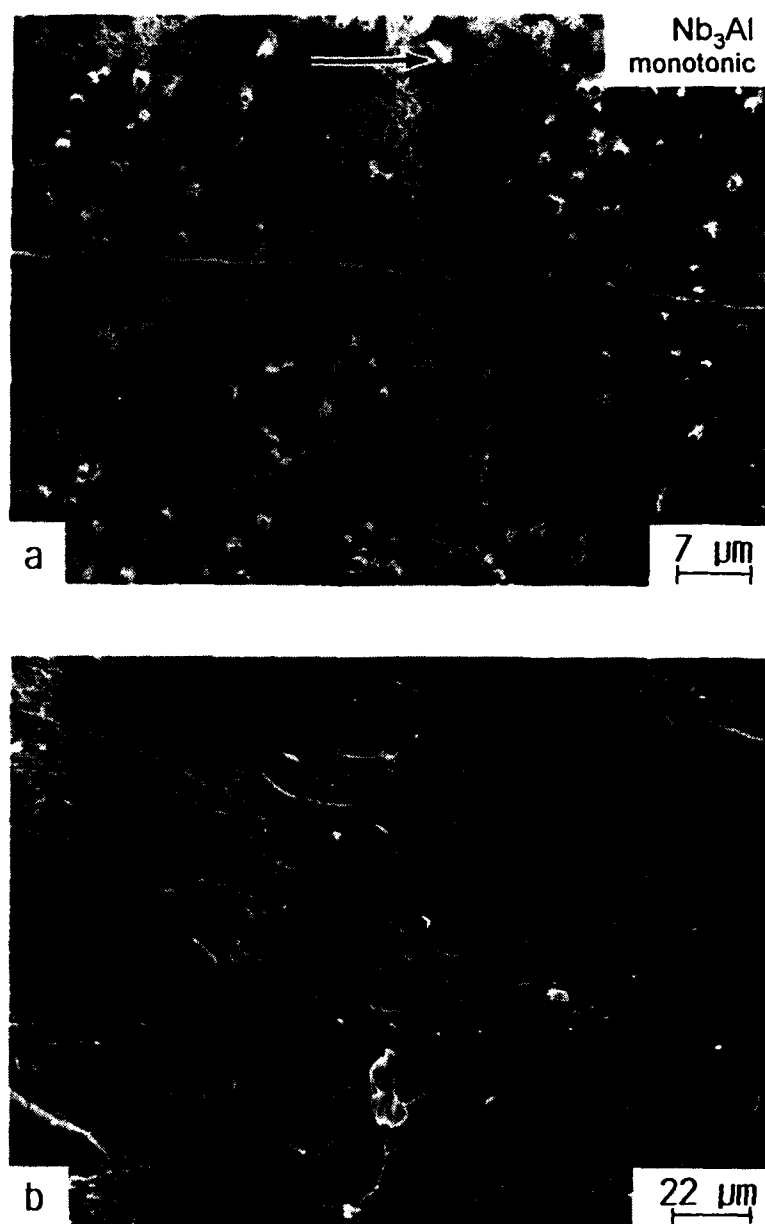


Fig. 4.5. SEM micrographs of monolithic Nb_3Al under monotonic loading (a) of the crack profile showing no impediment to crack growth, and (b) of the fracture surface showing failure by a cleavage mechanism. Arrow indicates direction of crack advance.

4.4 Cyclic Fatigue-Crack Growth Behavior

The variation in fatigue-crack growth rates as a function of the applied stress intensity range ΔK , at a loading ratio $R = 0.1$, for the equiaxed and lamellar Nb/Nb₃Al composites composite are shown in Figure 4.6, and are compared with corresponding results for unreinforced Nb₃Al and Nb. Similar to many intermetallics, growth rates in Nb/Nb₃Al are strongly dependent upon ΔK ; simply expressed in terms of a Paris power-law relationship ($da/dN \propto \Delta K^m$), the exponents m are in the range of ~ 10 -25. This should be compared with m values for structural metallic materials in this growth-rate regime which typically range between 2 and 4 [3].

Crack-particle interactions under cyclic loading (at 25 Hz) are different than those observed under monotonic loading. In general, fatigue cracks tend to avoid the small equiaxed Nb particles; where they do intercept the Nb though, failure occurs by a part brittle-part ductile fatigue mechanism. As seen in Figure 4.7b, most of the particles fail by a cleavage-type mechanism, while others show evidence of ductile fatigue striations. Such cleavage-type fatigue failure is not unusual in bcc metals, particularly at low temperatures and high strain rates [4-8], and is generally termed "cyclic cleavage".

For the lamellar Nb/Nb₃Al composite, fatigue cracks cannot avoid the ductile Nb phase and failure again occurs by a mixed ductile-brittle mechanism (Fig. 4.8). At low ΔK values, a ductile striation fatigue failure is prominent while at the high ΔK a mixed brittle-ductile failure occurs with evidence of cyclic cleavage (Fig. 4.9). Microcracking and secondary matrix cracks are substantially less evident than during monotonic loading.

The cyclic cleavage mechanism is also seen in pure Nb samples; presumably this accounts for the high fatigue-exponent of $m \sim 10$. Here, at a frequency of 25 Hz, fatigue-crack advance occurs by a cleavage mechanism, with isolated regions of ductile striations among the cleaved grains particularly at low ΔK levels; at high ΔK levels where the majority of the fracture occurs by cyclic cleavage, these ductile regions act as temporary crack arrest sites (Fig. 4.10). Thresholds for crack growth in Nb are quite high, between 7 to 8 MPa \sqrt{m} . In marked contrast, fatigue cracks in pure Nb₃Al grow at very low stress intensities ($\Delta K_{TH} \sim 0.6$ -0.8 MPa \sqrt{m}) with an eventually featureless fracture surface (Fig. 4.11).

In summary, it is apparent that the potency of ductile-phase toughening by Nb particles is diminished under cyclic loading due to premature fatigue failure of the Nb; however, the fatigue-crack growth resistance of the Nb-phase reinforced Nb₃Al composites is nevertheless improved compared to monolithic Nb₃Al.

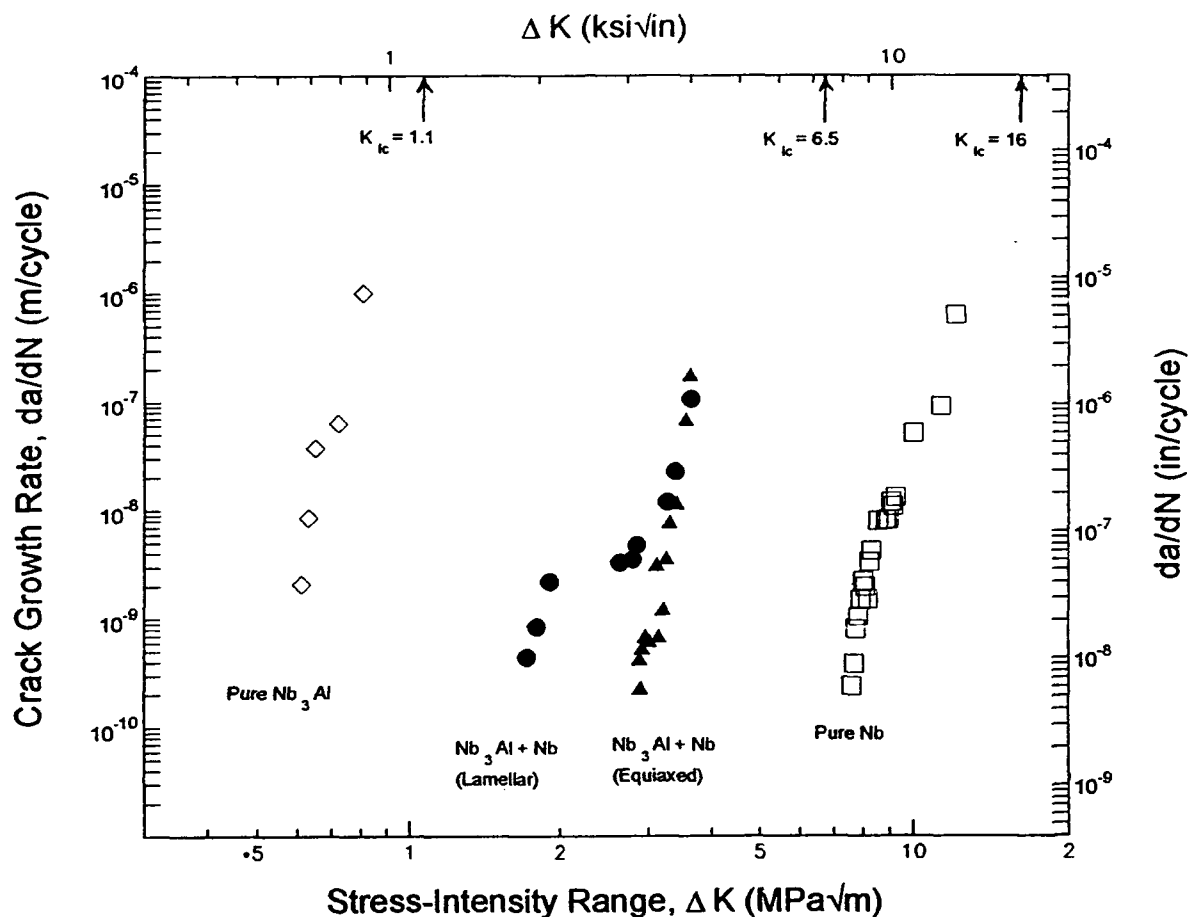


Fig. 4.6. Variation in cyclic fatigue-crack propagation rates, da/dN , as a function of the applied stress-intensity range, ΔK , in the equiaxed $\text{Nb}/\text{Nb}_3\text{Al}$ composite and the lamellar $\text{Nb}/\text{Nb}_3\text{Al}$ composite. Data for pure Nb and monolithic Nb_3Al are also shown for comparison. Testing was performed in room temperature air at a load ratio $R = 0.1$ and test frequency of 25 Hz.

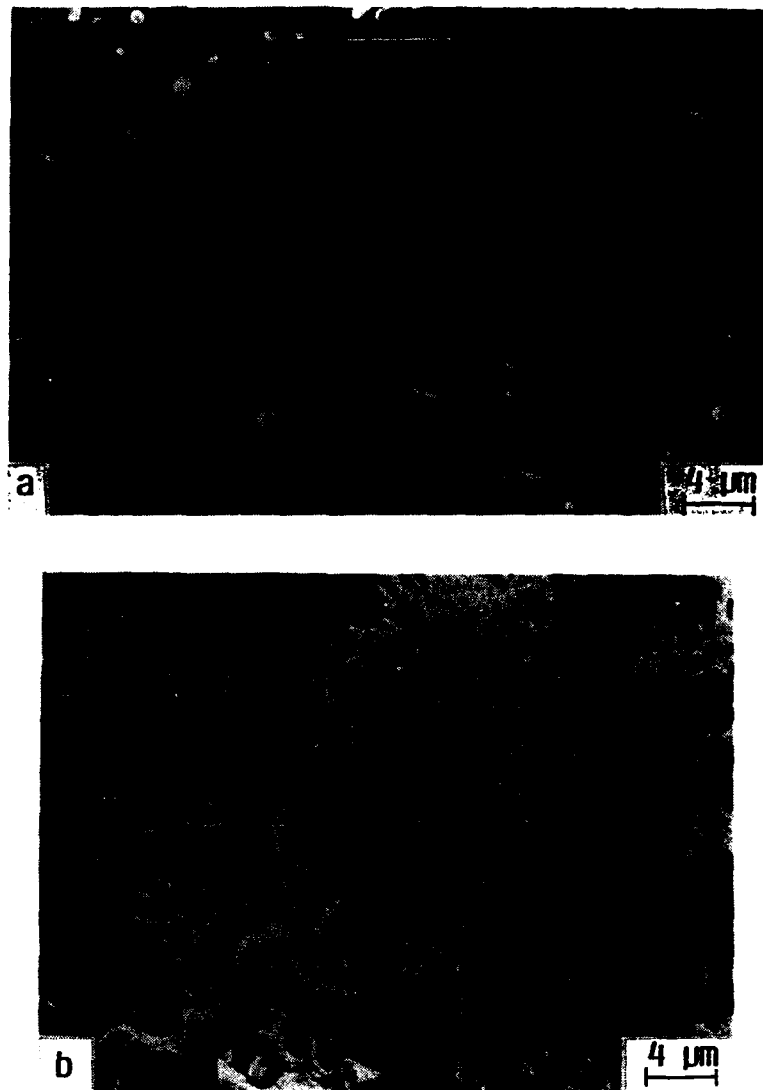


Fig. 4.7. SEM micrographs in the equiaxed Nb/Nb₃Al composite under cyclic loading (a) of the crack profile showing cracked Nb particles, and (b) of the fracture surface showing fatigue failure of the Nb particles by "cyclic cleavage". Arrow indicates direction of crack advance.

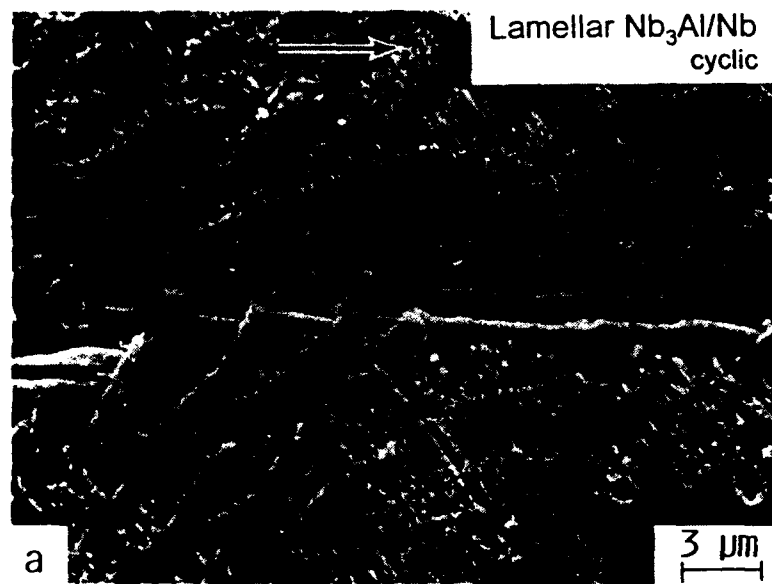


Fig. 4.8. SEM micrographs in the lamellar Nb/Nb₃Al composite under cyclic loading (a) of the crack profile showing cracked Nb lamellae behind the crack tip, and (b) of the fracture surface showing fatigue failure of the Nb particles by "cyclic cleavage". Arrow indicates direction of crack advance.

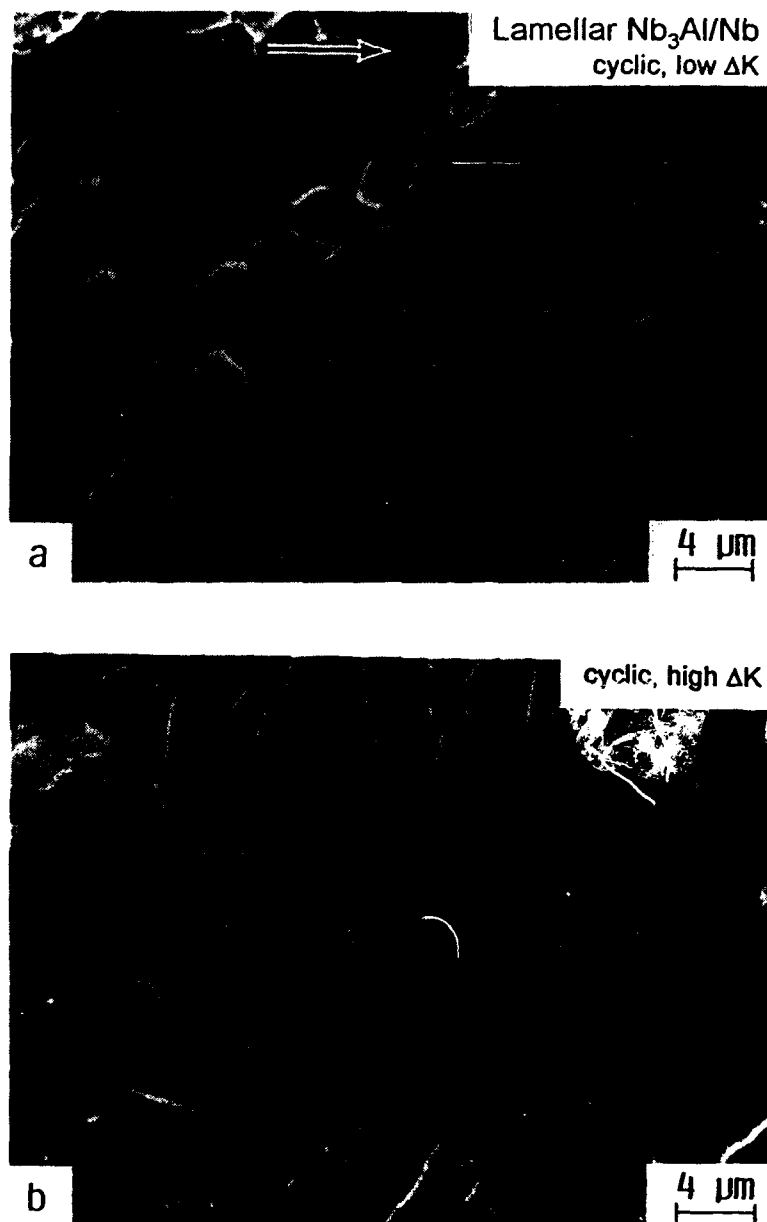


Fig. 4.9. SEM micrographs in the lamellar $\text{Nb}/\text{Nb}_3\text{Al}$ composite under cyclic loading (a) at low stress intensity showing ductile striations and (b) at a high stress intensity showing failure by a mixed ductile-brittle mode.

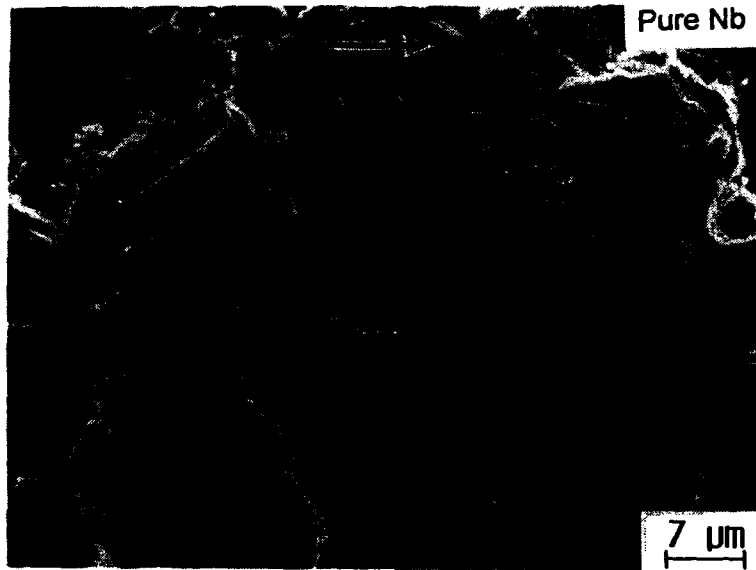


Fig. 4.10. SEM micrograph of cyclic fatigue failure in pure Nb, showing fracture by "cyclic cleavage" with isolated regions of ductile striations. Arrow indicates direction of crack advance.

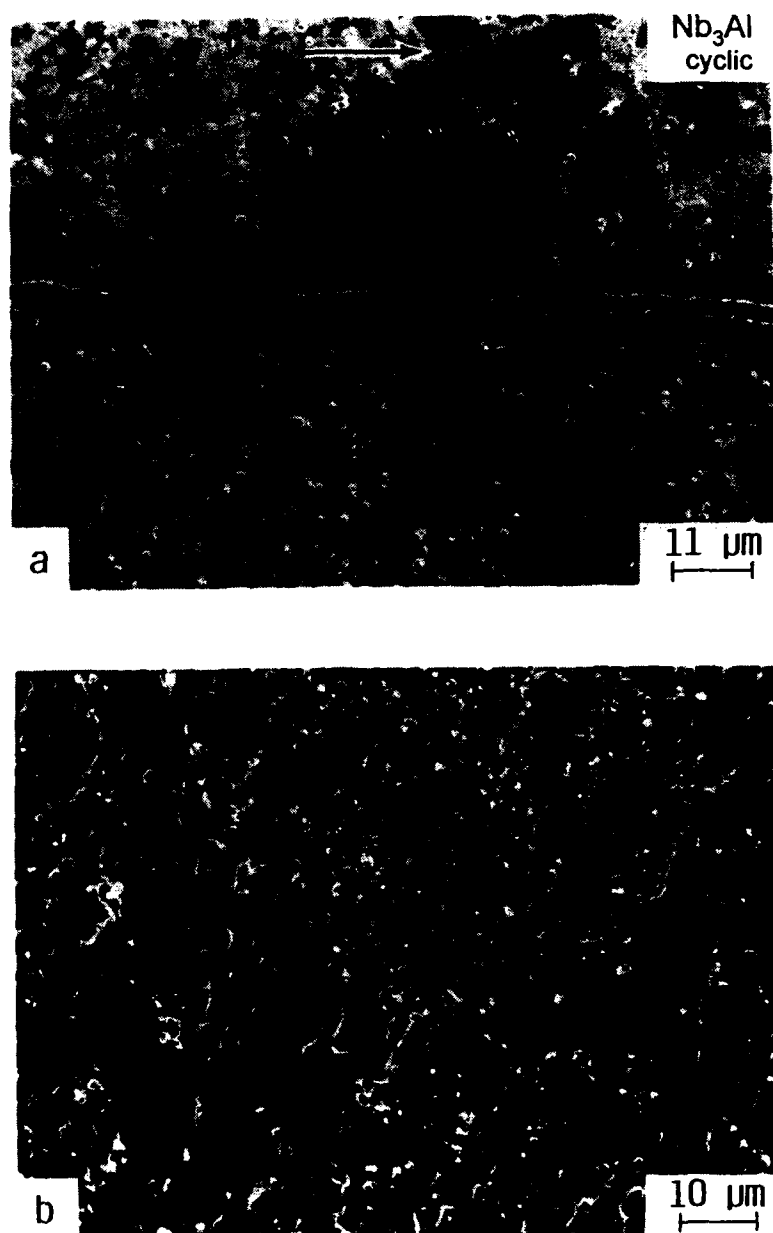


Fig. 4.11. SEM micrographs of monolithic Nb₃Al under cyclic loading (a) of the crack profile showing no impediment to crack growth, and (b) of the fracture surface showing failure by a cleavage-type mechanism with some evidence of striations. Arrow indicates direction of crack advance.

4.5 Effect of Strain-Rate Under Cyclic Loading

To examine the effect of strain rate on the fatigue failure mechanisms under cyclic loading, the equiaxed Nb/Nb₃Al composite was cyclically loaded at different frequencies. Samples were tested at sinusoidal frequencies of 0.025 Hz, 0.25 Hz, 2.5 Hz and 25 Hz, which represent \dot{K}_I 's of 0.1, 1, 10 and 100 MPa $\sqrt{m/s}$ respectively, at a ΔK of ~ 4 MPa \sqrt{m} . The resulting variation in fatigue-crack growth rates at 25 Hz and 0.025 Hz ($R = 0.1$) are shown in Figure 4.12. Although data were not obtained at the very low ΔK levels due to time constraints, above $\Delta K \sim 4$ MPa \sqrt{m} as K_{max} approaches K_{Ic} , growth rates are accelerated at the higher frequency. Specifically, this occurs close to $K_{Ic} \sim 4.8$ MPa \sqrt{m} at 25 Hz compared to $K_{Ic} \sim 6.5$ MPa \sqrt{m} at 0.025 Hz.

Crack-particle interactions under cyclic loading at the two strain rates are considerably different. Although the fatigue cracks always avoided small particles with diameters typically less than $\sim 2 \mu m$, the larger particles failed by ductile striations at the very slow strain-rates (Fig. 4.13a), and cyclic cleavage at the high strain rates (Fig. 4.13d), the latter mechanism being also favored at high ΔK levels. Concomitant with this fracture mode transition, crack-growth rates increase by as much as three orders of magnitude for the same ΔK ; similar behavior is seen in the pure Nb samples.

4.6 Discussion

The increase in fracture toughness of a brittle intermetallic matrix due to reinforcement by ductile phases can be modelled by considering the increase in the strain energy release rate caused by the intact bridging ligaments spanning the crack. Provided the crack path intercepts the reinforcing phase, the dominant contribution to toughening arises from tractions provided by the two crack surfaces, thus partially shielding the crack tip from remote loads. In addition, toughening contributions from crack deflection, crack trapping, crack renucleation and decohesion along the particle-matrix interface further accentuate this effect. The extent of toughening depends on the length of the bridging zone in the wake of the crack tip; at steady state, where the zone is at a maximum length governed by ductile ligament rupture at a critical crack-opening displacement u^* , the steady-state fracture energy increase ΔG_c , has been estimated in terms of the area fraction f of ductile ligaments intersecting the crack path, their uniaxial yield strength, σ_y , and a representative cross-sectional radius, r , as [9]:

$$\Delta G_c = f \sigma_y r \chi, \quad (1)$$

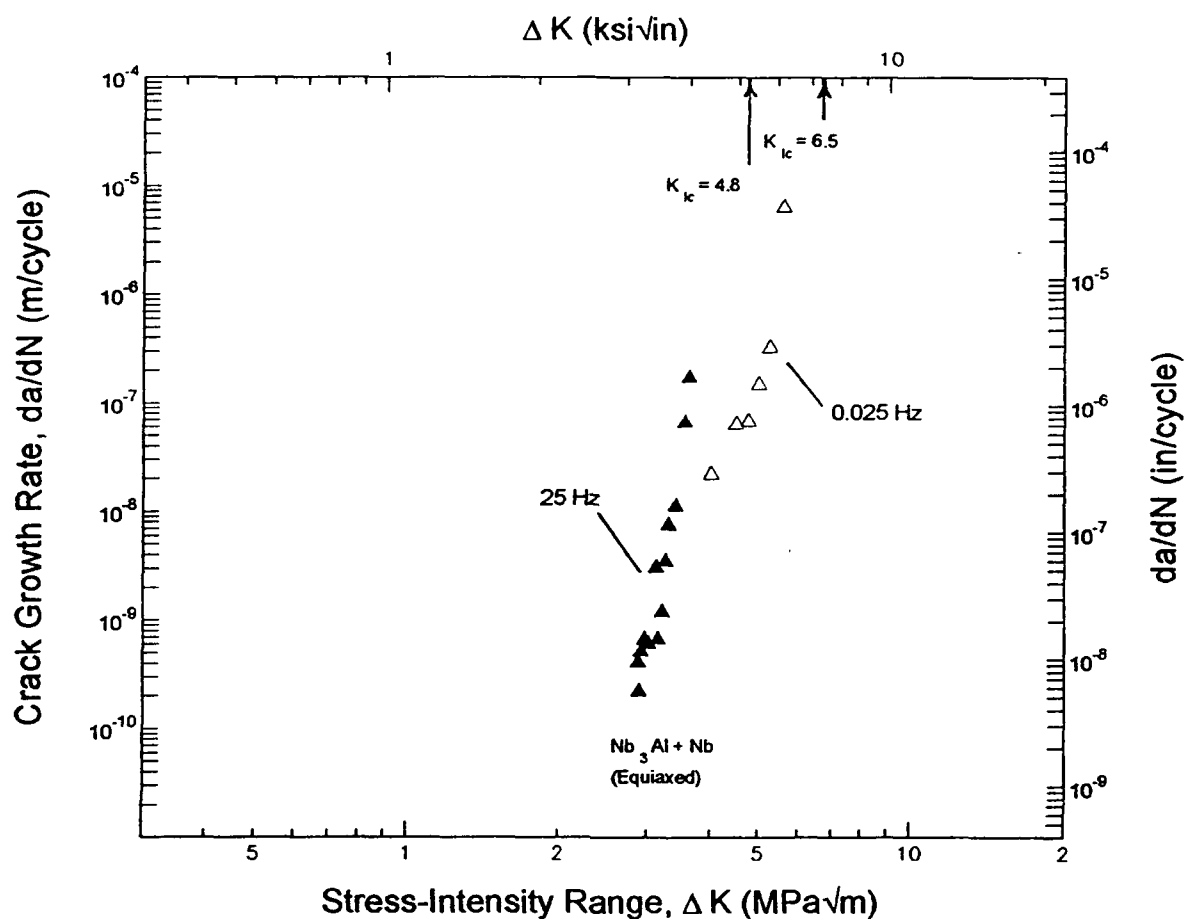


Fig. 4.12. Variation in cyclic fatigue-crack propagation rates, da/dN , as a function of the applied stress-intensity range, ΔK , in the equiaxed Nb/Nb_3Al composite tested at frequencies of 25 Hz and 0.025 Hz. Testing was performed in room temperature air at a load ratio $R = 0.1$.

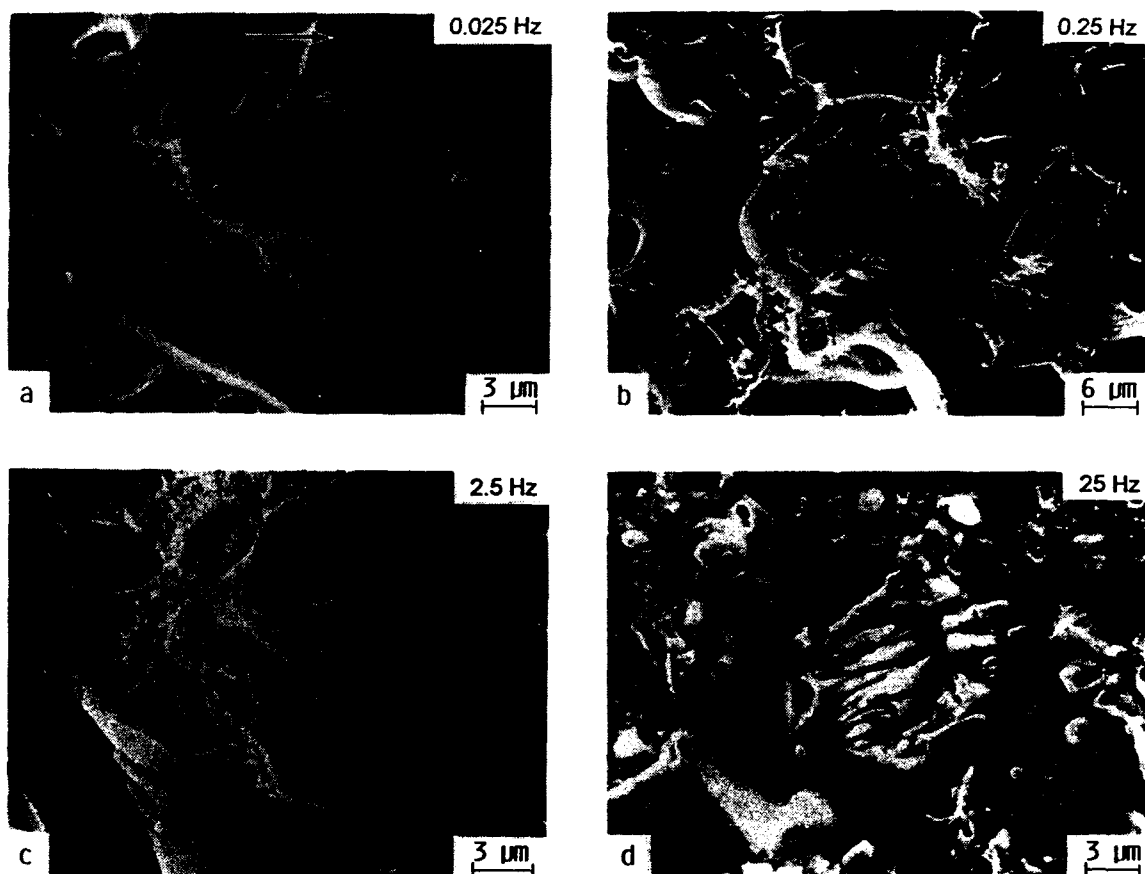


Fig. 4.13. SEM micrographs of Nb particles in the equiaxed Nb/Nb₃Al composite under cyclic loading at test frequencies of (a) 0.025 Hz, (b) 0.25 Hz, (c) 2.5 Hz and (d) 25 Hz. All tests were conducted at similar stress intensities ($\Delta K \sim 4$ MPa \sqrt{m}) and at room temperature.

where χ is a dimensionless function representing the work of rupture, given by [9]:

$$\chi = \int_0^{u^*} \frac{\sigma(u) du}{\sigma_y \cdot r} \quad (2)$$

which can vary between ~ 0.5 and ~ 8 , depending upon the degree of interface debonding and constitutive properties of the reinforcement phase [10-12]. Note that this formulation only applies when the size of the bridging zone is small compared to crack length and specimen dimensions (small-scale bridging).

For the equiaxed microstructure, estimating the area fraction of ductile Nb phase that is intercepted by the crack path as $f \sim 0.28$ and using σ_y for Nb ~ 90 MPa (taken as one-third the Vickers hardness [13]), particle size $r \sim 6 \mu\text{m}$ and $\chi_{Nb} \sim 2$ [14], the increase in toughness from crack bridging is $\sim 6 \text{ MPa}\sqrt{\text{m}}$. For a toughness of $\sim 1.1 \text{ MPa}\sqrt{\text{m}}$ for the monolithic Nb_3Al , the increase in toughness by the incorporation of the ductile phase gives a composite toughness of $\sim 7 \text{ MPa}\sqrt{\text{m}}$, which agrees well with the experimental result of $K_{Ic} \sim 6.5 \text{ MPa}\sqrt{\text{m}}$.

For the lamellar microstructure, estimating the area fraction of ductile phase intercepted by the crack path as $f \sim 0.4$ and again using $\sigma_y \sim 90$ MPa, lamellae thickness, $r \sim 1 \mu\text{m}$ and $\chi_{Nb} \sim 2$; the increase in toughness from crack bridging is $\sim 3 \text{ MPa}\sqrt{\text{m}}$. For a monolithic Nb_3Al toughness of $\sim 1.1 \text{ MPa}\sqrt{\text{m}}$, the increase in toughness by the incorporation of the ductile phase gives a composite toughness of $\sim 4 \text{ MPa}\sqrt{\text{m}}$. The higher experimental values ($K_{Ic} \sim 5.5 \text{ MPa}\sqrt{\text{m}}$) measured maybe due to additional toughening from microcracking ahead of the crack tip (Fig 4.2c) which acts to lower the effective near-tip stress intensity.

The absence of any significant crack-particle interactions in the two composites under cyclic loading can result from several factors. The cyclic failure of the Nb bridges is perhaps not too unexpected as metallic materials are known to be susceptible to fatigue failure. Moreover, Nb is readily embrittled by interstitial impurities such as C, H, N and O, and is thus especially prone to cracking [15-17]. Furthermore, since the Nb particles fail at stress intensities as low as $2\text{-}3 \text{ MPa}\sqrt{\text{m}}$, the toughening contribution from the deformation of the Nb would naturally be smaller than under monotonic loads where the particles fracture by microvoid coalescence at higher stress intensities of $5\text{-}6 \text{ MPa}\sqrt{\text{m}}$. The cyclic cleavage failure of the Nb particles in the composite is consistent with that observed in pure Nb. Here, at the higher test frequencies, fatigue occurs by a "cyclic cleavage"

mechanism, with isolated areas of ductile striations among the cleaved grains particularly at low ΔK levels; at high ΔK where the majority of the fracture occurs by cyclic cleavage, these areas act as temporary crack arrest sites [8].

As Nb is highly susceptible to hydrogen pick-up, which can lead to markedly increased fatigue-crack growth rates [15-17], this may promote the premature failure of the Nb particles and the absence of crack-bridging phenomena in the Nb/Nb₃Al composites under cyclic loading conditions. However, as seen in Figure 4.14, the fatigue data for the Nb used in this study matched well with that of pure Nb (0 ppm hydrogen). Moreover, extensive efforts were taken to avoid hydrogen pick up in the Nb by eliminating any processing operations involving hydriding of the Nb particles. In addition, the long aging time for the lamellar composite in an inert atmosphere eliminates hydrogen and other interstitials quite effectively. Thus any effect of hydrogen embrittlement is likely to be small.

An reason why the Nb particles fail so readily in fatigue is that under the higher frequencies associated with cyclic loading, the increased strain rate promotes brittle fracture of the Nb by cyclic cleavage, rather than the ductile rupture mechanism which occurs during quasi-static toughness tests. This is confirmed by the change in failure mechanism observed with varying frequency under cyclic loading. Figure 4.15 shows crack profiles under monotonic as well as cyclic loading for the equiaxed and lamellar Nb/Nb₃Al composites.

It has been shown that the cyclic deformation of bcc metals such as niobium is sensitive to temperature, strain rate, and direction of deformation [4-8,18-20]. At low temperatures ($T < 0.2 T_m$) or high strain rates at $T \sim 0.2 T_m$, bcc Nb exhibits a deformation response that is strongly dependent on temperature and strain rate, $\dot{\epsilon}$. The dependence of the flow stress on temperature and strain rate is usually expressed in terms of an athermal stress and an effective stress as follows [18-20]:

$$\sigma = \sigma_g + \sigma^*(\dot{\epsilon}, T) \quad (3)$$

where σ_g is the athermal component that arises from the long-range interaction of gliding dislocations with the structure and varies weakly with temperature to the same degree as the shear modulus, and σ^* is the effective stress that depends on $\dot{\epsilon}$ and T but only weakly on the density and arrangement of the dislocations.

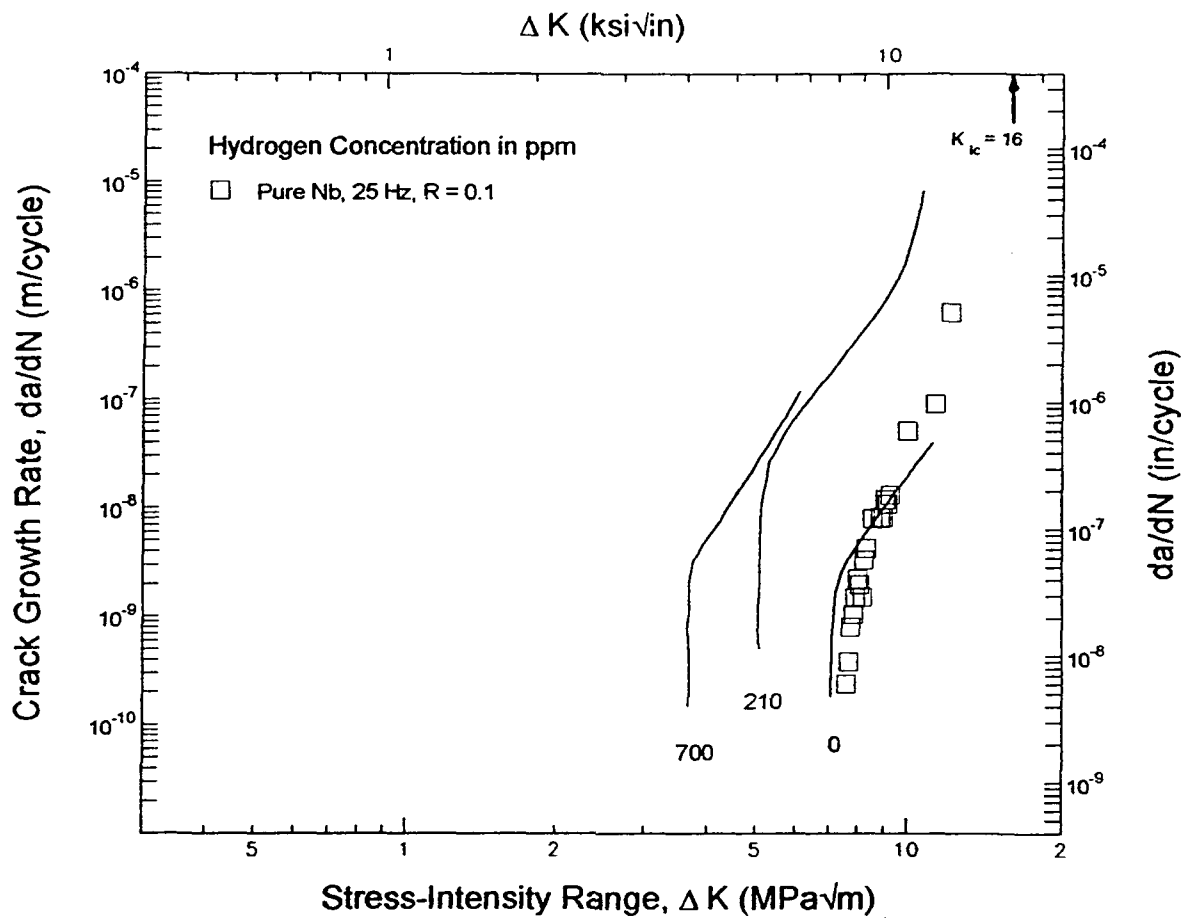


Fig. 4.14. The effect of hydrogen on the cyclic fatigue-crack propagation rate, da/dN , as a function of the applied stress-intensity range, ΔK for a Nb sample. Data for pure Nb is compared with data [from ref. 14].

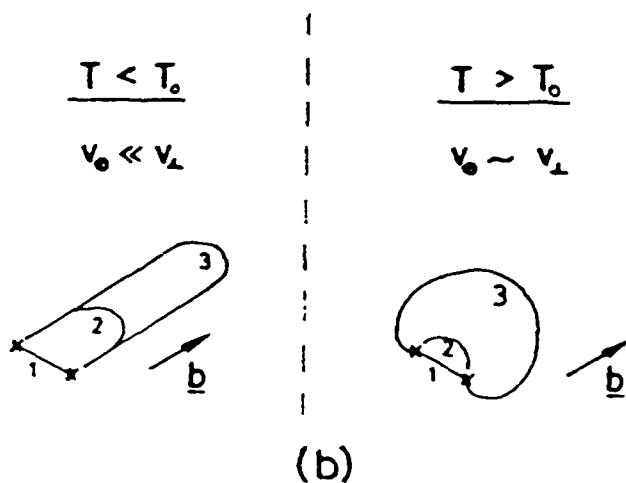
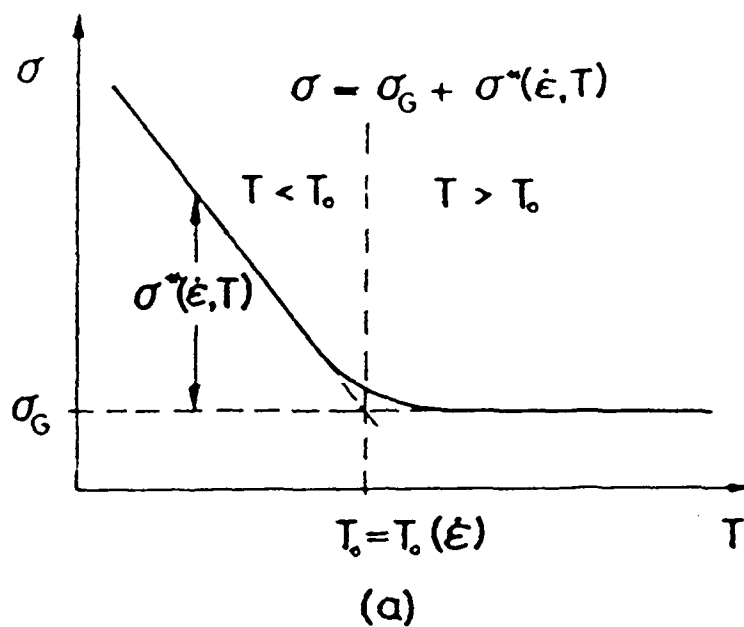


Fig. 4.15. Temperature dependence of the deformation behavior of bcc metals (schematically) (a) temperature dependence of the flow stress σ and (b) glide mode of dislocation segment (anchored at two pinning points) at low and intermediate temperatures.

In niobium, as with other bcc metals, the physical source of the large effective stress is the limited mobility of the screw dislocations at low temperatures. The glide of the screw dislocations occurs by the thermally activated formation of kink pairs [18] (double-kink nucleation). As a result, the mobility of the screw dislocations decreases strongly when the temperature decreases below a critical temperature. For niobium, this critical temperature is close to room temperature for slow ($\dot{\epsilon} \sim 10^{-4}/s$) strain rates but is higher than room temperature for fast ($\dot{\epsilon} \sim 10^{-2}/s$) strain rates [20]. In the low-temperature regime, the edge dislocations are more mobile than the screw dislocations, and dislocation multiplication by bowing is difficult. Above the critical temperature, both screw and non screw segments have similar mobilities, σ^* is small, and the deformation behavior resembles that of fcc metals. Figure 4.15 shows schematically the temperature dependence of the deformation behavior of bcc metals. Thus at the low strain rates fatigue occurs by a ductile failure mechanism due to the similar mobilities of both screw and edge dislocations. At high strain rates, the screw dislocations are pinned and the flow stress is high thus promoting failure by brittle cleavage mechanisms.

Previous work on the effects of temperature and strain rate on the cyclic failure of bcc metals has confirmed the existence of a ductile-brittle transition [4-8]; where cyclic cleavage was observed at the high strain rates while ductile failure occurred at the low strain rates. Cyclic cleavage is associated with a brittle cyclic cleavage crack growth per fatigue cycle; it is thus a crystallographic form of crack advance controlled by dislocation motion but associated with a cleavage plane and not a slip plane. An increased contribution from cleavage to the crack advance process clearly enhances the crack-growth rates under cyclic loading and it is possible that at the highest growth rates monotonic "burst" cleavage phenomena are the predominant mode of failure [21]. The cyclic cleavage growth occurs by a brittle "striation-jogged river" process across the cleavage plane. The striations tend to be an integral part of the process but may exist independently and be perpendicular to cleavage rivers in the absence of jogs. Since such processes are fairly small-scale, cyclic cleavage is often difficult to observe even though it may exist. Figure 4.16 shows evidence of cyclic cleavage in the Nb particle in the equiaxed composite tested at the high strain rate. Such phenomena are not well understood.

The current results demonstrate that composite microstructures developed for superior toughness may not necessarily offer optimum resistance to fatigue. Similar to behavior reported previously for γ -TiAl reinforced with TiNb, under cyclic loading the



Fig. 4.16. SEM micrograph of a Nb particle in the equiaxed Nb/Nb₃Al composite under cyclic loading at 25 Hz and room temperature, showing evidence of "cyclic cleavage". Note the presence of striations perpendicular to the crack-growth direction (direction of arrow) and also perpendicular to the cleavage river markings.

effect of ductile-phase toughening can be diminished due to premature fatigue failure of the reinforcing ductile phase. However, the inclusion of such reinforcements still provides for increased crack growth resistance as compared to unreinforced Nb_3Al .

4.7 Conclusions

1. Reinforcement of monolithic Nb_3Al with Nb gives rise to approximately a six-fold increase in fracture toughness; the ductile-phase toughening results primarily from crack bridging by unbroken Nb particles in the wake of the crack tip, and from plastic deformation and ultimately ductile rupture of the Nb phase. Additional toughening results from microcracking of the matrix ahead of the crack tip and crack deflection. K_{Ic} of the equiaxed and the lamellar composites are $\sim 6.5 \text{ MPa}\sqrt{\text{m}}$ and $\sim 5.5 \text{ MPa}\sqrt{\text{m}}$ respectively compared to a $K_{Ic} \sim 1.1 \text{ MPa}\sqrt{\text{m}}$ for monolithic Nb_3Al .
2. Under cyclic loading conditions, premature failure of the Nb particles effectively decreases ductile-phase toughening by crack bridging. The Nb particles fail by a cleavage-type mechanism (cyclic cleavage) at high frequencies and at high ΔK levels, as opposed to the ductile rupture under monotonic loading. Fatigue cracks propagate at stress intensities of $2\text{-}3 \text{ MPa}\sqrt{\text{m}}$ far below the stress intensities required to propagate cracks ($5\text{-}6 \text{ MPa}\sqrt{\text{m}}$) under monotonic loading.
3. The change in failure mechanism observed from a ductile rupture failure under monotonic loading to a brittle cleavage failure under high frequency fatigue loading is a result of the strain rate sensitivity of the ductile Nb particles. Tests conducted at various strain rates under cyclic loading indicate a fracture-mode transition from ductile striations at low frequencies to cyclic cleavage at high frequencies.

4.8 References

1. L. Murugesh, K. T. Venkateswara Rao, L. C. DeJonghe and R. O. Ritchie, in *Developments in Ceramic and Metal-Matrix Composites*, edited by K. Upadhya, p. 65, TMS, Warrendale, PA (1991).
2. L. Murugesh, K. T. Venkateswara Rao, L. C. DeJonghe and R. O. Ritchie, *Mat. Res. Soc. Symp. Proc.* **273**, 433 (1992).
3. R. O. Ritchie, *Int. Met. Rev.* **20**, 205 (1979).
4. P. Neumann, H. Vehoff and H. Fuhlrott, in *Fracture 1977*, Vol. 2, p. 1313. Fourth Int. Conf. Fract., Waterloo, Ontario, Canada (1977).
5. W. W. Gerberich, N. R. Moody and K. Jatavallabhula, *Scripta Metall.* **14**, 113 (1980).
6. N. R. Moody and W. W. Gerberich, *Mater. Sci. Eng.* **41**, 271 (1979).
7. W. W. Gerberich and K. Jatavallabhula, *Acta Metall.* **31**, 241 (1983).
8. J. I. Dickson, I. Uribe-Perez and E. Geckinli, *Mater. Sci. Eng.* **60**, 231 (1983).
9. M. F. Ashby, F. J. Blunt and M. Bannister, *Acta Metall.* **37**, 1847 (1989).
10. H.E. Dève, A.G. Evans, G.R. Odette, R. Mehrabian, M.L. Emiliani and R.J. Hecht, *Acta Metall.* **38**, 1491 (1990).
11. G.R. Odette, H.E. Dève, C.K. Elliott, A. Hasigawa and G.E. Lucas, in *Interfaces in Ceramic Metal Composites*, edited by R.J. Arsenault, R.Y. Lin, G.P. Martins and S.G. Fishman, p. 443, TMS-AIME, Warrendale, PA (1990).
12. H.C. Cao, B.J. Dalgleish, H.E. Dève, C. Elliott, A.G. Evans, R. Mehrabian and G.R. Odette, *Acta Metall.* **37**, 2969 (1989).
13. D. Tabor, *The Hardness of Metals*, Oxford University Press, New York (1951).
14. P. A. Mataga, *Acta Metall.* **37**, 3349 (1989).
15. S. Fariabi, A. L. W. Collins and K. Salama, *Metall. Trans. A* **14A**, 701 (1983).
16. M. M. Farahani, F. Attia and K. Salama, *Metall. Trans. A* **12A**, 631 (1981).
17. D. W. Chung and N. S. Stoloff, *Metall. Trans. A* **9A**, 1387 (1978).

18. H. Mughrabi, K. Herz and X. Stark, *Int. J. Fract.* **17**, 193 (1981).
19. F. Ackermann, H. Mughrabi and A. Seeger, *Acta Metall.* **31**, 1353 (1983).
20. J. M. Meininger and J. C. Gibeling, *Metall. Trans. A* **23**, 3077 (1992).

5. DUCTILE-PHASE TOUGHENING IN MoSi_2/Nb COMPOSITES

(In collaboration with Dr. W. O. Soboyejo, McDonnell-Douglas Research Labs)

5.1 Introduction

Many of the toughened intermetallic and ceramic composites under current active study are being developed as potential high-temperature structural materials for the next generation of aerospace propulsion systems [1-13]. Molybdenum disilicide (MoSi_2) is a promising candidate for such applications due to its high melting point (2050°C), moderate density (6.31 g/cm^3) and excellent oxidation resistance, resulting from the formation of a protective glassy- SiO_2 film at temperatures above 600°C .³ In fact, for this reason, silicides such as MoSi_2 are widely used as oxidation-resistant coatings on refractory-metal components [15]. However, like most intermetallics, the structural use of MoSi_2 is severely limited by problems of low ductility, toughness and impact strength at room temperature (the ductile-to-brittle transition temperature is between $900\text{--}1000^\circ\text{C}$); in addition, its high-temperature strength is relatively low [14-17]. Accordingly, it is a model material system for reinforcement with second-phase particles to achieve optimal strength-toughness combinations at ambient and elevated temperatures.

Limited studies to date on MoSi_2 -based intermetallic-matrix composites reveal only modest improvements in toughness with the addition of second-phase reinforcements [9,18-25]. For example, TiC particulate reinforcements show little effect [22], whereas crack deflection and crack bridging promoted by the inclusion of 20 vol.% SiC whiskers only raises the toughness of MoSi_2 from ~ 5.3 to $8.2 \text{ MPa}\sqrt{\text{m}}$ [21]. CaO-partially-stabilized-zirconia (Ca-PSZ) reinforcements have been shown to provide a larger degree of toughening (by a factor of $2\frac{1}{2}$), presumably from the monoclinic-to-tetragonal phase transformation in ZrO_2 [24]. The use of ductile-phase toughening, on the other hand, has received only very limited attention. Results on Y_2O_3 -coated and uncoated Nb/ MoSi_2 composites [9] indicate a larger rupture energy for the composites, although similar to the other studies, cyclic fatigue data on the MoSi_2 system are non-existent. It is thus the objective of the present paper to examine the (monotonic) fracture toughness and (cyclic) fatigue-crack propagation behavior in a MoSi_2 intermetallic-matrix composite reinforced with 20 vol.% of ductile Nb spheres, with emphasis on the micromechanisms associated with crack advance.

³Between $300\text{--}600^\circ\text{C}$, MoSi_2 is prone to severe oxidation in air or oxygen-bearing atmospheres, referred to as "pest failures" [14].

5.2 Materials and Experimental Procedures

The Nb/MoSi₂ composite was processed at the McDonnell Douglas Research Laboratories. MoSi₂ powder (99.5%, -325 mesh), produced by Cerac, Milwaukee, WI, was mixed with a nominal 20 vol.% of spherical niobium particles (-35 to +80 mesh or -500 to +177 μm), manufactured by Nuclear Metals. The MoSi₂ powder was loaded into a Nb can, degassed and sealed by electron beam welding. The can was then hot isostatically pressed (HIPed) at 1700°C for 1 h under 200 MPa argon pressure. The resulting composite microstructure, shown in Figs. 5.1a and b, consisted of ~250 μm diameter Nb spheres (measured as 18.4 vol.%), randomly distributed in a fine-grained (~14 μm) MoSi₂ matrix. Considerable interfacial reaction between Nb and MoSi₂ phases was observed during consolidation resulting in a ~40 μm thick reaction layer surrounding the Nb particles (Fig. 5.1b). This layer was composed of predominantly Nb₅Si₃ and (Mo,Nb)₅Si₃, as shown by the energy dispersive X-ray spectroscopy results in Figure 5.2, proportions varied with distance from the interface with the Nb₅Si₃ phase being closer to the Nb. Porosity was inherent in the MoSi₂ matrix at grain boundaries and within grains; pull-out of Mo₅Si₃ and SiO₂ second-phase particles at grain boundaries further contributed to voids in the matrix. In contrast, the reaction layer and Nb particles exhibited a fully dense structure, although very fine features resembling microcracks were evident within the Nb spheres. Room temperature physical and mechanical properties of the constituents, MoSi₂ and Nb, are listed in Table 5.1.

Fatigue-crack growth behavior under cyclic tension loading was examined using 25 mm-diameter, 19 mm-wide and 5 mm-thick disk-shaped compact DC(T) specimens (as per ASTM Standard E399-83), with a wedge-shaped starter notch to assist precracking. Tests were performed manually on electro-servo-hydraulic testing machines operating under displacement control, in room-temperature air (22°C and ~45% relative humidity), at a load ratio ($R = K_{min}/K_{max}$) of 0.1 and a frequency of 25 Hz (sine wave). Growth rates over the range $\sim 10^{-10}$ to 10^{-6} m/cycle were obtained under both K-decreasing and K-increasing conditions, with crack lengths continuously monitored *in situ*, to a resolution better than 5 μm, by measuring the electrical resistance of thin metallic foils bonded onto the specimen surface. Techniques were similar to those developed for cyclic fatigue testing of ceramics [28,29]. Results are presented in the form of crack-growth rates per cycle (da/dN) as a function of the applied stress-intensity range, $\Delta K (= K_{max} - K_{min})$.

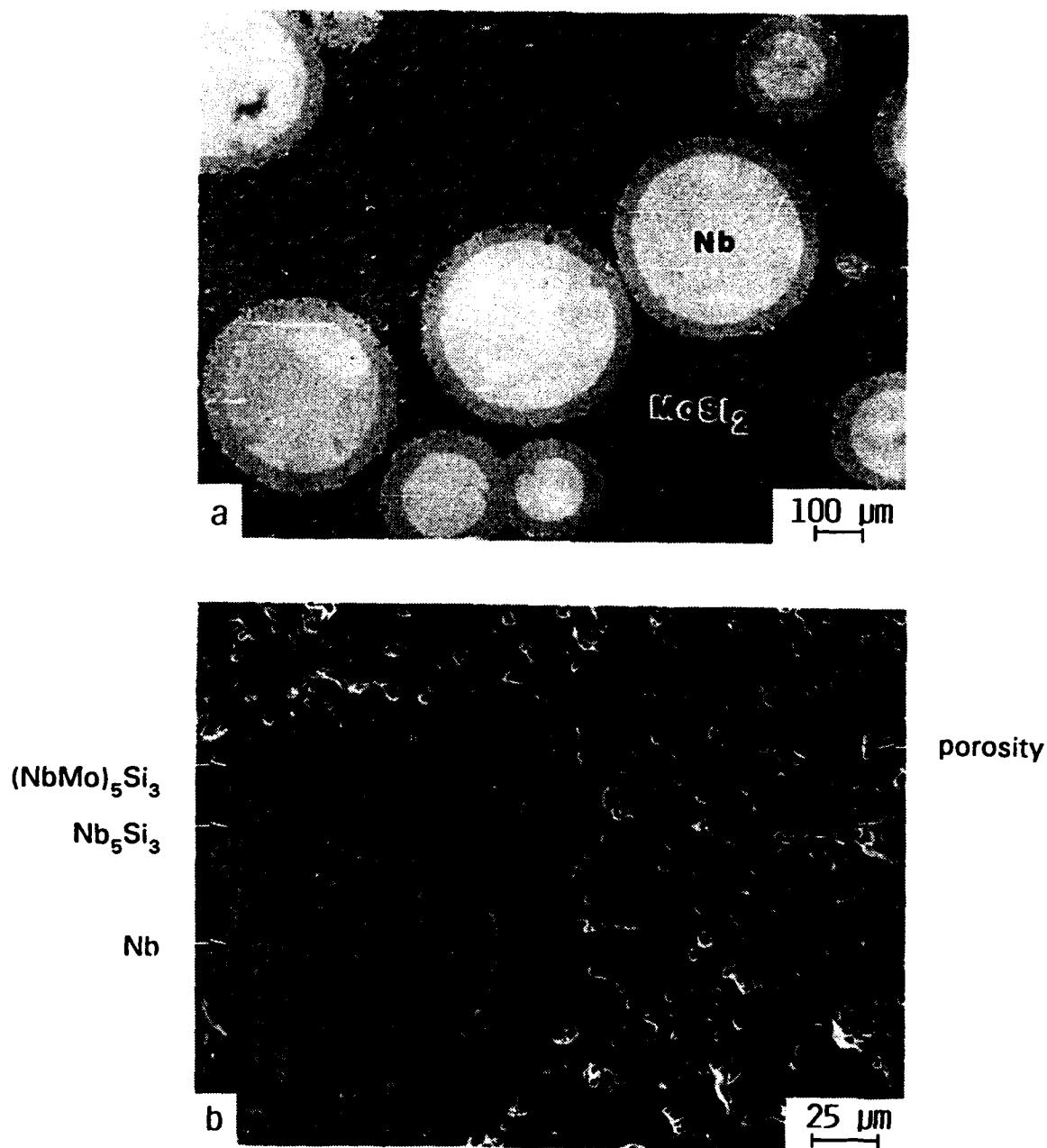


Fig. 5.1: Scanning electron microscope (SEM) images of a) the microstructure and b) the Nb/reaction-layer/matrix interface in hot-isostatically pressed Nb/MoSi₂ intermetallic-matrix composite.

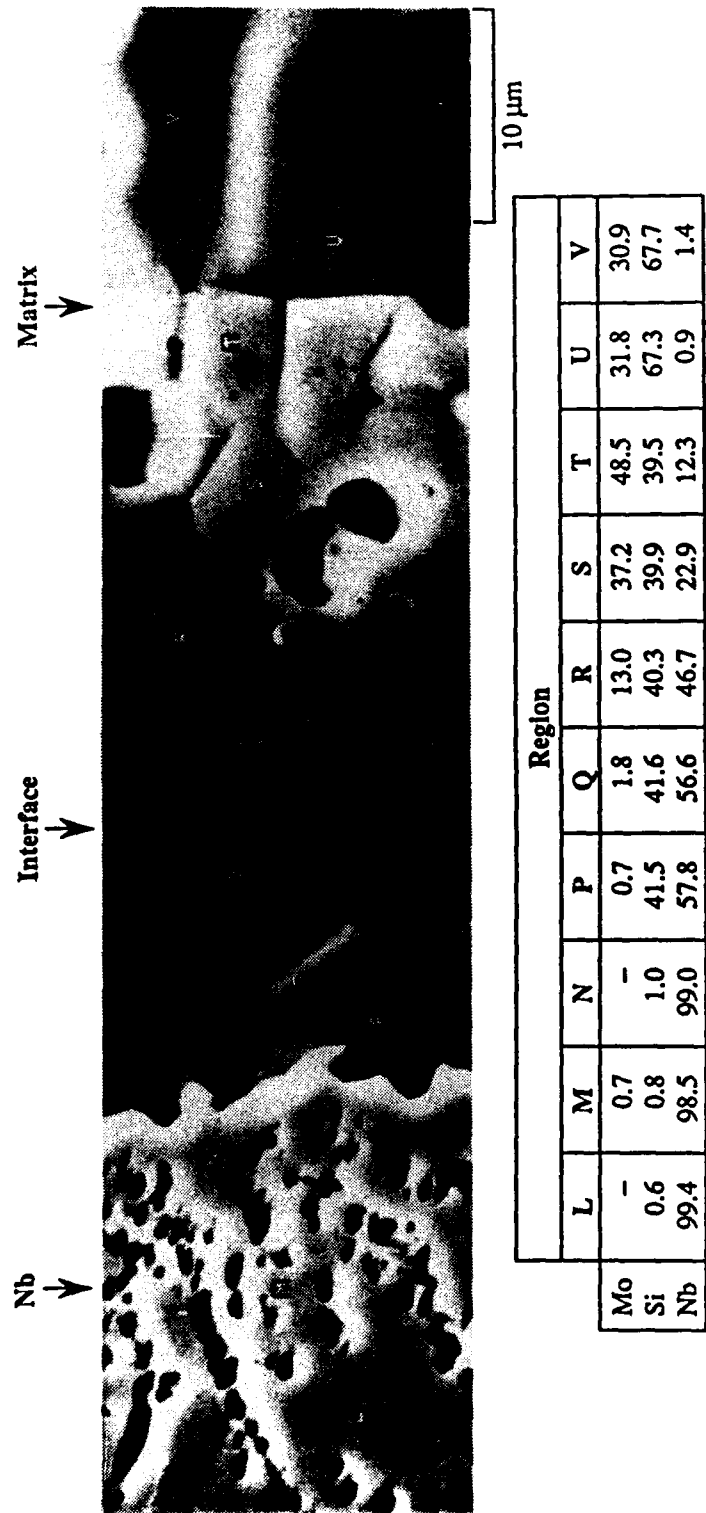


Fig 5.2: Energy dispersive X-ray spectroscopy of the interface between the Nb particles and MoSi₂ matrix. All compositions are given in atomic pct.

**TABLE 5.1: Physical and Mechanical Properties of MoSi₂
and Nb at Room Temperature[†]**

Property	MoSi ₂	Nb
Density (g/cm ³)	5.60	8.57
Crystal structure	bct (ordered C11 _b)	bcc
Melting point (°C)	2050	2468
Coefficient of Thermal Expansion, α		
at 20°C (μm/m.°C)	6.8	7.3
at 1800°C (μm/m.°C)	10.0	9.6
Elastic modulus, E (GPa)	380	103
Poisson's ratio, ν	0.17	0.38
Tensile Strength at 20°C (MPa)	325	200 (annealed)
Yield Strength at 1200°C (MPa)	325	55
Ductile-to-brittle transition temperature (°C)	~925	~450

[†]Compiled from Refs. 14-27.

Corresponding fracture-toughness behavior was evaluated by subsequently monotonically loading the fatigue-cracked samples to failure in order to determine resistance curves (R-curves), characterized by the crack-growth resistance, K_{Rc} , as a function of crack extension Δa . Results were again obtained in controlled room temperature air, with crack lengths continuously monitored using the bonded metal foils and a high-resolution optical telescope equipped with a video camera. Fracture surfaces and metallographically polished sections of the crack paths were examined in the scanning electron microscope (SEM).

5.2 Results

5.2.1 Fracture Toughness

Measurements of fracture-toughness values indicate only a modest degree of toughening in MoSi₂ from the inclusion of 20 vol.% Nb; compared to a K_{Ic} value of ~4.2 MPa√m for monolithic MoSi₂, the toughness of the composite is 5.2 MPa√m, a mere ~24% higher. Crack initiation in both the monolithic and composite MoSi₂ was coincident with instability, with no evidence of increasing crack-growth resistance with crack extension, i.e., R-curve behavior.

Consistent with this behavior, metallographic observations show that interactions between the crack and the ductile-Nb particles provide minimal impedance to crack advance (Fig. 5.3). First, it is apparent that cracking is primarily confined to the matrix and the reaction layer interface separating Nb and MoSi_2 . Of the ~18 vol.% of Nb particles in the microstructure, a mere ~3% are actually fractured; the rest fail along the reaction layer interface. In fact, cracks tend to circumvent the Nb particles by opting for trajectories between or around particles in the $(\text{Mo,Nb})_3\text{Si}_3$ product phase, i.e., in the reaction layer (Fig. 5.3d). Accordingly, the resulting fracture surfaces are covered with dimples and mounds left by Nb spheres that decohered or pulled out from the matrix (Fig. 5.4a); correspondingly, particle and dimple surfaces are less porous compared to the matrix indicative of failure in the (Mo,Nb) silicide-product layer (Fig. 5.4b). Second, the Nb particles that are traversed by the crack show no evidence of plastic stretching or rupture which would provide a contribution to the toughness. Third, in contrast to Nb reinforcements in γ -TiAl composites [7], there is no evidence of crack blunting, or excessive plastic deformation, in the Nb phase; cracks appear to remain sharp in both the matrix and Nb spheres (Fig. 5.3). Accordingly, the Nb-particle fracture surfaces are characterized by complete transgranular cleavage on a single plane (Figs. 5.4c,d), although a few exhibit brittle-shear type cracking; matrix failures are similarly brittle with a mixed intergranular/transgranular fracture mode (Fig. 5.5).

5.2.2 *Fatigue-Crack Propagation*

The variation in (cyclic) fatigue-crack growth rates with applied ΔK for the Nb/ MoSi_2 composite, shown in Figure 5.6, illustrates that cracks can grow subcritically in this material at stress intensities well below K_{Ic} . However, similar to many ceramics [e.g., refs. 28-30], growth rates are strongly dependent upon ΔK and display a non-sigmoidal growth-rate curve with no apparent indication of a well defined fatigue threshold. Expressed in terms of a simple Paris power-law da/dN vs. ΔK relationship, the exponent on ΔK is ~14, compared to values between 2 and 4 typically observed for metals and between 15 and 50 for ceramics [30,31]. Although precracking was achieved in compression, stable fatigue crack growth was not observed in monolithic MoSi_2 under tension-tension loading at ΔK levels for which K_{max} was less than K_{Ic} .

Crack-particle interactions in the Nb/ MoSi_2 composite under cyclic loading are quite similar to those observed under monotonic loading. In general, fatigue cracks still

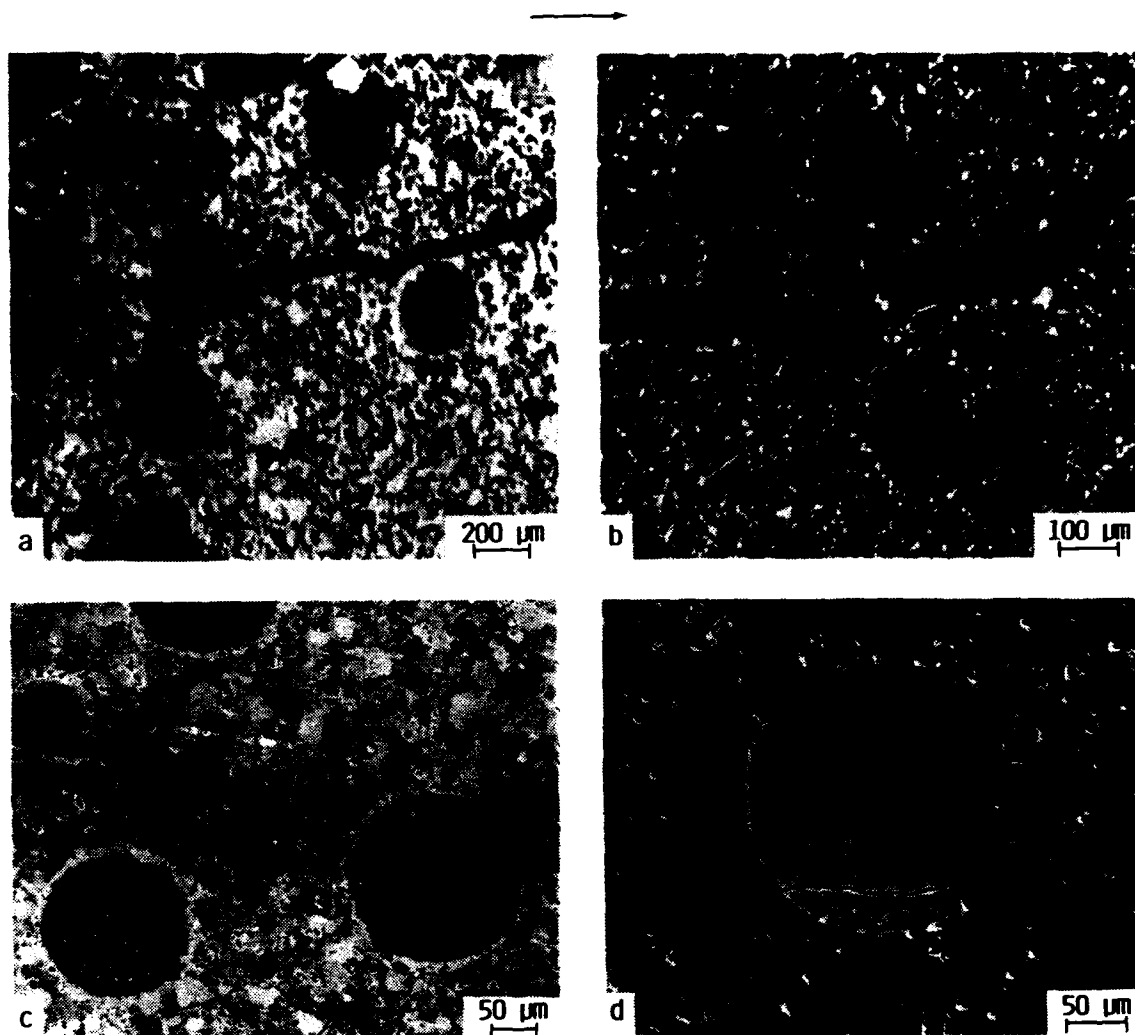


Fig. 5.3: a,b) *In situ* optical telescopic and c,d) SEM images of crack-path morphologies in the Nb/MoSi₂ composite, showing crack propagation a) around and b) between the Nb spheres. Crack-path trajectories around the Nb generally occur in the (NbMo)₅Si₃ layer close to matrix/reaction-layer interface. Features are similar under monotonic and cyclic loading. Arrow indicates direction of crack growth.

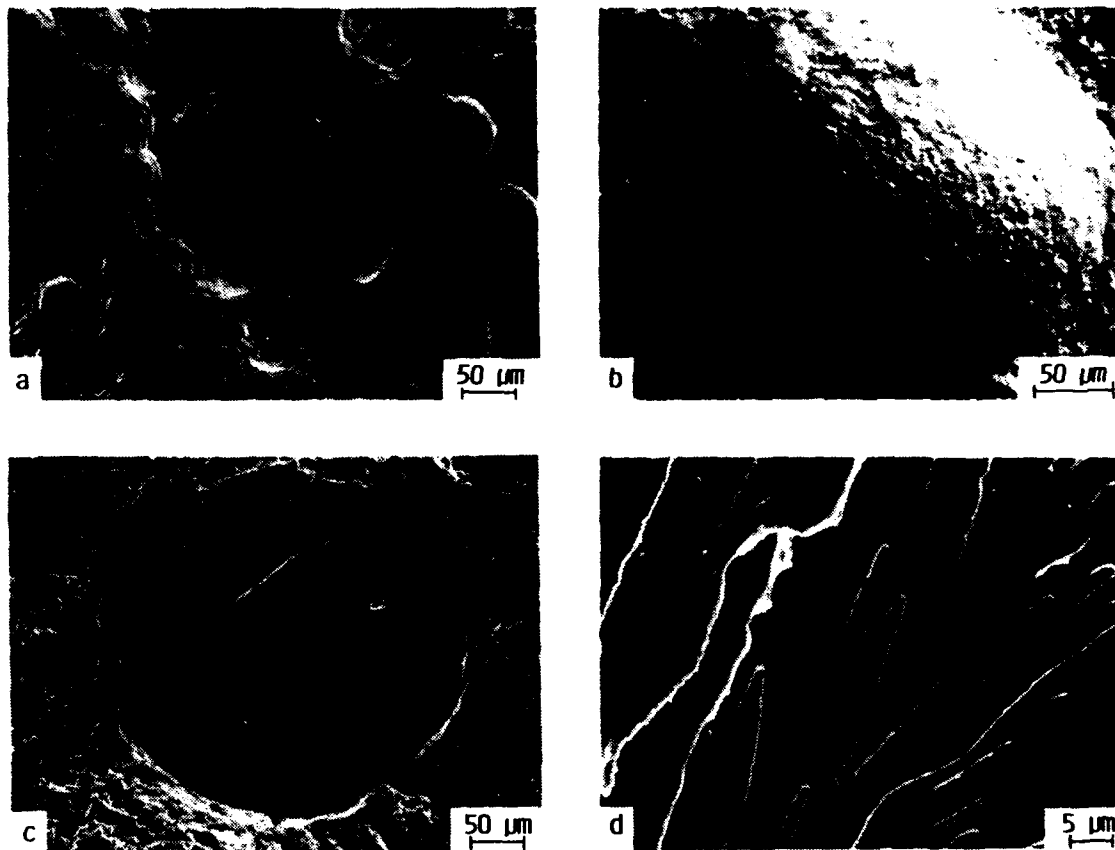


Fig. 5.4: SEM Micrographs of fracture surfaces in Nb/MoSi₂ composite under monotonic loading, showing a,b) predominantly dimples and mounds caused by particle pull-out, and c,d) transgranular cleavage of the few Nb particles that intercept the crack (at a,c) low and b,d) high magnifications). Arrow indicates general direction of crack advance.

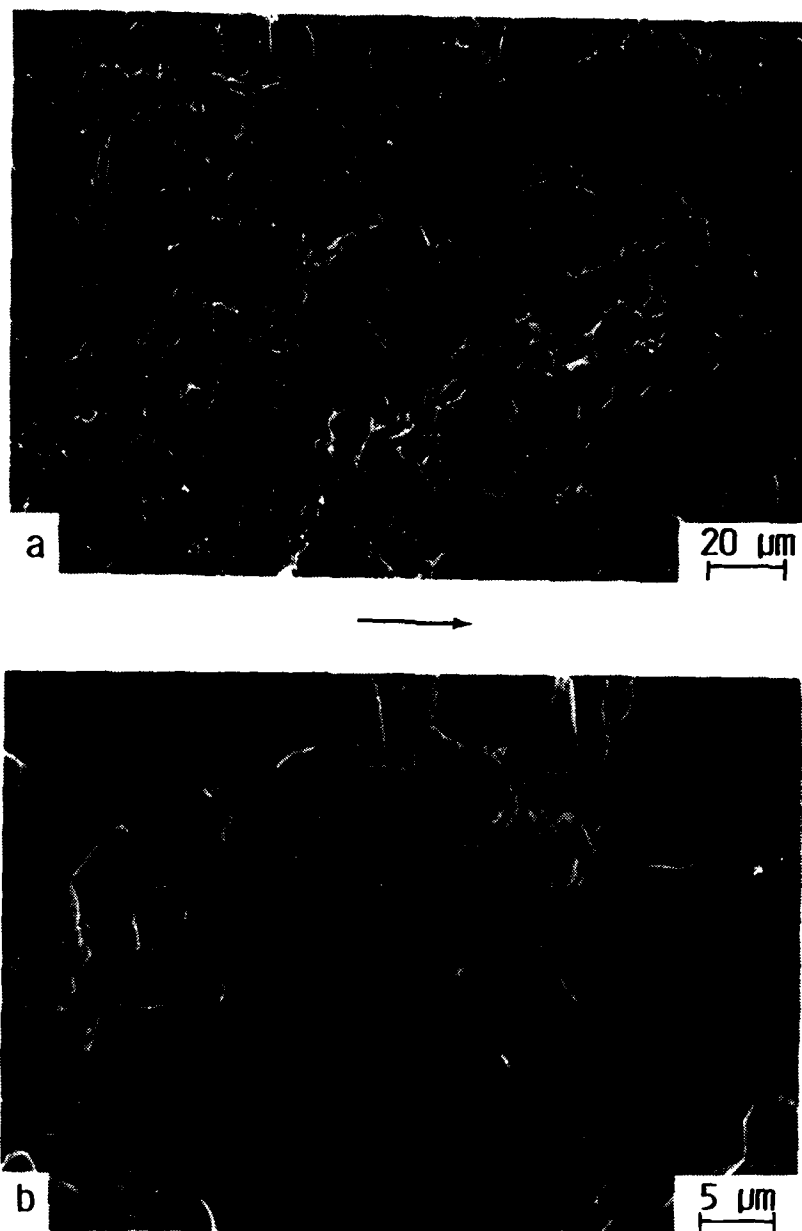
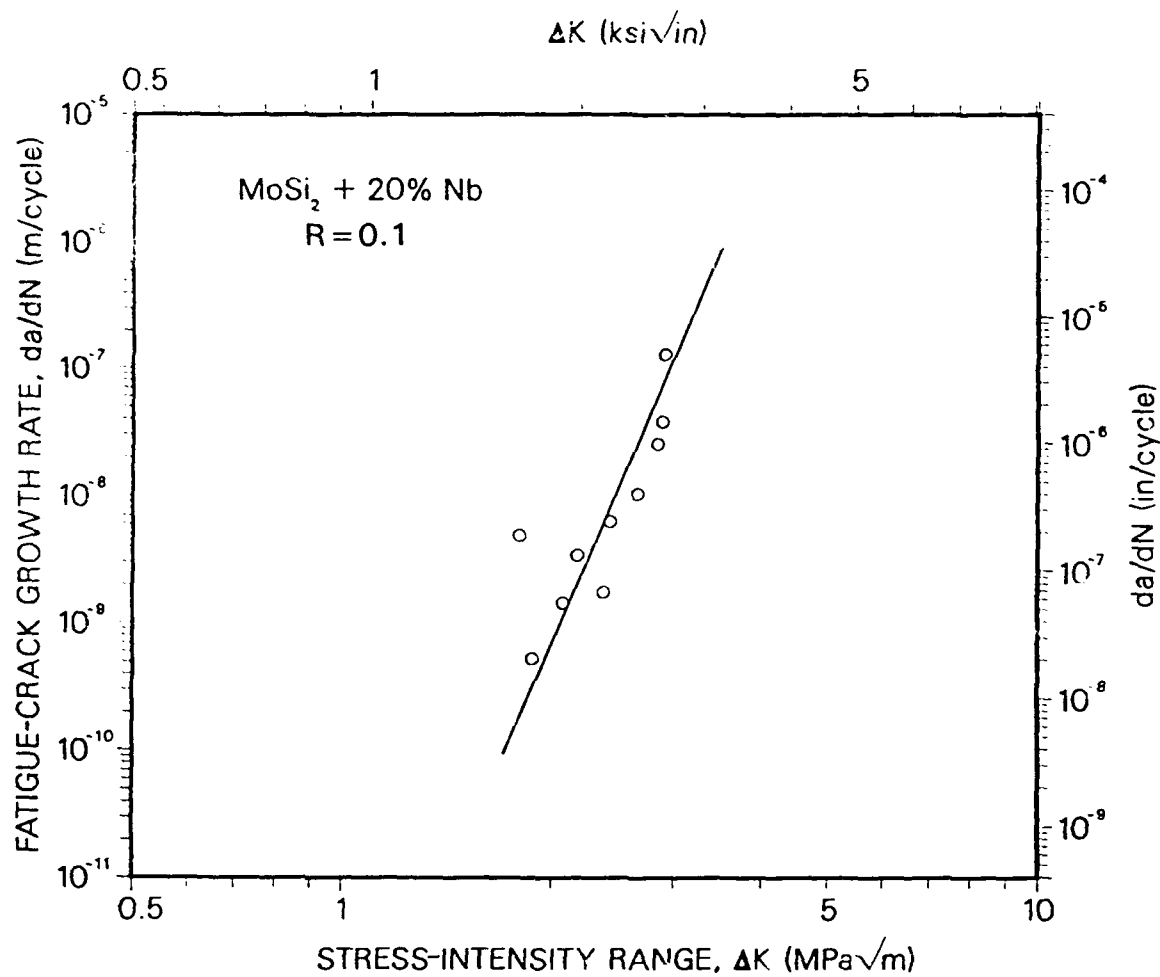


Fig. 5.5: a) Low and b) high-magnification SEM micrographs of fracture in Nb/MoSi₂ under monotonic loading, showing transgranular plus intergranular cracking in the porous MoSi₂ matrix. Features are nominally similar under monotonic and cyclic loading. Arrow indicates direction of crack growth.



XBL 917-1403

Fig. 5.6: Variation in cyclic fatigue-crack propagation rates, da/dN , as a function of the applied stress-intensity range, ΔK , in the Nb/MoSi₂ composite, in controlled room temperature air at a load ratio R of 0.1.

tend to avoid the ductile Nb reinforcements, such that "hill and trough" fracture surfaces are again observed (Fig. 5.3). Cracking in the MoSi_2 matrix occurs by brittle intergranular plus transgranular fracture (Fig. 5.5), similar to static failures; however, the mechanism of failure in the few Nb particles (~3 vol.%) that are intercepted by the crack is predominantly by multi-faceted, brittle-transgranular shear (Fig. 5.7), rather than the transgranular cleavage seen under monotonic loads.

5.3 Discussion

5.3.1 Crack/Particle Interactions

The present results clearly demonstrate that the reinforcement of brittle solids by a ductile phase can only induce marked toughening provided the crack truly intersects the ductile phase. In the present Nb/ MoSi_2 composite, where the crack essentially avoids the ductile phase by debonding within the reaction layer interface, no significant toughening is observed. This can result from several factors, including i) residual thermal stresses, ii) elastic mismatch stresses at the crack tip, iii) properties of the particle/matrix interface, and iv) the shape of the reinforcement phase [1-3,9,32-35]. The effect of these factors is discussed in turn below.

Residual thermal stresses: Assuming no stress relaxation during cooling, the maximum value of the hydrostatic (thermal mismatch) stress, σ_{therm} , arising from a temperature change ΔT can be estimated from the differential linear thermal-expansion coefficient between the matrix and the ductile phase ($\Delta\alpha = \alpha_m - \alpha_p$) [32]:

$$\sigma_{\text{therm}} = \Delta\alpha\Delta T \left[\frac{1 + \nu_m}{2E_m + \left(\frac{1 - 2\nu_p}{E_p} \right)} \right]^{-1} \quad (2)$$

where E_m , E_p , ν_m and ν_p are the Young's moduli and Poisson's ratios of the matrix and the particle, respectively. The particles are in compression where $\alpha_m > \alpha_p$ and in tension where $\alpha_p > \alpha_m$. As α_{MoSi_2} and α_{Nb} are closely matched, the value of σ_{therm} is relatively small; using average values for α in Table 5.1, thermal stresses resulting from processing are estimated to be ~44 MPa (compression) in the particle, insufficient to cause interfacial cracking in the composite.

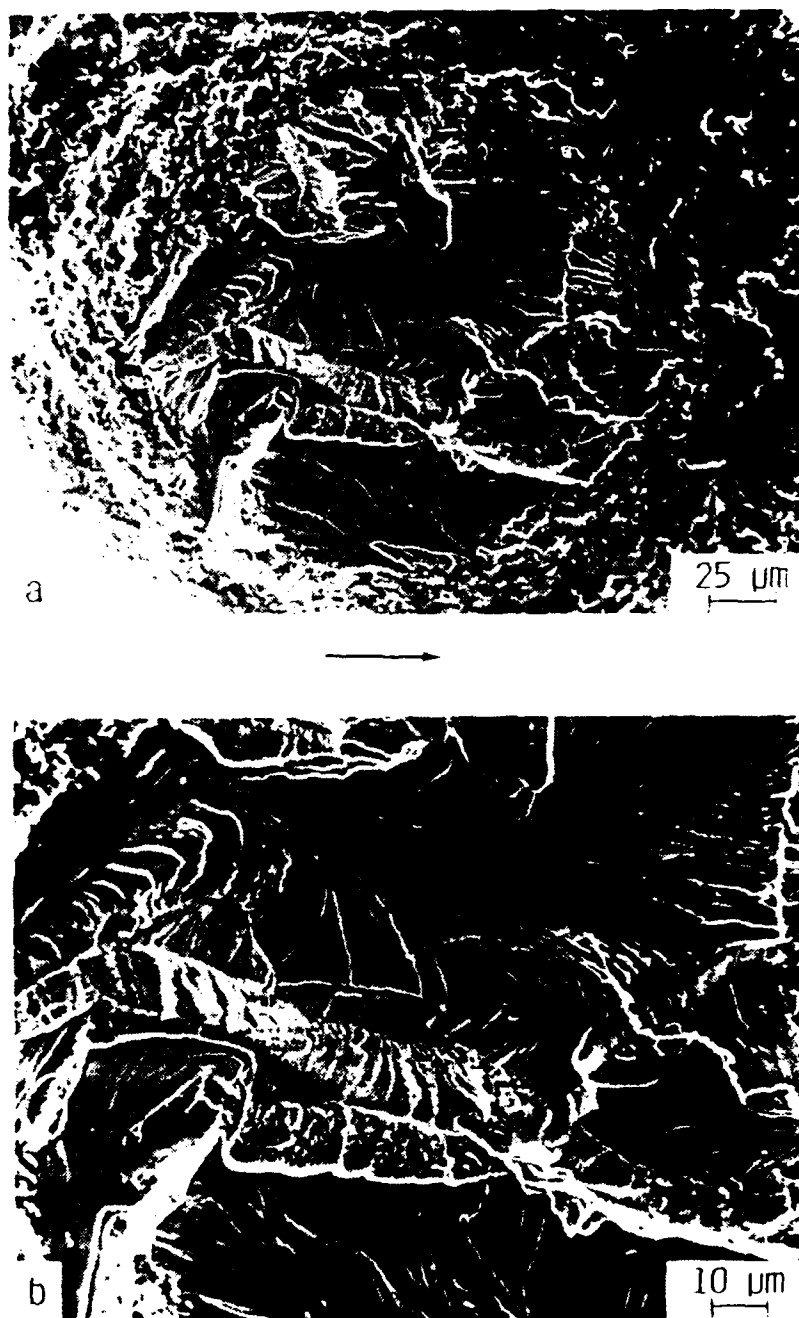


Fig. 5.7: a) Low and b) high-magnification SEM micrographs of fracture in Nb/MoSi₂ under cyclic loading, showing brittle-shear cracking in the few Nb particles that are intercepted by the crack. Arrow indicates direction of crack advance.

Elastic mismatch stresses: Crack-path selection can be influenced by interactions between the asymptotic stress field of the crack tip in the matrix and the elastic-stress concentration around a spherical particle of different stiffness [33,35]. In composite systems, where $E_p > E_m$ cracks tend to deflect to high stress concentration sites, i.e., poles of particles, thus completely avoiding the particle. Conversely, where $E_m > E_p$, as is the case with Nb/MoSi₂, cracks are expected to be attracted by soft ductile particles in the stiffer matrix. Since this is not observed, it is presumed that interfacial properties are primarily responsible for the crack bowing around Nb particles, as discussed below.

Particle/matrix interface properties: As cracking proceeds in the reaction layer interface, the Nb particle can be effectively considered to be weakly bonded to MoSi₂.^{*} From interfacial mechanics analysis [36], a weak interface in composites combined with a large elastic mismatch between matrix and particle increasingly favors crack paths along the interface over crack intersection with the particle (and hence particle rupture). For a mismatch of $\delta \sim 0.57$ between Nb and MoSi₂, taken as [36]:

$$\delta = \frac{\left(\frac{E_m}{1 - \nu_m^2} \right) - \left(\frac{E_p}{1 - \nu_p^2} \right)}{\left(\frac{E_m}{1 - \nu_m^2} \right) + \left(\frac{E_p}{1 - \nu_p^2} \right)}, \quad (3)$$

the criterion for debonding along the interface is given as [35]:

$$\frac{G_i}{G_p} < 0.4, \quad (4)$$

where G_i and G_p refer to the interfacial and particle toughnesses, respectively. The corresponding criterion for an interfacial crack between two materials with similar moduli is $G_i/G_p < 0.25$. In other words, interfacial decohesion occurs in composites with progressively stronger interfaces with increasing elastic mismatch. The requirement in Eq. 4 is readily satisfied for the Nb/MoSi₂ composite, which has an interfacial toughness, G_i of

^{*} A more precise treatment of this problem should consider the properties of a Nb/Nb₅Si₃/(Mo,Nb)₅Si₃/MoSi₂ layered structure. The varying composition of the reaction layer interface and the absence of elastic properties for Mo, Nb silicides precludes solution to this problem.

~50-60 J/m² (which is on the order of G_{MoSi_2} [9,26,27]) compared to G_{Nb} of ~200-500 J/m² [9].

In addition to poor interfacial resistance, the elastic properties of the ~40 μm -thick reaction layer can influence the crack path; a compliant product phase tends to negate the toughening capability of the particle and weakens the composite [35]. The application of stiffer surface coatings to the Nb particles, that are capable of retarding MoSi₂/Nb interfacial reaction kinetics and layer thickness during processing, may therefore be more effective in utilizing the ductility of Nb particles.

Reinforcement-phase shape: Although weak matrix/reinforcement-phase bonding and resultant debonding at the interface is generally desirable in the toughening of brittle materials, it is vital that the dispersed reinforcement phase has a large aspect ratio, i.e., is in the form of aligned fibers, whiskers or laminates. This follows because debonding at the interface lessens the probability of failure of the reinforcement phase, thereby promoting crack bridging. With spherical reinforcements, however, this approach appears counterproductive; owing to the low aspect ratio of spheres, the initial debonding stabilizes crack propagation *around* the particle in the interfacial region, thereby limiting the toughening contribution of ductile particles to mere crack deflection.

The moderate improvement in toughness of Nb/MoSi₂ compared to pure MoSi₂ is consistent with the extent of shielding from crack deflection by second-phase Nb particles. Upon intercepting the Nb particle, the crack tilts away from the plane of principal stress in the particle/matrix interface; further crack advance occurs by crack front twisting as the crack circumvents the spherical particle. Both the (in plane) tilt and (out of plane) twist processes contribute to crack deflection toughening. Following the approach of Bilby et al. [37], the local Mode I, Mode II and Mode III stress-intensities k_1 , k_2 and k_3 , at the tip of a deflected crack can be given in terms of the far-field stress-intensities for the linear crack K_I and K_{II} as:

$$\begin{aligned} k_1' &= a_{11}(\theta) K_I + a_{12}(\theta) K_{II} \\ k_2' &= a_{21}(\theta) K_I + a_{22}(\theta) K_{II} \end{aligned} \quad (5)$$

where θ is the tilt angle, $a_{ij}(\theta)$ refers to the angular functions documented in ref. [38] and superscript t denotes the reduction in local driving force from tilting. The corresponding relations for k_1^T and k_3^T , due to crack twisting at an angle ϕ , may be given as [39]:

$$\begin{aligned} k_1^T &= b_{11}(\phi) k_1' + b_{12}(\phi) k_2' \\ k_3^T &= b_{31}(\phi) k_1' + b_{32}(\phi) k_2' \end{aligned} \quad (6)$$

angular functions $b_{ij}(\phi)$ are documented in ref. [39]. The effective near-tip driving force, in terms of the energy-release rate (fracture energy) G or k_{eff} , can then be considered as:

$$\begin{aligned} EG &= k_1^2(1 - \nu^2) + k_2^2(1 - \nu^2) + k_3^2(1 + \nu) \\ k_{eff} &= \sqrt{EG} \end{aligned} \quad (7)$$

where E and ν are the Young's modulus and Poisson's ratio of the material. Using these relations for the local driving force and incorporating crack-particle interception probabilistics in two-phase systems (at all possible tilt and twist angles), with well defined second-phase morphologies, toughening increment due to spherical reinforcements from pure tilt-induced deflection may be given as [39]:

$$G_c = (1 + 0.87V_f) G_{cm} \quad (8)$$

where G_c and G_{cm} are the fracture energies of the composite and matrix, respectively, and V_f is the volume fraction; including twist further enhances the toughening ratio. For example, crack tilting induced by the addition of 20 vol.% spheres based on Eq. 11 yields $G_c/G_{cm} \sim 1.17$; crack-twist contributions from uniformly distributed spheres elevate this ratio to ~ 1.3 . And moreover, a distributed spacing (Δ) between these particles (of radius r), with the standard deviation $\sigma > 0.4(\Delta/r)$, can further increase toughness to $\sim 1.6 G_{cm}$ [39]. Expressed in terms of stress-intensities, $k_{eff} \sim 1.26 K_{cm}$ (or $/1.6 G_{cm}$) or in other words the near-tip stress intensity is reduced $\sim 30\%$ by crack deflection.

In the present case, measured local crack-tilt and -twist angles range between 25-90°; particles are distributed with a mean spacing of $\sim 400 \mu m$ with a standard deviation of $\sim 140 \mu m$ suggesting that particle-spacing effects are prominent. Measured increase in K_{Ic} of the composite with respect to the monolithic $MoSi_2$ is ~ 1.3 in good agreement with the above predictions. Higher rupture energies measured in other studies [9] are associated with stretching of the Nb particles.

Apart from crack bridging considerations, the above analysis also emphasizes the need to increase the aspect ratio of reinforcing particles to significantly enhance the composite toughness from pure crack deflection considerations [39]. For example,

equivalent toughening increment, G_c/G_{cm} , for rod- and disc-shaped reinforcements with an aspect ratio of 12 is predicted to range between 3 and 4, compared to a maximum of ~ 1.8 for spheres. Thus, incorporating rod-shaped particles with high aspect ratio may be the optimal route for toughening MoSi₂-based intermetallics [21].

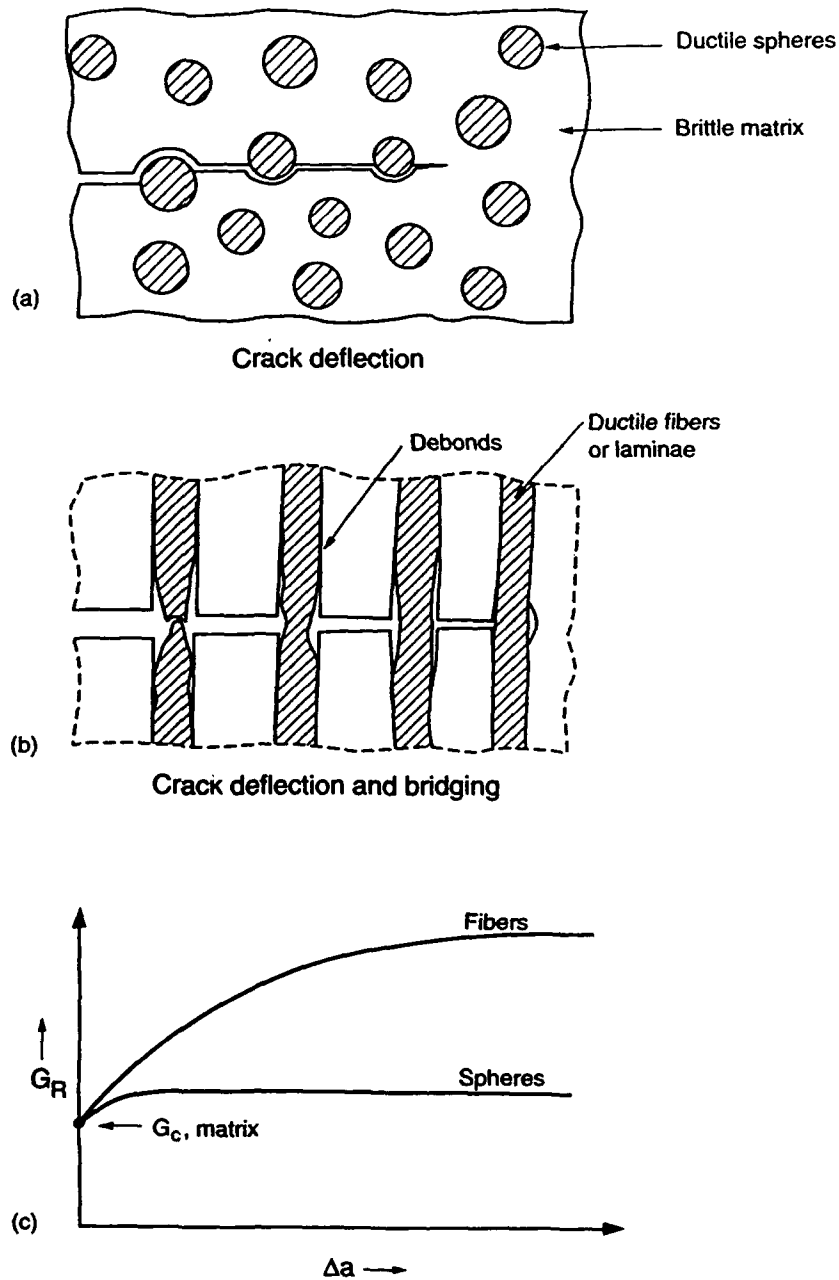
5.3.2 Brittle Fracture of Nb Particles

Other factors may be responsible for the fact that the few Nb particles that are intercepted by the crack suffer brittle cleavage fracture with little evidence of plastic deformation and do not contribute to toughening. Contamination during processing, from interstitial impurities such as carbon, hydrogen, nitrogen and oxygen, and diffusion of silicon could well embrittle the niobium particles [40]. More generally, constraint imposed on the ductile phases by large triaxial (tensile) stresses, e.g., in the vicinity of a sharp crack tip, can significantly reduce their ductility or strain-to-fracture [e.g., ref. 4]; moreover, it can trigger brittle modes of failure, especially in bcc materials that show a clear ductile-to-brittle fracture transition.

5.4 Concluding Remarks

It is clear that the absence of significant toughening in Nb/MoSi₂ results from a lack of correspondence between interfacial properties and the reinforcement shape in the microstructure. Although a weak interface, as in the present case, is often desirable in many instances for optimizing toughness of brittle materials via crack-bridging mechanisms, the spherical morphology of Nb restricts toughening since the crack circumvents the Nb phase. Moreover, Nb particle ductility is not utilized, and as a result, only a mild increase in toughness is achieved in Nb/MoSi₂ from crack deflection around spheres, with the least aspect ratio. Accordingly, both from crack-bridging and crack-deflection considerations, successful toughening in Nb/MoSi₂ composites must involve modifying the morphology of Nb into fibers, aligned whiskers, rods, pancakes or laminae and retaining the weak interface to effectively utilize crack-particle interactions, interfacial debonding and Nb particle ductility to impede crack advance (Fig. 5.8).

However, it should be noted that beneficial effects of toughening by ductile particles observed under monotonic loading may not necessarily imply better fatigue resistance under cyclic loading, as the deformation mechanisms can be quite different. In ductile-TiNb particle reinforced γ -TiAl intermetallic-matrix composites for example, the



XBL9112-7099

Fig. 5.8: Schematic illustration of crack-particle interactions in a ductile-particle toughened brittle composite for a) spherical and b) fiber reinforcement morphologies, and their influence on resistance-curve behavior.

susceptibility of TiNb particles to premature fatigue failure diminishes their ability to bridge the crack under cyclic loading [13]. Similar behavioral trends may well be expected in Nb/MoSi₂ composites, even after modifications to the microstructure to promote crack/Nb phase interactions, as Nb particles do exhibit a tendency toward fatigue failure via brittle-shear cracking under cyclic loading.

5.5 Conclusions

Based on a preliminary study on the ambient temperature fracture toughness and fatigue-crack propagation behavior in a MoSi₂ intermetallic-matrix composite reinforced with 20 vol.% Nb spheres, the following conclusions can be made:

1. Only moderate improvements (~24%) in fracture toughness K_{Ic} are observed in the Nb-reinforced MoSi₂ composite compared to the unreinforced MoSi₂, primarily due to the absence of crack-particle interactions during crack growth under monotonic loading. Resistance-curve behavior is not seen as the crack path predominantly avoids the ductile Nb particles.
2. The lack of crack-particle interactions is attributed to the formation of a weak reaction-layer interface and elastic mismatch stresses at the crack tip between Nb and MoSi₂, both of which favor interfacial debonding; moreover, the spherical morphology of Nb phase stabilizes cracking around the particle.
3. Subcritical crack growth under cyclic loading is seen in the Nb/MoSi₂ composite at stress intensities some 75-90% smaller than K_{Ic} ; similar to ceramic materials, growth rates are strongly power-law dependent on the applied stress-intensity range, with an exponent of ~14.
4. Results suggest that increasing the aspect ratio of the distributed Nb reinforcement phase (i.e., in the form of pancakes, filaments, fibers, whiskers or laminates) and preserving matrix/particle interface debonding (to reduce constraint in the Nb particles), and eliminating possible Nb-phase embrittlement (by limiting interstitial impurity contamination), are critical factors for improved crack-growth resistance in structural Nb/MoSi₂ composites.

5.6 References

1. V. D. Krstic and A. K. Khaund, in *Advances in Fracture Research, Proceedings of the Fifth Intl. Conf. on Fracture*, D. François et al. (eds.), Pergamon Press, Oxford, New York, 1577 (1980).
2. V. D. Krstic, P. S. Nicholson and R. G. Hoagland, *J. Am. Ceram. Soc.* **64**, 499 (1981).
3. V. D. Krstic, *Philos. Mag.* **48**, 695 (1983).
4. M. F. Ashby, F. J. Blunt, and M. Bannister, *Acta Metall.* **37**, 1847 (1989).
5. C. K. Elliott, G. R. Odette, G. E. Lucas, and J. W. Sheckherd, in *High-Temperature/High-Performance Composites*, F. D. Lemkey, A. G. Evans, S. G. Fishman, and J. R. Strife (eds.), MRS Symp. Proc., Vol. 120, 95 (1988).
6. H. E. Dève, A. G. Evans, G. R. Odette, R. Mehrabian, M. L. Emiliani, and R. J. Hecht, *Acta Metall. Mater.* **38**, 1491 (1990).
7. G. R. Odette, H. E. Dève, C. K. Elliott, A. Harigowa, and G. E. Lucas, in *Interfaces in Ceramic Metal Composites*, R. J. Arsenault, R. Y. Lin, G. P. Martins, and S. G. Fishman (eds.), TMS-AIME, Warrendale, PA, 443 (1990).
8. H. C. Cao, B. J. Dalgleish, H. E. Dève, C. Elliott, A. G. Evans, R. Mehrabian, and G. R. Odette, *Acta Metall.* **37**, 2969 (1989).
9. T. C. Lu, A. G. Evans, R. J. Hecht, and R. Mehrabian, *Acta Metall. Mater.* **39**, 1853 (1991).
10. B. D. Flinn, M. Rühle, and A. G. Evans, *Acta Metall.* **37**, 3001 (1989).
11. P. Hing and G. W. Groves, *J. Mater. Sci.* **7**, 427 (1972).
12. L. S. Sigl and H. E. Exner, *Metall. Trans. A* **18A**, 1299 (1986).
13. K. T. Venkateswara Rao, G. R. Odette, and R. O. Ritchie, *Acta Metall. Mater.* **40**, 353 (1992).
14. J. B. Berkowitz-Mattuck, M. Rossetti, and D. W. Lee, *Metall. Trans.* **1**, 479 (1970).
15. P. J. Meschter and D. S. Schwartz, *J. Metals* **41**:11, 52 (1989).
16. E. Fitzer, O. Rubisch, J. Schlichting, and I. Sewdas, *Sci. Ceram.* **18** (1973).

17. J. Schlichting, *High Temp.-High Pressures* **10**, 241 (1978).
18. F. D. Gac and J. J. Petrovic, *J. Am. Ceram. Soc.* **68**, C-200 (1985).
19. W. S. Gibbs, J. J. Petrovic, and R. E. Honnell, *Ceram. Eng. Sci. Proc.* **8**, 645 (1987).
20. D. H. Carter, J. J. Petrovic, R. E. Honnell, and W. S. Gibbs, *Ceram. Eng. Sci. Proc.* **10**, 1121 (1989).
21. D. H. Carter and G. F. Hurley, *J. Am. Ceram. Soc.* **70**, C-79 (1987).
22. J.-M. Yang, W. Kai, and S. M. Jeng, *Scripta Metall.* **23**, 1953 (1989).
23. J. J. Petrovic and R. E. Honnell, *J. Mat. Sci. Lett.* **9**, 1083 (1990).
24. J. J. Petrovic and R. E. Honnell, *J. Mat. Sci.* **25**, 4453 (1990).
25. J.-M. Yang and S. M. Jeng, *J. Mater. Res.* **6**, 505 (1991).
26. *Metals Handbook*, Tenth Edition, American Society for Metals International, Metals Park, OH, Vol. 2 (1990).
27. *Engineering Properties of Selected Ceramic Materials*, J. F. Lynch, C. G. Ruderer, and W. H. Duckworth (eds.), The American Ceramic Society, Columbus, OH (1966).
28. R. H. Dauskardt and R. O. Ritchie, *Closed Loop* **27**, 7 (1989).
29. R. H. Dauskardt, D. B. Marshall, and R. O. Ritchie, *J. Am. Ceram. Soc.* **73**, 893 (1990).
30. R. O. Ritchie and R. H. Dauskardt, *J. Ceram. Soc. Japan* **99**, 1047 (1991).
31. R. O. Ritchie, *Int. Met. Rev.* **20**, 205 (1979).
32. J. Selsing, *J. Am. Ceram. Soc.* **44**, 419 (1961).
33. R. W. Davidge and T. J. Green, *J. Mat. Sci.* **3**, 629 (1968).
34. A. K. Khaund, V. D. Krstic, and P. S. Nicholson, *J. Mat. Sci.* **12**, 2269 (1977).
35. J. Tirosh and A. S. Tetelman, *Int. J. Fract.* **12**, 187 (1976).
36. M.-Y. He and J. W. Hutchinson, *Int. J. Solids Struct.* **25**, 1053 (1989).

37. B. A. Bilby, G. E. Cardew, and I. C. Howard, in *Fracture 1977, Proceedings of the Fourth Intl. Conf. on Fracture*, D. M. R. Taplin (ed.), Pergamon Press, Oxford, New York, Vol. 3, 197 (1977).
38. B. Cotterell and J. R. Rice, *Int. J. Fract.* **16**, 155 (1980).
39. K. T. Faber and A. G. Evans, *Acta Metall.* **31**, 565 (1983).
40. D. W. Chung and N. S. Stoloff, *Metall. Trans. A* **9A**, 1387 (1978).

6. ACKNOWLEDGEMENTS

This work was supported by the U.S. Air Force Office of Scientific Research under Grant No. AFOSR-90-0167, with Dr. A. H. Rosenstein as program manager, Professor G. R. Odette, who collaborated on TiNb/ γ -TiAl intermetallic composites, is funded at the University of California at Santa Barbara by the Defense Advanced Projects Agency, and Dr. W. O. Soboyejo who collaborated on Nb/MoSi₂ composites was also funded by the U.S. Air Force Office of Scientific Research under Grant No. F49620-90-C-0030. Our thanks are due to Professor Odette, Professor Amit Ghosh of the University of Michigan, Dr. J. J. Petrovic at Los Alamos National Laboratory, Dr. W. O. Soboyejo, formerly of McDonnell Douglas Research Laboratories, Pratt and Whitney, and Dr. R. H. Dauskardt for supplying the intermetallic composites and for many helpful discussions.

7. PROGRAM ORGANIZATION AND PERSONNEL

The work described was performed in the Department of Materials Science and Mineral Engineering, University of California at Berkeley, under the supervision of Dr. R. O. Ritchie, Professor of Materials Science and Dr. L. C. De Jonghe, Professor of Materials Science, aided by a research engineer, graduate student research assistant and undergraduate research helpers.

- i) Professor R. O. Ritchie, Principal Investigator
(Department of Materials Science and Mineral Engineering)
- ii) Professor L. C. De Jonghe, Co-Investigator
(Department of Materials Science and Mineral Engineering)
- iii) Dr. K. T. Venkateswara Rao, Research Engineer
(Department of Materials Science and Mineral Engineering)
- iv) L. Murugesh, Graduate Student Research Assistant
(Department of Materials Science and Mineral Engineering)
- v) D. Nath, Undergraduate Engineering Aide
(Department of Mechanical Engineering)

8. PUBLICATIONS

8.1 Refereed Journals

1. K. T. Venkateswara Rao, G. R. Odette and R. O. Ritchie, "On the Contrasting Role of Ductile-Phase Reinforcements in the Fracture Toughness and Fatigue-Crack Propagation Behavior of TiNb/ γ -TiAl Intermetallic-Matrix Composites," *Acta Metallurgica et Materialia*, **40** (1992), pp. 353-361.
2. K. T. Venkateswara Rao and R. O. Ritchie, "Fatigue-Crack Propagation Resistance of Ductile TiNb-Reinforced γ -TiAl Intermetallic-Matrix Composites," *Materials Science and Engineering A*, **A153** (1992), pp. 479-485.
3. K. T. Venkateswara Rao, W. O. Soboyejo and R. O. Ritchie, "Ductile-Phase Toughening and Fatigue-Crack Growth in Nb-Reinforced Molybdenum Disilicide Intermetallic Composites," *Metallurgical Transactions A*, **23A** (1992), pp. 2249-2257.
4. K. T. Venkateswara Rao, S. C. Siu and R. O. Ritchie, "Failure Mechanisms in SiC-Fiber Reinforced 6061 Aluminum Alloy Composites Under Monotonic and Cyclic Loading," *Metallurgical Transactions A*, **24A** (1993), pp. 721-734.
5. W. O. Soboyejo, K. T. Venkateswara Rao, S. M. L. Sastry and R. O. Ritchie, "An Investigation of the Fatigue and Fracture Behavior of Advanced High-Temperature Intermetallics Reinforced with Ductile Phases," *Metallurgical Transactions A*, **24A** (1993), pp. 585-600.
6. K. T. Venkateswara Rao, G. R. Odette and R. O. Ritchie, "Ductile-Reinforcement Toughening in γ -TiAl Intermetallic-Matrix Composites: Effects on Fracture Toughness and Fatigue-Crack Propagation Resistance," *Acta Metallurgica et Materialia*, **41** (1993), in review.
7. L. Muruges, K. T. Venkateswara Rao and R. O. Ritchie, "Processing of Ductile-Phase Nb/Nb₃Al *In Situ* Composites," *Metallurgical Transactions B*, **24B** (1993), in review.
8. L. Muruges, K. T. Venkateswara Rao and R. O. Ritchie, "Crack Growth in Nb-Ductile Phase Toughened Nb₃Al *In Situ* Composites Under Monotonic and Cyclic Loading," *Scripta Metallurgica et Materialia*, **27** (1993), in review.

8.2 Conference Proceedings

9. K. T. Venkateswara Rao, G. R. Odette and R. O. Ritchie, "Fatigue and Fracture Resistance of Ductile-Phase Toughened Intermetallic-Matrix Composites: Behavior in β -TiNb/ γ -TiAl," in *Fatigue of Advanced Materials*, R. O. Ritchie, R. H. Dauskardt and B. N. Cox (eds.), Materials and Components Engineering Publications Ltd., Edgbaston, U.K. (1991), pp. 429-437.
10. L. Muruges, K. T. Venkateswara Rao, L. C. De Jonghe and R. O. Ritchie, "Fabrication of Nb₃Al Intermetallic *in situ* Composite Microstructures," in *Developments in Ceramic and Metal-Matrix Composites*, Symposium Proceedings of The Minerals, Metals and Materials Society, G. Upadhy (ed.), The Minerals, Metals and Materials Society of AIME, Warrendale, PA (1992), pp. 222-237.
11. L. Muruges, K. T. Venkateswara Rao, L. C. De Jonghe and R. O. Ritchie, "Fracture and Fatigue Behavior in Nb₃Al + Nb Intermetallic Composites," in *Intermetallic Matrix Composites II*, MRS Symposium Proceedings, D. Miracle, J. Graves and D. Anton (eds.), Materials Research Society, Pittsburgh, PA, Vol. 273 (1992), pp. 433-438.
12. K. T. Venkateswara Rao and R. O. Ritchie, "Microstructural Effects on Fatigue-Crack Growth in γ -TiAl/ β -TiNb Intermetallic Composites," in *Intermetallic Matrix Composites II*, MRS Symposium Proceedings, D. Miracle, J. Graves and D. Anton (eds.), Materials Research Society, Pittsburgh, PA, Vol. 273 (1992), pp. 127-134.
13. K. T. Venkateswara Rao, G. R. Odette and R. O. Ritchie, "The Role of Interface and Reinforcement Properties on the Fracture and Fatigue Resistance of Ductile-Phase Toughened γ -TiAl Intermetallics," in *Structural Intermetallics*, Symposium Proceedings of the Minerals, Metals and Materials Society of AIME, Warrendale, PA (1993).

8.3 Ph.D. Theses

14. L. Muruges, "Monotonic and Cyclic Crack Growth in Ductile-Phase Toughened Nb₃Al Intermetallic Composites." Ph.D. thesis, Department of Materials Science and Mineral Engineering, University of California, Berkeley, May 1993.

9. DISTRIBUTION LIST

AFOSR/NC
ATTN: Drs. A. H. Rosenstein and C. Ward
Bldg. #410
Bolling Air Force Base
Washington, D.C. 20332-6448

AFWAL/MLLM
ATTN: Branch Chief
Wright-Patterson AFB
Dayton, OH 45433

AFWAL/MLLS
ATTN: Branch Chief
Wright-Patterson AFB
Dayton, OH 45433

AFWAL/MLLN
ATTN: Branch Chief
Wright-Patterson AFB
Dayton, OH 45433

Dr. Hugh R. Gray
NASA Lewis Research Center
Materials and Structures Division
21000 Brookpark Rd.
Cleveland, OH 44135

Prof. A. G. Evans
Materials Department
University of California
Santa Barbara, CA 93106

Dr. J. J. Petrovic
Los Alamos National Labs.
Group MST-4, Mail Stop G771
Los Alamos, NM 87545

Dr. A. F. Giamei
United Technologies Research Center
Silver Lane, MS-22
East Hartford, CT 06108

Dr. D. M. Dimiduk
AFWAL Materials Laboratory
WL/MLLN
Wright Patterson AFB
Dayton, OH 45433-6533

Dr. T. Nicholas
AFWAL Materials Laboratory
WL/MLLN
Wright Patterson AFB
Dayton, OH 45433-6533

Dr. Edward A. Loria
Niobium Products Co., Ltd.
300 Corporate Center Drive
Carapolis, PA 15108